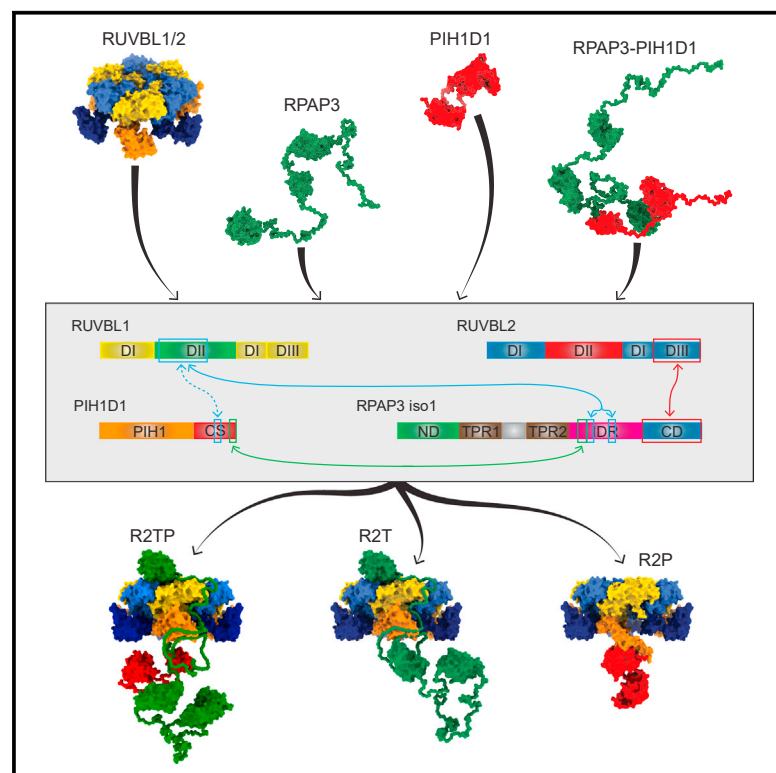


# Structure

## Assembly principles of the human R2TP chaperone complex reveal the presence of R2T and R2P complexes

### Graphical abstract



### Authors

Thiago V. Seraphim, Nardin Nano, Yiu Wing Sunny Cheung, ..., Carlos H.I. Ramos, Philipp Kukura, Walid A. Houry

### Correspondence

walid.houry@utoronto.ca

### In brief

R2TP is a conserved chaperone complex that is required for quaternary structure formation. Seraphim et al. perform detailed structural and biochemical analyses to understand the dynamics and mechanism of function of this complex. This work provides important insights into how a chaperone involved with complex assembly might work.

### Highlights

- R2TP, R2T, and R2P chaperone complexes are identified and characterized
- RPAP3 and RPAP3-PIH1D1 are highly dynamic proteins
- RPAP3 and PIH1D1 do not influence RUVBL1/2 ATPase activity
- RPAP3 N-domain binds proteins enriched in helical domains



## Article

# Assembly principles of the human R2TP chaperone complex reveal the presence of R2T and R2P complexes

Thiago V. Seraphim,<sup>1,2,12</sup> Nardin Nano,<sup>1,12</sup> Yiu Wing Sunny Cheung,<sup>1</sup> Siripat Aluksanasuwan,<sup>1,3,13</sup> Carolina Colleti,<sup>1,4</sup> Yu-Qian Mao,<sup>1</sup> Vaibhav Bhandari,<sup>1</sup> Gavin Young,<sup>5</sup> Larissa Höll,<sup>2</sup> Sadhna Phanse,<sup>1,2</sup> Yuliya Gordiyenko,<sup>5</sup> Daniel R. Southworth,<sup>6</sup> Carol V. Robinson,<sup>5</sup> Visith Thongboonkerd,<sup>3</sup> Lisandra M. Gava,<sup>4</sup> Júlio C. Borges,<sup>7</sup> Mohan Babu,<sup>2</sup> Leandro R.S. Barbosa,<sup>8,11</sup> Carlos H.I. Ramos,<sup>9</sup> Philipp Kukura,<sup>5</sup> and Walid A. Houry<sup>1,10,14,\*</sup>

<sup>1</sup>Department of Biochemistry, University of Toronto, 661 University Avenue, MaRS Centre, West Tower, Room 1612, Toronto, ON M5G 1M1, Canada

<sup>2</sup>Department of Chemistry and Biochemistry, University of Regina, Regina, SK S4S 0A2, Canada

<sup>3</sup>Medical Proteomics Unit, Office for Research and Development, Faculty of Medicine Siriraj Hospital, Mahidol University, Bangkok, Thailand

<sup>4</sup>Center of Biological and Health Sciences, Federal University of São Carlos, São Carlos, SP 13560-970, Brazil

<sup>5</sup>Physical and Theoretical Chemistry Laboratory, Department of Chemistry, University of Oxford, Oxford OX1 3QZ, UK

<sup>6</sup>Department of Biochemistry and Biophysics, Institute for Neurodegenerative Diseases, University of California, San Francisco, CA 94158, USA

<sup>7</sup>São Carlos Institute of Chemistry, University of São Paulo, São Carlos, SP 13566-590, Brazil

<sup>8</sup>Institute of Physics, University of São Paulo, São Paulo, SP 05508-090, Brazil

<sup>9</sup>Institute of Chemistry, University of Campinas (UNICAMP), Campinas, SP 13083-970, Brazil

<sup>10</sup>Department of Chemistry, University of Toronto, Toronto, ON M5S 3H6, Canada

<sup>11</sup>Brazilian Synchrotron Light Laboratory (LNLS), Brazilian Center for Research in Energy and Materials (CNPEM), Campinas, SP 13083-100, Brazil

<sup>12</sup>These authors contributed equally

<sup>13</sup>Present address: School of Medicine, Mae Fah Luang University, Chiang Rai, Thailand

<sup>14</sup>Lead contact

\*Correspondence: [walid.houry@utoronto.ca](mailto:walid.houry@utoronto.ca)

<https://doi.org/10.1016/j.str.2021.08.002>

## SUMMARY

R2TP is a highly conserved chaperone complex formed by two AAA+ ATPases, RUVBL1 and RUVBL2, that associate with PIH1D1 and RPAP3 proteins. R2TP acts in promoting macromolecular complex formation. Here, we establish the principles of R2TP assembly. Three distinct RUVBL1/2-based complexes are identified: R2TP, RUVBL1/2-RPAP3 (R2T), and RUVBL1/2-PIH1D1 (R2P). Interestingly, we find that PIH1D1 does not bind to RUVBL1/RUVBL2 in R2TP and does not function as a nucleotide exchange factor; instead, RPAP3 is found to be the central subunit coordinating R2TP architecture and linking PIH1D1 and RUVBL1/2. We also report that RPAP3 contains an intrinsically disordered N-terminal domain mediating interactions with substrates whose sequences are primarily enriched for Armadillo repeat domains and other helical-type domains. Our work provides a clear and consistent model of R2TP complex structure and gives important insights into how a chaperone machine concerned with assembly of folded proteins into multisubunit complexes might work.

## INTRODUCTION

The R2TP chaperone complex was initially discovered by our group in a systematic proteome-wide screen for Hsp90-interacting proteins in yeast (Zhao et al., 2005). The complex was then found to be conserved in all higher eukaryotes. In humans, R2TP consists of RUVBL1, RUVBL2, PIH1D1, and RPAP3 (Figure 1). R2TP was found to play critical roles in the assembly of macromolecular complexes regulating central cellular functions, such as cell response to nutrients, DNA damage response, ribosome biogenesis, and RNA transcription and processing (Houry et al., 2018).

The R2TP complex has been shown to stabilize client proteins belonging to the phosphatidylinositol 3-kinase-related kinase (PIKK) family, such as mTOR, ATM, ATR, DNA-PKcs, and SMG-1, via interaction with the TTT complex (TELO2-TTI1-TTI2) (Cloutier et al., 2017; Horejsi et al., 2010; Kamano et al., 2013; Pal et al., 2021). R2TP is also involved in the assembly of the TSC complex (TSC1-TSC2-TBC1D7), a regulator of mTORC1, U5 snRNPs and L7Ae RNPs (Cloutier et al., 2017; Malinova et al., 2017; Mir et al., 2015), and RNA polymerase II (Bouillon et al., 2010). More recently, R2TP and R2TP-like complexes have been associated with dynein assembly (Maurizy et al., 2018; Zur Lage et al., 2018). Biochemical and cell biological

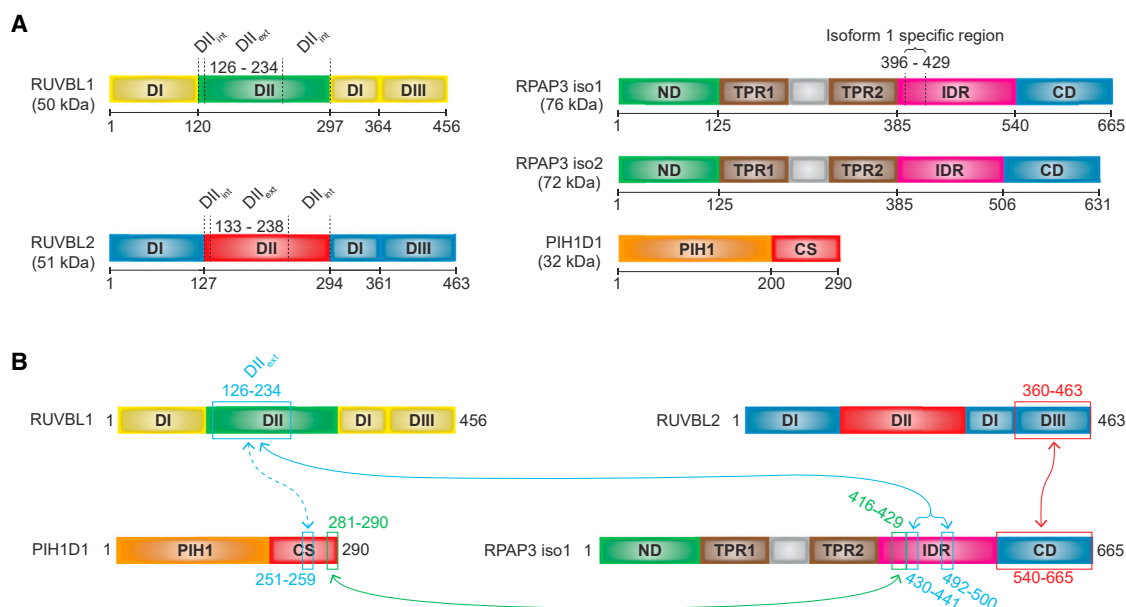


**Figure 1. Schematics of the R2TP subunits**

(A) Domain arrangement of RUVBL1, RUVBL2, RPAP3 isoforms 1 and 2, and PIH1D1. The indicated domain boundaries are used throughout this work. DI, domain I; DII, domain II; DII<sub>int</sub>, internal DII; DII<sub>ext</sub>, external DII; ND, N-terminal domain; TPR, tetratricopeptide repeat-containing domain; IDR, intrinsically disordered region; ND, N-terminal domain; CD, C-terminal domain; PIH1, protein interacting with Hsp90-1 domain; CS, CHORD-containing proteins and SGT1 domain.

(B) Mapping of R2TP interacting interfaces as determined in this work. Solid lines represent interactions observed in the R2TP and R2T complexes. Dashed line indicates the interaction observed in the R2P complex.

studies led to the hypothesis that R2TP functions as an assembly platform, bridging interactions between client proteins and chaperones, such as HSP70 and HSP90, in order to promote quaternary structure formation (Martino et al., 2018; Rivera-Calzada et al., 2017).

RUVBL1 and RUVBL2 (Figure 1A) belong to the AAA+ superfamily (ATPases Associated with diverse cellular Activities) of P-loop NTPases, bearing Walker A and Walker B motifs required for nucleotide binding and hydrolysis (Seraphim and Houry, 2020). These motifs are encompassed within the  $\alpha\beta\alpha$  domain I (DI), while the  $\alpha$ -helical domain III (DIII) contains a *trans*-acting Arg (R-finger) (Seraphim and Houry, 2020). DI is divided into two subdomains by the so-called insertion or domain II (DII) (Figure 1A). DII was recently proposed to be conformationally controlled via nucleotide binding (Matias et al., 2006; Silva et al., 2018). DII contains an internal part (DII<sub>int</sub>) located close to DI and DIII and an external OB-fold region (DII<sub>ext</sub>) protruding from the RUVBL protomer. Typically, RUVBL1 and RUVBL2 assemble into heterohexameric complexes that can also associate via DII<sub>ext</sub> to form double-heterohexameric species (Lakomek et al., 2015; Lopez-Perrote et al., 2012).

PIH1D1 has a PIH1 domain (Figure 1A) at the N terminus that binds to peptides containing phosphorylated DSDD/E motifs present in TEL02 and MRE11 (Horejsi et al., 2014; von Morgen et al., 2017). PIH1D1 also contains a C-terminal CS domain (CHORD-containing proteins and SGT1) that binds to RPAP3 (Henri et al., 2018). RPAP3 is the largest R2TP subunit, bearing an uncharacterized N-terminal domain (ND), two TPR domains (TPR1 and TPR2) that bind to the C-terminal EEVD motif of

HSP90, and an intrinsically disordered region (IDR) connecting the TPR2 to the C-terminal domain (CD) (Figure 1A) (Henri et al., 2018; Maurizy et al., 2018). Moreover, RPAP3 has been shown to have two isoforms in the cell (RPAP3 iso1 and iso2; Figure 1A), but only isoform 1 interacts with PIH1D1 (Yoshida et al., 2013).

Recently, cryo-electron microscopy (cryo-EM) studies revealed that, in human R2TP, RUVBL2 DIII binds RPAP3 CD while DII binds to PIH1D1 (Martino et al., 2018). Furthermore, PIH1D1 has been proposed to function as a nucleotide exchange factor (NEF) for R2TP, inducing conformational changes that result in the opening of the heterohexameric ring, hence modulating the accessibility of the ATP-binding pocket of RUVBL1/2 (Munoz-Hernandez et al., 2019).

Here, we report a detailed biophysical and biochemical analysis of the human R2TP subunits and their binding interfaces. By using size-exclusion chromatography coupled to static light scattering (SEC-MALS), small-angle X-ray scattering (SAXS), and mass photometry, we report low-resolution solution structures of the RUVBL1/2 heterohexamer, RPAP3, and RPAP3-PIH1D1, as well as their stoichiometry. Spectroscopic and mass spectrometry analyses revealed that RPAP3 ND is intrinsically disordered and mediates protein-protein interaction. Using pull-down experiments, we revealed that PIH1D1 does not bind directly to RUVBL1/2 in the R2TP complex. Our work shows that RPAP3 is the only link between RUVBL1/2 and PIH1D1 in R2TP and that RPAP3 contains two RUVBL-binding regions. RPAP3 and PIH1D1 were found to compete for RUVBL1/2 binding, hence forming R2T (RUVBL1-RUVBL2-RPAP3) and R2P

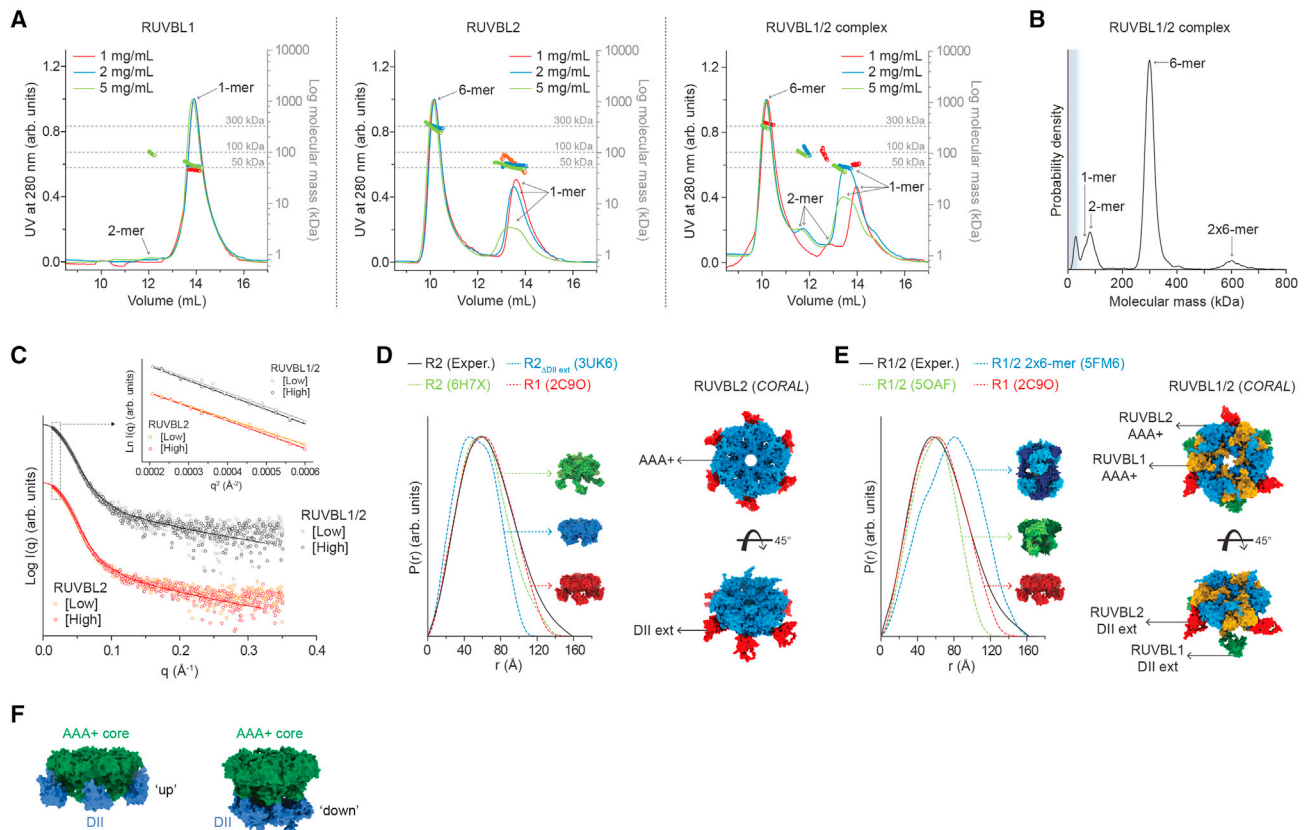


**Figure 2. Solution structure of RUVBL1 and RUVBL2**

(A) Molecular mass determination of RUVBL1, RUVBL2, and RUVBL1/2 complex using SEC-MALS. Molecular masses of 50 kDa, 100 kDa, and 300 kDa are indicated as references (dashed gray lines). See also Table S1 and Figures S2A–S2D.

(B) Molecular mass distribution of the RUVBL1/2 complex by mass photometry. The observed oligomeric species are indicated.

(C) SAXS profiles of RUVBL2 and RUVBL1/2 complexes (empty circles) at 0.85 mg/mL (low) and 1.7 mg/mL (high), and their respective GNOM fits (solid lines). Guinier approximation analyses are shown in the inset. Data are shown as empty circles and their respective linear fits are displayed as solid lines.

(D) Experimental  $P(r)$  function of RUVBL2 and comparison with theoretical  $P(r)$  of RUVBL1 hexamer (R1), RUVBL2 hexamer (R2), and RUVBL2 hexamer lacking DII<sub>ext</sub> (R2<sub>ΔDIIext</sub>). Structures are shown on the left side. On the right side, the CORAL model of RUVBL2 is displayed. The AAA+ core and DII<sub>int</sub> are colored in blue; DII<sub>ext</sub> is shown in red. See also Table S2; Figures S2E and S2F.

(E) Experimental  $P(r)$  of RUVBL1/2 complex shown in comparison with theoretical  $P(r)$  of RUVBL1/2 double hexamer (R1/2 2x6-mer), RUVBL1/2 hexamer in the INO80-bound conformation (R1/2), and RUVBL1 hexamer (R1). Displayed on the right is the RUVBL1/2 CORAL model. AAA+ cores and DII<sub>int</sub> of RUVBL1 (yellow) and RUVBL2 (blue) are shown; RUVBL1 DII<sub>ext</sub> and RUVBL2 DII<sub>ext</sub> are colored in green and red, respectively. See also Table S2; Figures S2E and S2F.

(F) Surface representation of RUVBL1 hexamers with DII<sub>ext</sub> in "up" (PDB: 2C9O) and "down" (PDB: 5OAF) conformations. The AAA+ core and DII<sub>int</sub> are displayed in green; DII<sub>ext</sub> is shown in blue.

(RUVBL1-RUVBL2-PIH1D1) complexes, both *in vitro* and in cells. We also demonstrate, based on ATPase and nucleotide-binding affinity assays, that PIH1D1 is not a NEF as reported by Munoz-Hernandez et al. (2019). Our solution-based characterization allows us to propose detailed models for the assembly of human R2TP, R2T, and R2P. These models highlight the critical role played by the DII domains of the RUVBLs in dictating the architecture of these complexes and clarify several issues raised by the recent cryo-EM R2TP structures.

## RESULTS

### Solution structure of human RUVBL1 and RUVBL2

We purified recombinant untagged human RUVBL1 and RUVBL2 in their folded state (Figure S1) and initially evaluated their solution behavior by SEC-MALS (Figure 2A and Ta-

ble S1). RUVBL1 alone behaved as a monomer at concentrations from 1 to 5 mg/mL (19.9–99.5  $\mu\text{M}$  protomer). However, at similar concentrations (19.5–97.7  $\mu\text{M}$  protomer), RUVBL2 formed monomers and hexamers. Analytical SEC (Figure S2A) and nanoflow electrospray ionization mass spectrometry experiments (Figure S2B) supported the results of SEC-MALS experiments showing that monomer is the main species for RUVBL1, whereas the hexamer is the major species for RUVBL2. When RUVBL1 and RUVBL2 were mixed at 1:1 molar ratio, hexamers, dimers, and monomers were observed by SEC-MALS at all tested concentrations (Figure 2A and Table S1). Interestingly, the appearance of dimeric species suggested the formation of RUVBL1-RUVBL2 heterodimers. As noticed for RUVBL2, increasing the concentration of the RUVBL1/2 complex promoted oligomerization (Figure 2A).

We also used the recently developed mass photometry technology (Young et al., 2018) to characterize the oligomeric behavior of RUVBL1/2 in solution (Figure 2B). Even at low concentrations of 0.2  $\mu$ M, RUVBL1/2 displayed primarily hexameric species and, to a lower extent, dimers, monomers, and double hexamers. Analytical SEC experiments showed that RUVBL1 readily associates with RUVBL2 to form high molecular mass species, even at low concentrations (Figure S2A). The addition of nucleotides did not affect the solution behavior of RUVBL1, RUVBL2, or RUVBL1/2 complex (Figure S2A). However, the presence of a tag at the N terminus of RUVBL1 or RUVBL2 affected the hydrodynamic behavior of the individual proteins (Figure S2C) and the heterocomplex (Figure S2D). Electron micrographs of RUVBL1/2 (Figure S2D) clearly showed a tendency to form double hexamers when one of the subunits was N-terminally tagged. This is similar to what we observed with the yeast proteins (Cheung et al., 2010). Therefore, all of our experiments were performed using untagged RUVBL1 and RUVBL2.

Next, the solution structure and conformation of RUVBL proteins were studied by SAXS. Shown in Figure 2C are the scattering profiles of RUVBL2 and RUVBL1/2 at two concentrations. Inspection of the curves by Guinier approximation (Figure 2C, inset) and dimensionless Kratky analysis (Figure S2E) suggested that samples were well behaved (Table S2), with RUVBL1/2 complex presenting slightly higher flexibility than RUVBL2, likely due to DII dynamics. Using merged scattering profiles, distance distribution functions  $P(r)$  were generated, revealing similar dimensions for RUVBL2 and RUVBL1/2 (Figures 2D and 2E; Table S2).

To obtain further insights into RUVBL conformations in solution, we calculated theoretical  $P(r)$  values from the published high-resolution three-dimensional (3D) structures and compared them with the experimental SAXS data (Figures 2D and 2E). It was intriguing to observe that the DII domain can adopt either an “up” or “down” conformation depending on whether DII is close or away from the AAA+ core, respectively (Figure 2F). Comparison between the experimental  $P(r)$  of RUVBL2, RUVBL1/2, and the theoretically derived  $P(r)$  from the different X-ray structures (Figures 2D and 2E) suggests that, in solution, hexameric RUVBL2 and hetero-hexameric RUVBL1/2 have DII in the up conformation. Furthermore, 3D Complexes with Random Loops (CORAL) models (Petoukhov et al., 2012) were constructed for both RUVBL2 (Figure 2D) and RUVBL1/2 (Figure 2E). All of the ring-like structures displayed DII adopting the up conformation. The modeling strategy showed an excellent fit with experimental data for both proteins (Figure S2F and Table S2).

Taken together, these experiments unambiguously demonstrate that RUVBL1 is mainly monomeric, whereas RUVBL2 and RUVBL1/2 are mostly hexamers in solution. Moreover, the DII domains in apo RUVBL2 and apo RUVBL1/2 hexamers adopt the up conformation.

### Solution structure and dynamics of RPAP3 and RPAP3-PIH1D1 complex

Next, we characterized the solution behavior of RPAP3 iso1 (Figure 1A; also referred to here as RPAP3), PIH1D1, and the RPAP3-PIH1D1 complex. We purified recombinant RPAP3 and RPAP3-PIH1D1 in their folded state (Figure S1) and carried out SEC-MALS experiments varying protein concentration from 1

to 3 mg/mL (13.2–39.6  $\mu$ M protomers of RPAP3 and 9.3 to 27.8  $\mu$ M protomers of RPAP3-PIH1D1). RPAP3 behaved as a monomer, while RPAP3-PIH1D1 formed heterodimers in solution (Figure 3A and Table S1). We also purified PIH1D1 (Figure S1), though due to solubility issues we were not able to reach high concentrations, precluding accurate molecular mass determinations. However, the chromatographic profile of PIH1D1 showed three peaks, suggesting a behavior composed of multiple oligomeric species in solution (Figure 3A).

The molecular masses of RPAP3, RPAP3-PIH1D1, and PIH1D1 were also investigated by mass photometry (Figure 3B). RPAP3 displayed molecular mass distribution with two peaks, a main one corresponding to monomers and a minor one corresponding to dimers. The monomer molecular mass is similar to that obtained by analytical ultracentrifugation sedimentation velocity experiments (Figure S3A). RPAP3-PIH1D1, on the other hand, displayed a molecular mass distribution consisting mainly of heterodimers (Figure 3B). For PIH1D1, although close to the limit of the detection of the instrument, mass photometry revealed at least three peaks corresponding to monomers, dimers, and tetramers (Figure 3B).

The structures of the individual domains of RPAP3 have been solved (Henri et al., 2018; Horejsi et al., 2014; Martino et al., 2018; Maurizy et al., 2018; Pal et al., 2014); however, the RPAP3 ND remains largely unknown. To gain information about this domain, we initially performed a predictive analysis using PSIPRED, DISOPRED, and MARCOIL servers (Figure S3B). A region comprising ~50 residues of RPAP3 ND was found to be  $\alpha$ -helix prone, correlating with a strong likelihood for coiled-coil formation. A high disorder index was observed for the rest of the domain (~65–75 residues). We then purified recombinant RPAP3 ND (Figure 1A) and submitted it to structural analyses. Far-UV circular dichroism revealed a spectral profile characteristic of disordered proteins with some  $\alpha$ -helical content, with minima at ~202 nm and ~222 nm (Figure S3C). Addition of 4 M GdnHCl to RPAP3 ND caused loss of signal in the ~222 nm band, leading to the appearance of a ~218 nm peak (Figure S3C), suggesting that PII-type helical structures may be formed under this condition (Chemes et al., 2012). When exposing RPAP3 ND to increasing temperatures, we observed a loss of signal in its circular dichroism spectrum (Figure S3D). Nonetheless, we noticed loss of protein due to aggregation, and further inspection of its spectra revealed no substantial changes in the RPAP3 ND profile (Figure S3D, inset). Intrinsic fluorescence emission using Trp residues as probes revealed that W31 and W93 are fully exposed to the solvent, confirming the intrinsically disordered nature of RPAP3 ND (Figure S3E). Moreover, the hydropathy index of this domain was compatible with those of intrinsically disordered proteins (Figure S3F).

RPAP3 is a large protein containing extensive intrinsically disordered regions, e.g., ND and IDR, in addition to well-folded domains (Figures 1A, S1, S3B, and S3C), which makes it difficult to determine the structure of the full-length protein by X-ray crystallography or nuclear magnetic resonance. Therefore, we made use of SAXS to determine the structure and dynamics of the full-length RPAP3 and RPAP3-PIH1D1. The X-ray scattering curves of RPAP3 and RPAP3-PIH1D1 are depicted in Figure 3C. Guinier approximation showed that samples were monodisperse (Figure 3C, inset), and dimensionless Kratky analysis revealed that

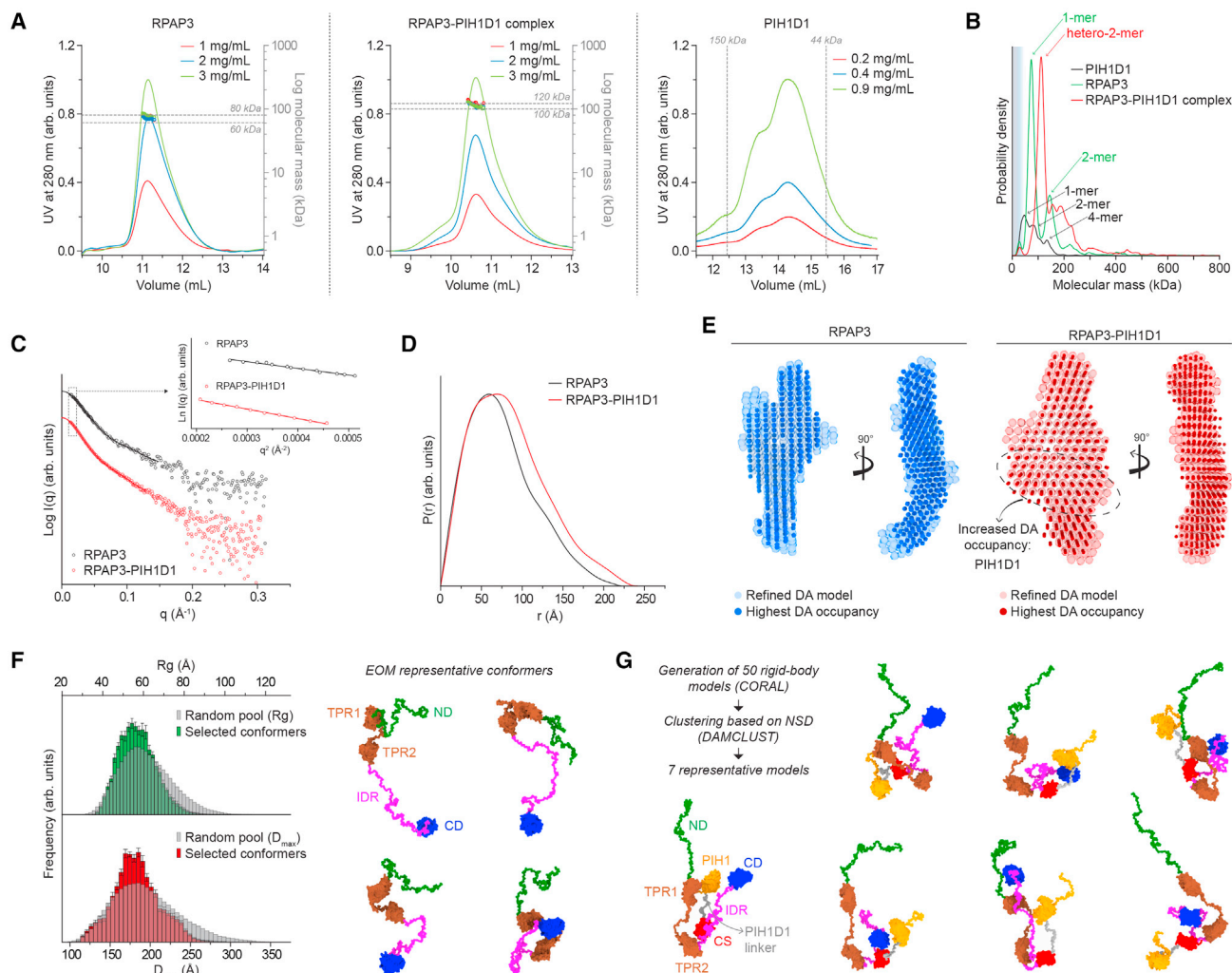


**Figure 3. Solution structure of RPAP3 and RPAP3-PIH1D1 complex**

(A) Molecular mass determination of RPAP3 and RPAP3-PIH1D1 complex by SEC-MALS. As reference, molecular masses are indicated by gray dashed lines. PIH1D1 chromatographic profiles are also shown. Peaks of molecular mass standards are indicated by gray dashed horizontal lines. See also Figure S3 and Table S1.

(B) Molecular mass distribution of PIH1D1, RPAP3, and RPAP3-PIH1D1 complex identified by mass photometry. Oligomeric species are indicated by arrows. (C) SAXS profiles of RPAP3 and RPAP3-PIH1D1 complex (empty circles) and respective GNOM fits (solid lines). Guinier regions are displayed in the inset (data and linear fit are shown as empty circles and solid lines, respectively).

(D) P(r) functions of RPAP3 and RPAP3-PIH1D1 complex.

(E) DA models of RPAP3 and RPAP3-PIH1D1 complex. Refined DA models are shown as translucent beads while the highest occupancies of DA among 20 models are shown as solid beads. In the RPAP3-PIH1D1 DA model, the region with increased DA occupancy is indicated by a dashed ellipse. See also Table S2.

(F) Ensemble optimization analysis of RPAP3. On the left, average Rg and D<sub>max</sub> distributions of the selected RPAP3 ensembles are shown in comparison with those of a random pool of RPAP3 conformers. Error bars correspond to SD. Representative RPAP3 conformers are shown on the right. See also Table S2.

(G) CORAL representative models of RPAP3-PIH1D1 complex.

RPAP3 is quite flexible in solution, while RPAP3-PIH1D1 tends to be slightly less flexible (Figure S3G).

P(r) functions were generated for RPAP3 and RPAP3-PIH1D1 (Figure 3D), displaying single peaks smoothly decaying to long distances, as those for elongated and flexible molecules (Kikhney and Svergun, 2015); RPAP3 displayed smaller size and dimensions than RPAP3-PIH1D1 complex (Table S2). Using dummy atoms (DA), *ab initio* models were generated (Figure S3H and Table S2, DAM). RPAP3 and RPAP3-PIH1D1 DA models have similar elongated shapes in solution (Figure 3E), albeit the

latter presented extra DA occupancy that can be attributed to the presence of PIH1D1 (Figure 3E, outlined by a black dashed ellipse). Since samples are conformationally polydisperse, we were not able to precisely determine the localization of RPAP3 domains or of PIH1D1 in the DA models. To overcome this issue, we employed the ensemble optimization method (EOM) to characterize the dynamics of RPAP3 in solution. Using the crystal structures of TPR1 (Pal et al., 2014), TPR2 (Henri et al., 2018), and CD (Maurizy et al., 2018) of RPAP3, the ensemble containing conformers best representing the experimental SAXS curve

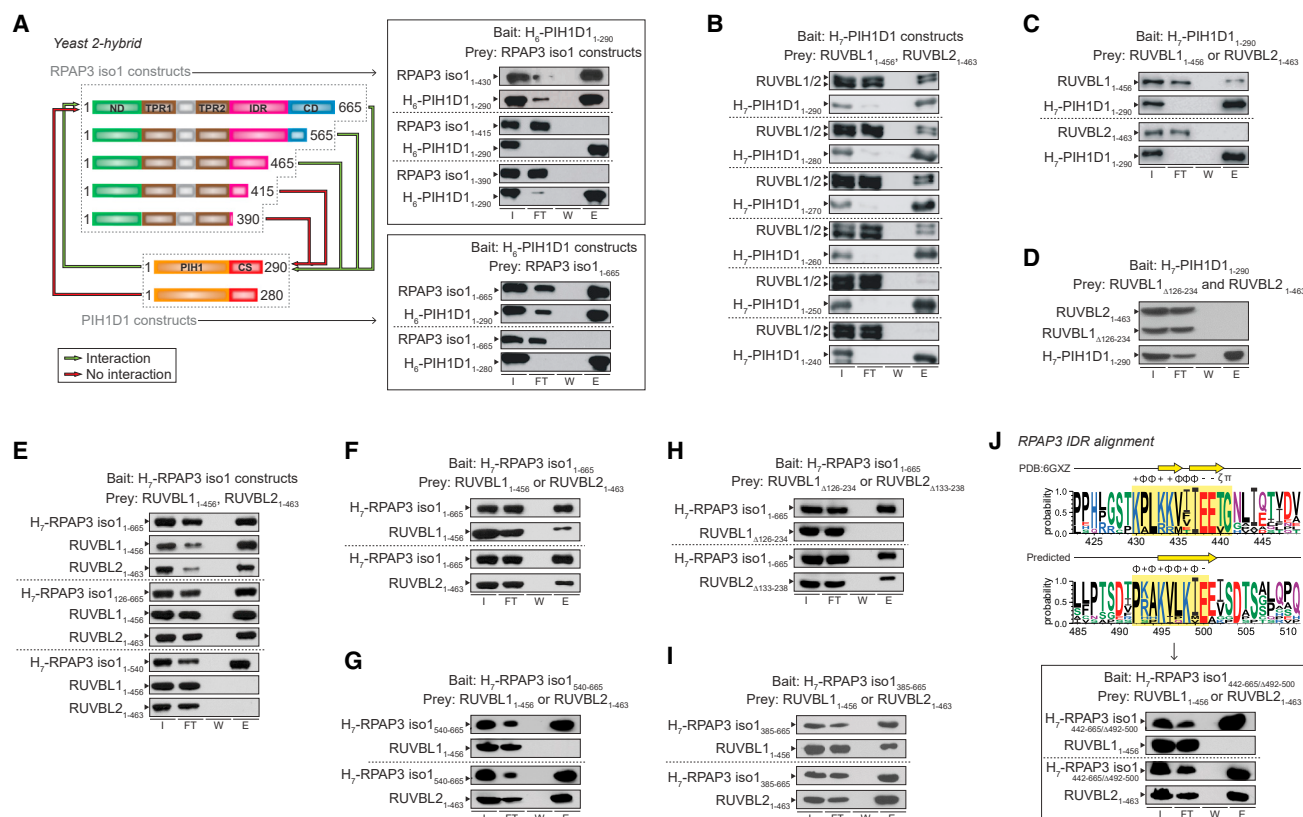


**Figure 4. Mapping the interacting interfaces between RPAP3 and PIH1D1, PIH1D1 and RUVBL1/2, and RPAP3 and RUVBL1/2**

(A) Schematics of RPAP3 iso1 and PIH1D1 constructs used for the yeast two-hybrid are displayed on the left. Interacting and non-interacting proteins are connected by green and red arrows, respectively. The panels on the right show the confirmation of yeast two-hybrid results by pull-down assays. In the top panel, H<sub>6</sub>-PIH1D1<sub>1-290</sub> was used to pull down RPAP3 iso1 constructs. In the lower panel, H<sub>6</sub>-PIH1D1 constructs were used to pull down RPAP3 iso1<sub>1-665</sub>. I, input; FT, flow-through; W, wash; E, elution. See also [Figures S4A and S4C](#).

(B–I) Determination of the interacting regions among the R2TP proteins. Bait and prey are indicated at the top of the gels. Proteins were detected using the respective antibodies. See text for a detailed explanation. See also [Figure S4B](#).

(J) The sequence logo of two conserved regions identified in the RPAP3 IDR (highlighted in yellow) is shown on top. Hydrophobic, acidic, basic, neutral, and polar amino acids are shown as black, red, blue, purple, and green letters, respectively. Secondary structures of the sequences are given, as well as the properties (+, positively charged; −, negatively charged; Φ, hydrophobic; ζ, hydrophilic; π, small side chain) of the most conserved residues. Shown on the bottom are the pull-downs of RUVBL1 or RUVBL2 with H<sub>7</sub>-RPAP3 iso1<sub>442-665/Δ492-500</sub>, i.e., RPAP3 lacking both of the conserved IDR regions. See also [Figure S5](#).

were selected from a pool of random conformers ([Figure 3F](#) and [S3I](#); [Table S2](#), EOM). The analysis indicates that despite being a very dynamic protein, RPAP3 adopts more compact conformations rather than fully stretched ones.

Although the EOM strategy was not applicable to RPAP3-PIH1D1 complex due to intrinsic limitations of the methodology, we explored RPAP3-PIH1D1 SAXS data further using a combination of rigid-body modeling by CORAL followed by models clustering based on similarity using DAMCLUST. RPAP3 domains used for EOM were applied in CORAL, in addition to PIH1D1 PIH1 ([Horejsi et al., 2014](#)) and CS ([Henri et al., 2018](#)) domains. Contacts between PIH1D1 and RPAP3 were imposed according to interacting interfaces identified in this work and presented below. After generation of 50 rigid-body structures, we clustered them to seven final representative structures ([Figure 3G](#) and [S3I](#); [Table S2](#), CORAL) whereby, much like RPAP3, more compact structures instead of stretched ones were observed.

In summary, RPAP3 is a monomeric, elongated, and dynamic protein containing an intrinsically disordered ND and adopts more compact conformations. PIH1D1 binds to RPAP3 at a 1:1 molar ratio, forming a compact complex, and seems to partially restrict RPAP3 IDR flexibility.

### Mapping the RPAP3- and PIH1D1-interacting interfaces

In our effort to determine the quaternary assembly of R2TP, we subsequently sought to identify the binding interfaces among the R2TP subunits. The interaction between RPAP3 and PIH1D1 was initially investigated by yeast two-hybrid assays ([Figures 4A and S4A](#)). Full-length RPAP3 (RPAP3 iso1<sub>1-665</sub>) interacted with full-length PIH1D1 (PIH1D1<sub>1-290</sub>), but not with the PIH1D1 construct lacking the last ten amino acid residues of its CS domain (PIH1D1<sub>1-280</sub>). Pull-down assays further confirmed that the deletion of PIH1D1 residues from 281 to 290 disrupted PIH1D1 binding to RPAP3 ([Figure 4A](#)).

A comparison between RPAP3 isoforms revealed that amino acid residues from 396 to 429 in iso1 are missing in iso2, which does not interact with PIH1D1 (Yoshida et al., 2013) (Figure 1A). In addition, our yeast two-hybrid assays showed that RPAP3 iso1<sub>1–565</sub> and RPAP3 iso1<sub>1–465</sub> interacted with PIH1D1<sub>1–290</sub>, but RPAP3 iso1<sub>1–415</sub> and RPAP3 iso1<sub>1–390</sub> failed to do so (Figures 4A and S4A). Considering these results and differences between RPAP3 iso1 and iso2 led us to hypothesize that the RPAP3 iso1 region spanning residues from 416 to 429 contains the PIH1D1-binding site. Therefore, pull-down experiments were carried out with RPAP3 iso1<sub>1–430</sub> and RPAP3 iso1<sub>1–415</sub>, as well as RPAP3 iso1<sub>1–390</sub> as a negative control, since it lacks almost the entire IDR (Figure 1A). We observed that RPAP3 iso1<sub>1–430</sub> was pulled down by PIH1D1<sub>1–290</sub>, whereas RPAP3 iso1<sub>1–415</sub> and RPAP3 iso1<sub>1–390</sub> were not, confirming that the PIH1D1-binding region on RPAP3 iso1 is contained within residues 416 and 429 of its IDR. In addition, crosslinking followed by mass spectrometry (XL-MS) experiments with the R2TP complex identified crosslinked peptides between RPAP3 IDR and PIH1D1 CS (Figure S4B and Table S3).

Altogether, RPAP3 iso1 IDR residues from 416 to 429 are required for binding to PIH1D1, and the deletion of the last ten residues in the  $\beta$ 7 strand of PIH1D1 CS disrupts its association with RPAP3 iso1 (Figure 1B).

### Mapping the PIH1D1- and RUVBL1/2-interacting interfaces

Next, the association between RUVBL1/2 and H<sub>7</sub>-PIH1D1 was investigated using pull-down assays. Full-length PIH1D1<sub>1–290</sub> interacted with full-length RUVBL1<sub>1–456</sub>/2<sub>1–463</sub> to form the R2P complex (Figure 4B, first panel from top). To identify where RUVBL1/2 binds on PIH1D1, we made a series of progressive deletions of ten residues at the PIH1D1 C terminus. PIH1D1<sub>1–280</sub>, PIH1D1<sub>1–270</sub>, and PIH1D1<sub>1–260</sub> constructs all interacted with RUVBL1<sub>1–456</sub>/2<sub>1–463</sub> in a similar manner (Figure 4B, second to fourth panels from top). However, PIH1D1<sub>1–250</sub> and PIH1D1<sub>1–240</sub> interacted significantly less with RUVBL1<sub>1–456</sub>/2<sub>1–463</sub> (Figure 4B, fifth and sixth panels from top), suggesting that the binding site consists mainly of PIH1D1 residues from 251 to 259 in the CS domain (Figure 1B). Controls to rule out unspecific RUVBL1/2 binding to beads are shown in Figure S4C.

To determine which RUVBL protein binds to PIH1D1, we used H<sub>7</sub>-PIH1D1<sub>1–290</sub> to pull down either RUVBL1<sub>1–456</sub> or RUVBL2<sub>1–463</sub>; H<sub>7</sub>-PIH1D1<sub>1–290</sub> only interacted with RUVBL1<sub>1–456</sub> (Figure 4C). To determine where PIH1D1 bound on RUVBL1, we made a complex consisting of an RUVBL1 mutant lacking DII<sub>ext</sub> (RUVBL1 $\Delta$ <sub>126–234</sub>) and RUVBL2<sub>1–463</sub> and pulled it down with H<sub>7</sub>-PIH1D1<sub>1–290</sub> (Figure 4D), but no interaction was observed. Controls for unspecific RUVBL1, RUVBL2, and RUVBL1 $\Delta$ <sub>126–234</sub>/RUVBL2<sub>1–463</sub> binding to beads are shown in Figure S4C. Curiously, we did not observe crosslinked peptides between RUVBL proteins and PIH1D1 protein in XL-MS experiments with R2TP (Figure S4B).

Hence, residues from 251 to 259 in the  $\beta$ 5 strand of PIH1D1 CS domain bind to DII<sub>ext</sub> of RUVBL1 within the RUVBL1/2 complex (Figure 1B).

### Mapping the RPAP3- and RUVBL1/2-interacting interfaces

To determine the RPAP3 domain interacting with RUVBL proteins, we used full-length RPAP3 iso1, a RPAP3 mutant lacking ND

(RPAP3 iso1<sub>125–665</sub>), and a RPAP3 mutant lacking CD (RPAP3 iso1<sub>1–540</sub>) to pull down RUVBL1<sub>1–456</sub>/2<sub>1–463</sub>. The deletion of RPAP3 CD disrupted complex formation with RUVBL1/2 (Figure 4E). Next, to determine with which RUVBL protein RPAP3 associates, we used both RPAP3 iso1<sub>1–665</sub> and RPAP3 iso2<sub>1–631</sub> to pull down the individual RUVBL proteins. Both isoforms pulled down RUVBL1<sub>1–456</sub> and RUVBL2<sub>1–463</sub> (Figures 4F and S5A). To verify this further, we used the RPAP3 iso1 CD (RPAP3 iso1<sub>540–665</sub>) to pull down individual RUVBL proteins. Unexpectedly, RPAP3 iso1<sub>540–665</sub> only interacted with RUVBL2 (Figure 4G), suggesting the presence of a second binding site through which RUVBL1 would interact with RPAP3. There was no unspecific binding observed of RUVBL1<sub>1–456</sub>/RUVBL2<sub>1–463</sub>, RUVBL1<sub>1–456</sub>, and RUVBL2<sub>1–463</sub> to beads (Figure S4C). Note that XL-MS experiments did not show crosslinked peptides between RPAP3 CD and RUVBL proteins (Figure S4B), likely due to the lack of appropriate primary amines within the allotted distance or orientation to allow for crosslinking.

In the recently published cryo-EM structures of the human R2TP, RPAP3 CD was seen to interact with the RUVBL2 DIII domain, whereas RPAP3 ND and TPR domains, together with PIH1D1, were observed near the DII domains of the RUVBL proteins (Martino et al., 2018; Munoz-Hernandez et al., 2019). Indeed, our R2TP XL-MS experiments found RPAP3 ND, TPR1/2, and IDR peptides crosslinked with both RUVBL1 and RUVBL2 DII<sub>ext</sub> (Figure S4B and Table S3). Therefore, we wondered whether RPAP3 would bind the DII of RUVBLs. So, RPAP3 was used to pull down RUVBL proteins lacking the DII<sub>ext</sub> (RUVBL1 $\Delta$ <sub>126–234</sub> and RUVBL2 $\Delta$ <sub>133–238</sub>). RPAP3 iso1<sub>1–665</sub> interacted with RUVBL2 $\Delta$ <sub>133–238</sub> but not RUVBL1 $\Delta$ <sub>126–234</sub> (Figure 4H). These results suggest that, while the RPAP3 CD binds to RUVBL2, an additional RPAP3 region interacts with RUVBL1 DII<sub>ext</sub>.

To narrow down the binding regions between RUVBL1 and RPAP3, we removed ND and TPR domains of RPAP3 iso1 (RPAP3 iso1<sub>385–665</sub>) and iso2 (RPAP3 iso2<sub>385–631</sub>) and pulled down full-length RUVBL1 and RUVBL2. In the presence of the RPAP3 iso1 and iso2 IDR, interactions with both RUVBL1 and RUVBL2 were detected (Figures 4I and S5B), revealing that the second binding site was located within RPAP3 IDR. Global sequence alignment with RPAP3 was carried out to determine conserved amino acids in the IDR, whereby two regions were identified (Figure 4J). The first one encompasses amino acid residues from 430 to 441 and coincides with the RPAP3 iso1 region co-crystallized with PIH1D1 (Henri et al., 2018), forming two  $\beta$  strands. The second one is formed by amino acid residues from 492 to 500 and is predicted to also form a  $\beta$  strand. Not only the structures of these two regions but also their amino acid compositions are similar, with both regions containing five hydrophobic, three positively charged, and one or two negatively charged residues at the end (Figure 4J). We then deleted these regions to verify whether they corresponded to putative RUVBL1-binding interfaces. Two RPAP3 constructs, one corresponding to the deletion of the 430–441 region (RPAP3 iso1 $\Delta$ <sub>442–665</sub>) and one to the 492–500 region (RPAP3 iso1<sub>385–665</sub> $\Delta$ <sub>492–500</sub>), were tested and both interacted with RUVBL1<sub>1–456</sub> and RUVBL2<sub>1–463</sub> (Figure S5C). Interestingly, when the deletions of the two regions were combined in the RPAP3 iso1 $\Delta$ <sub>442–665</sub> $\Delta$ <sub>492–500</sub> construct, RPAP3 iso1 IDR was no longer observed to bind to RUVBL1<sub>1–456</sub>, while the

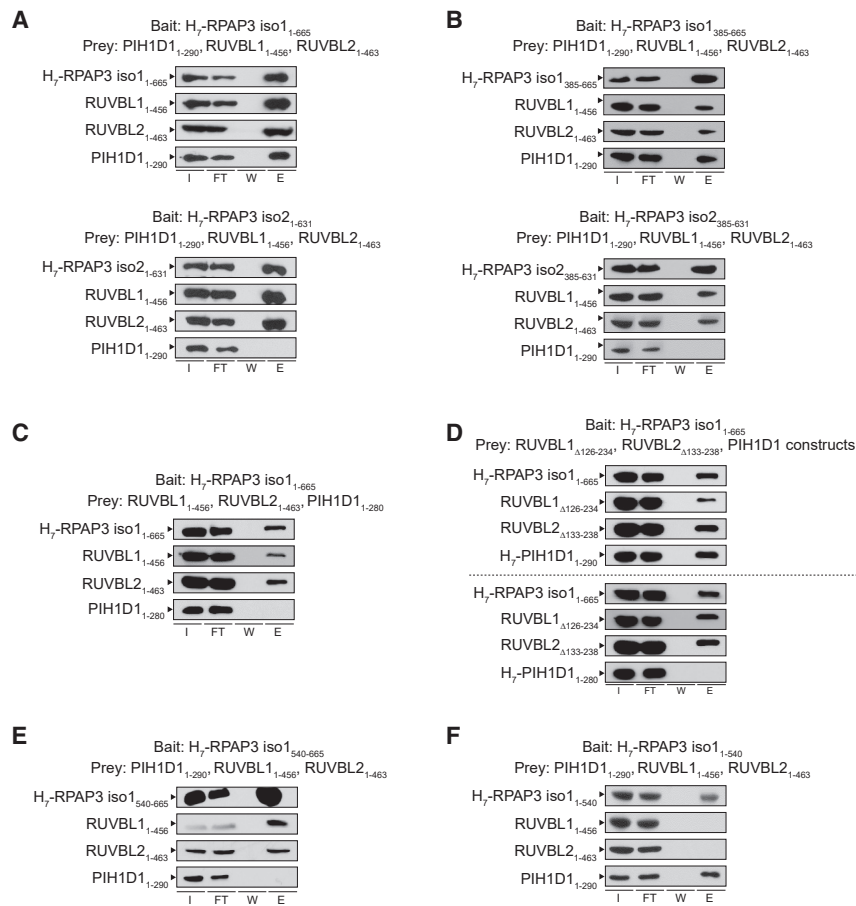


**Figure 5. Mapping the interaction interfaces that drive human R2TP complex assembly**

(A–F) Pull-down assays with bait and prey as indicated at the top of the gels. Proteins were detected using the respective antibodies. See text for more details. See also Figures S4B and S6.

whether the presence of the RPAP3 ND, TPR1, and TPR2 in the vicinity of the RUVBLs DII could be hindering the direct binding of PIH1D1 to RUVBL1/2. To investigate this possibility, RPAP3 iso1<sub>385–665</sub> and RPAP3 iso2<sub>385–631</sub>, which only have the IDR and CD, were co-expressed with PIH1D1<sub>1–290</sub> and mixed with co-expressed RUVBL1<sub>1–456</sub>/2<sub>1–463</sub>. Even in the absence of ND and TPR domains, RPAP3 iso1<sub>385–665</sub> formed a complex with PIH1D1<sub>1–290</sub> and RUVBL1<sub>1–456</sub>/2<sub>1–463</sub> (Figures 5B and S6B, top panels); however, RPAP3 iso2<sub>385–631</sub> did not (Figures 5B and S6B, bottom panels). These results suggest that RPAP3 iso2 and PIH1D1 may compete for RUVBL1/2 binding.

The above results lead us to propose that PIH1D1, in fact, does not directly interact with RUVBL1/2 within the R2TP complex. PIH1D1 interaction with RUVBL1/2 seems to be mediated by RPAP3 iso1. In agreement with this hypothesis, XL-MS data did not detect crosslinked peptides between PIH1D1 and RUVBL1/2 in R2TP (Figure S4B

binding to RUVBL2<sub>1–463</sub> was preserved due to the presence of the CD (Figure 4J). In agreement with these results, XL-MS data revealed that the RPAP3 K495 residue crosslinks with RUVBL1 and RUVBL2 DII<sub>ext</sub> peptides within the R2TP complex (Figure S4B and Table S3).

Our results demonstrate that RPAP3 iso1 and iso2 form complexes with RUVBL1/2 via two binding sites. The first is through RPAP3 CD, which binds to RUVBL2; the second is through two regions in IDR, 430–441 and 492–500, that bind to RUVBL1 DII<sub>ext</sub> and are proposed to form  $\beta$  strands (Figure 1B).

### The assembly of human R2TP

After mapping the interactions among the R2TP proteins, the assembly mechanism of the entire R2TP complex was investigated. Initially, bacterial cell lysates co-expressing RPAP3 iso1<sub>1–665</sub>-PIH1D1<sub>1–290</sub> or RUVBL1<sub>1–456</sub>/2<sub>1–463</sub> were mixed and purified, which allowed us to pull down the R2TP complex (Figures 5A and S6A, top panels). When the same approach was used but employing RPAP3 iso2<sub>1–631</sub>, PIH1D1<sub>1–290</sub> was no longer part of the complex (Figure 5A, bottom panel). On the other hand, when PIH1D1<sub>1–290</sub> was used to pull down the complex, RPAP3 iso2<sub>1–631</sub> was absent from it (Figure S6A, bottom panel).

We showed that PIH1D1 interacts with RUVBL1/2 (Figure 4B) and, taking into account the human R2TP structures (Martino et al., 2018; Munoz-Hernandez et al., 2019), we wondered

and Table S3). To confirm this, we carried out pull-down experiments using RPAP3 iso1 as bait and RUVBL1, RUVBL2, and the RPAP3-binding defective mutant of PIH1D1, PIH1D1<sub>1–280</sub>, as prey. RPAP3 iso1<sub>1–665</sub> pulled down RUVBL1<sub>1–456</sub>/2<sub>1–463</sub> but not PIH1D1<sub>1–280</sub> (Figure 5C), thereby confirming that PIH1D1 cannot directly bind to RUVBL1/2 when RPAP3 is bound to the ATPases. Deletion of the DII<sub>ext</sub> domains of RUVBLs, RUVBL1 $\Delta$ 126–234 and RUVBL2 $\Delta$ 133–238, did not interfere with the formation of the R2TP complex (Figure 5D, top panel). However, the replacement of PIH1D1<sub>1–290</sub> by PIH1D1<sub>1–280</sub>, which cannot bind RPAP3 (Figure 4A), showed impairment of the R2TP formation (Figure 5D, bottom panel). Therefore, instead of establishing a direct contact with RUVBL1/2, PIH1D1 depends on RPAP3 iso1 to be part of the R2TP complex.

The above experiments clearly establish that PIH1D1 cannot be part of the R2TP if not bound to RPAP3. Subsequently, we wondered which elements in RPAP3 might be responsible for disrupting the association between PIH1D1 and RUVBL1/2. We performed pull-down experiments using RPAP3 iso1<sub>540–665</sub> (CD), PIH1D1<sub>1–290</sub>, and RUVBL1<sub>1–456</sub>/2<sub>1–463</sub>. When RPAP3 iso1<sub>540–665</sub> was used as bait, it only pulled down RUVBL1/2 but not PIH1D1 (Figure 5E). Reverse pull-down, using PIH1D1<sub>1–290</sub> as bait, pulled down RUVBL1/2 but not RPAP3 iso1 CD (Figure S6C), hence revealing that the mere binding of the RPAP3 CD to RUVBL1/2 blocks PIH1D1 binding and vice versa.

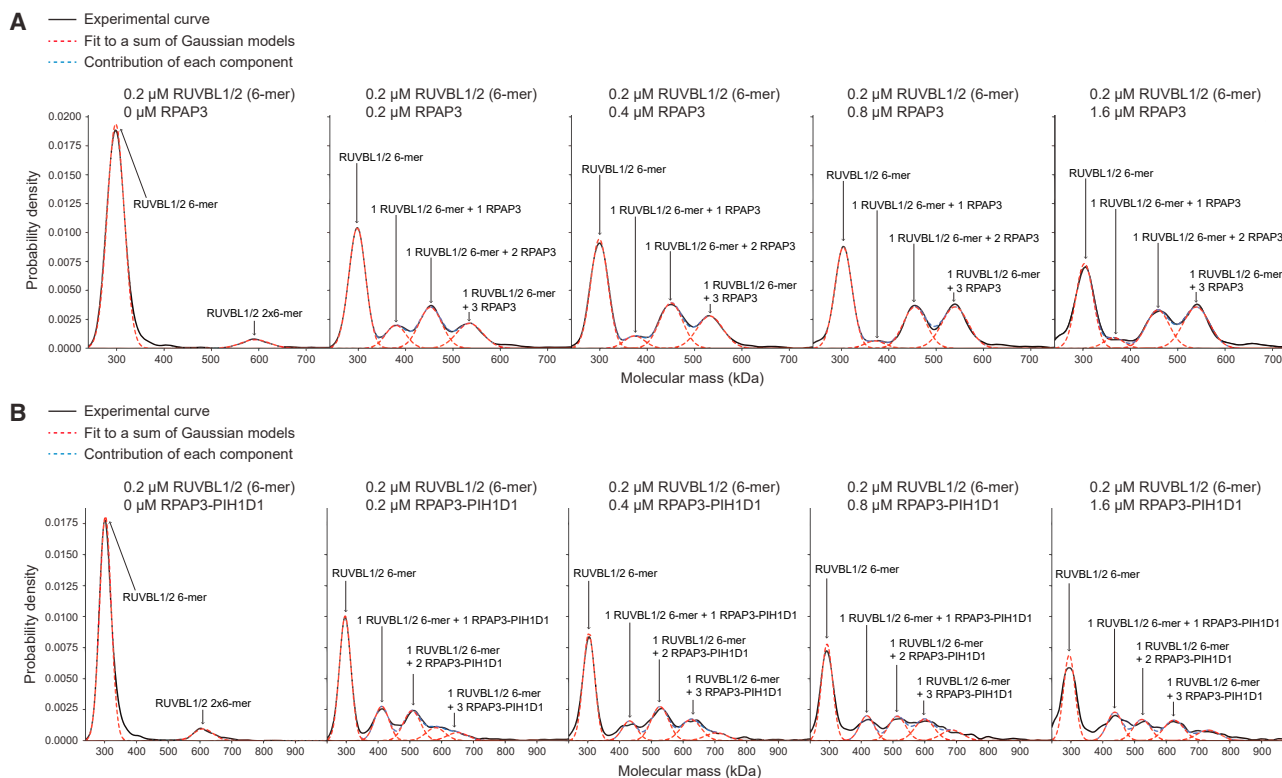


**Figure 6. Stoichiometry of the R2TP complex determined by mass photometry**

(A) Titration of RPAP3 iso1 into 0.2 μM RUVBL1/2 hexamers. Molecular mass distributions are shown for each RPAP3 iso1 concentration (solid black lines). The curves were fit to a sum of Gaussian models. The blue dashed lines show the fit for each experimental curve and the red dashed lines show the contribution of each component. Identified macromolecular species and their respective stoichiometries are indicated by arrows.

(B) Same as (A), but for titration of the RPAP3 iso1-PIH1D1 complex into 0.2 μM RUVBL1/2 hexamers.

We also tested whether the presence of all other RPAP3 iso1 regions, except CD, could affect PIH1D1 binding to RUVBL1/2. Figure 5F depicts the result of the experiment with the RPAP3 construct lacking the CD, RPAP3 iso1<sub>1-540</sub>, being used as a bait to pull down RUVBL1<sub>1-456</sub>/2<sub>1-463</sub> and PIH1D1<sub>1-290</sub>. The reverse pull-down, using PIH1D1<sub>1-290</sub> as bait instead, is shown in Figure S6D. Surprisingly, RPAP3 iso1<sub>1-540</sub> and PIH1D1<sub>1-290</sub> were able to interact with each other, but not with RUVBL1<sub>1-456</sub>/2<sub>1-463</sub>, suggesting that the simple binding of RPAP3 iso1 to PIH1D1 competes with its interaction to RUVBL1/2.

Altogether, these experiments demonstrate that RPAP3 is the central subunit of the R2TP complex, bridging the interaction between RUVBL1/2 and PIH1D1. Additionally, the binding of RPAP3 to RUVBL1/2 blocks the binding of PIH1D1 via two mechanisms: (1) binding of RPAP3 CD to RUVBL1/2 likely by changing the conformation of the DII domain in RUVBL1; and (2) binding of RPAP3 to PIH1D1 likely by blocking the binding site of PIH1D1 for RUVBL1 in the RUVBL1/2 complex.

### Stoichiometry of the subunits in the R2TP complex

Despite the recent studies on the human R2TP structure (Martino et al., 2018; Maurizy et al., 2018; Munoz-Hernandez et al., 2019), the number of RPAP3 and PIH1D1 subunits associated with RUVBL1/2 remains a matter of debate. To determine the subunit stoichiometry within R2TP, we made use of mass photometry.

Increasing concentrations of RPAP3 (0.2–1.6 μM) were titrated into a fixed amount of RUVBL1/2 (0.2 μM hexamers) as shown in Figure 6A. RUVBL1/2 complex alone was mostly hexamers with a small population of double hexamers. However, upon addition of RPAP3, the double-hexameric species disappeared and RUVBL1/2 hexamers containing one, two, and three bound RPAP3 appeared. Further addition of RPAP3, up to a ratio of eight RPAP3 monomers per RUVBL1/2 hexamer, revealed a gradual increase of species containing two and three bound RPAP3, with almost complete disappearance of the RUVBL1/2 species containing a single associated RPAP3.

Next, 0.2–1.6 μM RPAP3-PIH1D1 complex was titrated into 0.2 μM RUVBL1/2 hexamers (Figure 6B). When RPAP3-PIH1D1 was added at equimolar ratio to RUVBL1/2, the hexamers associated mostly with one or two RPAP3-PIH1D1 heterodimers. Increasing RPAP3-PIH1D1 concentrations allowed for the formation of RUVBL1/2 bound to three RPAP3-PIH1D1 molecules; however, in contrast to RPAP3 titration (Figure 6A), RUVBL1/2 hexamers bound to one, two, and three RPAP3-PIH1D1 molecules were equally populated.

The above results clearly indicate that R2TP and R2T are heterogeneous complexes containing different stoichiometries of RPAP3 or RPAP3-PIH1D1 bound to the RUVBL1/2. No usable results were obtained in a similar analysis with PIH1D1 due to the experimental limit of detection and instability of PIH1D1.

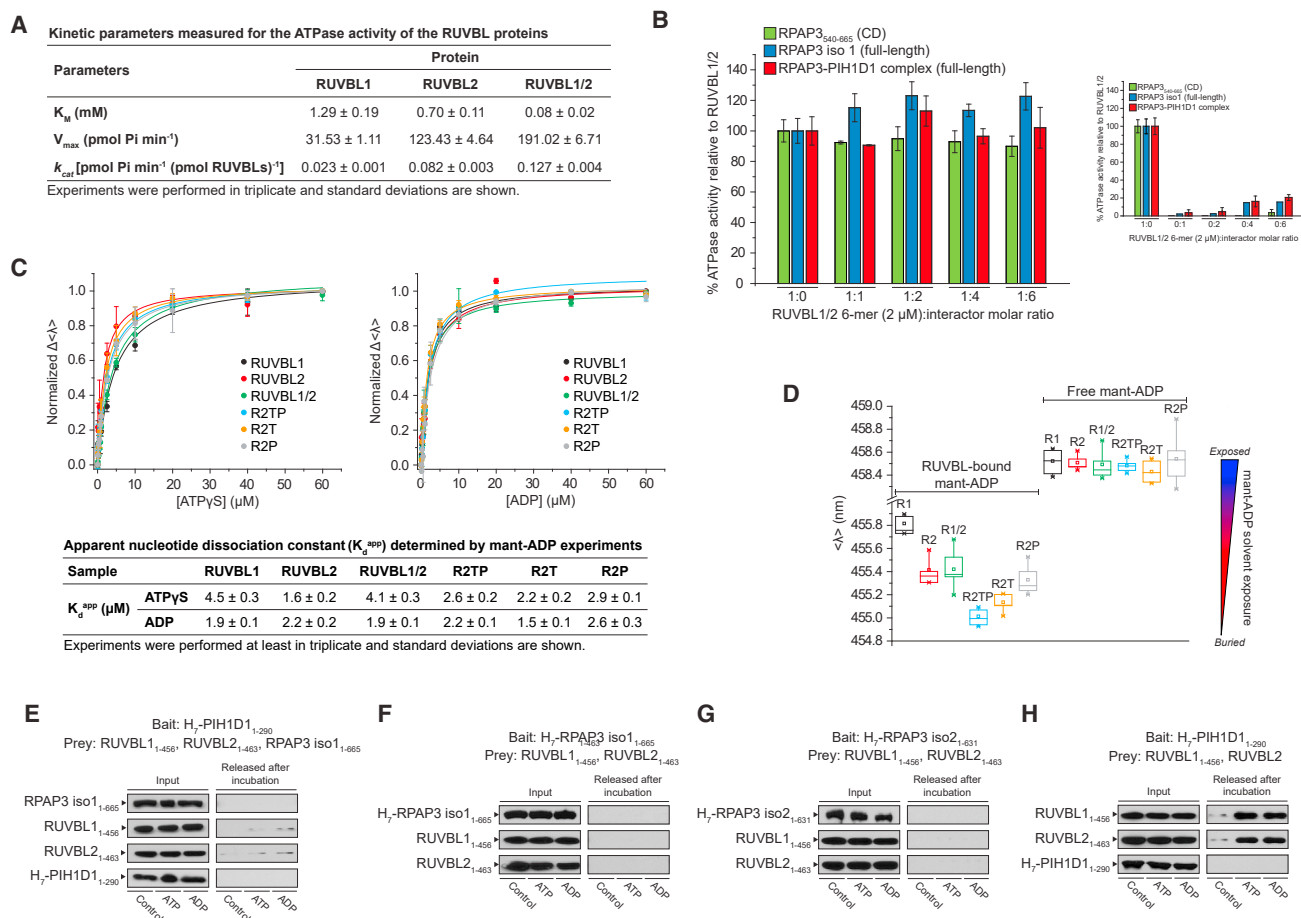


**Figure 7. ATPase activity of RUVBL1/2-related complexes and their nucleotide-binding properties**

(A) Kinetic parameters for the ATPase activity of the RUVBL proteins.

(B) Effect of RPAP3 and PIH1D1 on the RUVBL1/2 ATPase activity. The ATP hydrolysis rate of RUVBL1/2 complex (2 μM hexamer) was evaluated at increasing concentrations (2–12 μM) of RPAP3 CD, full-length RPAP3, and RPAP3-PIH1D1. Data were normalized to the ATPase rate of RUVBL1/2 complex by itself. The inset shows negligible background ATPase activity for RPAP3 CD, RPAP3 iso1, and PIH1D1. Error bars represent SD.

(C) Binding affinity of RUVBL proteins for adenosine nucleotides and effects of RPAP3, PIH1D1, and RPAP3-PIH1D1 on the RUVBL1/2 complex. Titration experiments are shown in the top panel for ATPγS (left side) and ADP (right side); SD are shown as error bars. The bottom panel displays calculated nucleotide  $K_D^{app}$  for RUVBLs, R2TP, R2T, and R2P complexes.

(D) Analysis of the environment experienced by mant-ADP in the ATP-binding pocket of RUVBL proteins based on experiments performed in (C). Shown are comparisons of centers of spectral mass for mant-ADP bound and unbound to protein. Interquartile range (large box), mean (small box), median (horizontal line), 5<sup>th</sup> and 95<sup>th</sup> percentile (whiskers) and maximum and minimum values are shown. As reference, the relative degree of solvent exposure is shown on the right.

(E–H) Effect of nucleotides on the assembled R2TP, R2T, and R2P complexes. The complexes were immobilized on Co<sup>2+</sup> ion-affinity beads via bait proteins and incubated with nucleotide solution. Prey proteins released after nucleotide addition were collected and visualized by western blots.

### The effect of nucleotides on R2TP assembly

Recently, PIH1D1 has been proposed to work as an NEF for RUVBL1/2 based on structural studies, but with no biochemical proof (Munoz-Hernandez et al., 2019). Therefore, we investigated whether RPAP3 and PIH1D1 have an impact on the ATPase activity of RUVBL1/2. Initially the ATPase activities of RUVBL1, RUVBL2, and RUVBL1/2 were measured, and the kinetic parameters are shown in Figure 7A. RUVBL2 has a more robust ATPase activity than RUVBL1, and RUVBL1/2 complex has the highest activity (refer also to Nano et al., 2020).

Subsequently, RUVBL1/2 concentration was fixed (2 μM hexamer) and RPAP3, RPAP3-PIH1D1, and RPAP3<sub>540–665</sub> (CD) were titrated into it. Only a slight increase in the ATPase activity

was observed upon addition of RPAP3 (Figure 7B). No significant effect was observed upon addition of the RPAP3 CD or RPAP3-PIH1D1 complex. Control experiments showed that RPAP3 constructs and RPAP3-PIH1D1 have negligible or little ATPase activity (Figure 7B) subtracted from RUVBL1/2-containing data.

Since RPAP3 and RPAP3-PIH1D1 did not affect the ATPase rates of RUVBL1/2, we wondered whether they could affect the binding affinity of RUVBL1/2 for nucleotides instead. To address this question, we made use of a fluorescent ADP analog (mant-ADP) to determine the apparent dissociation constant ( $K_D^{app}$ ) for the interaction of nucleotides ATPγS and ADP with RUVBLs. The mant-ADP fluorescence emission spectrum undergoes a blue shift when bound to RUVBL1/2; addition of

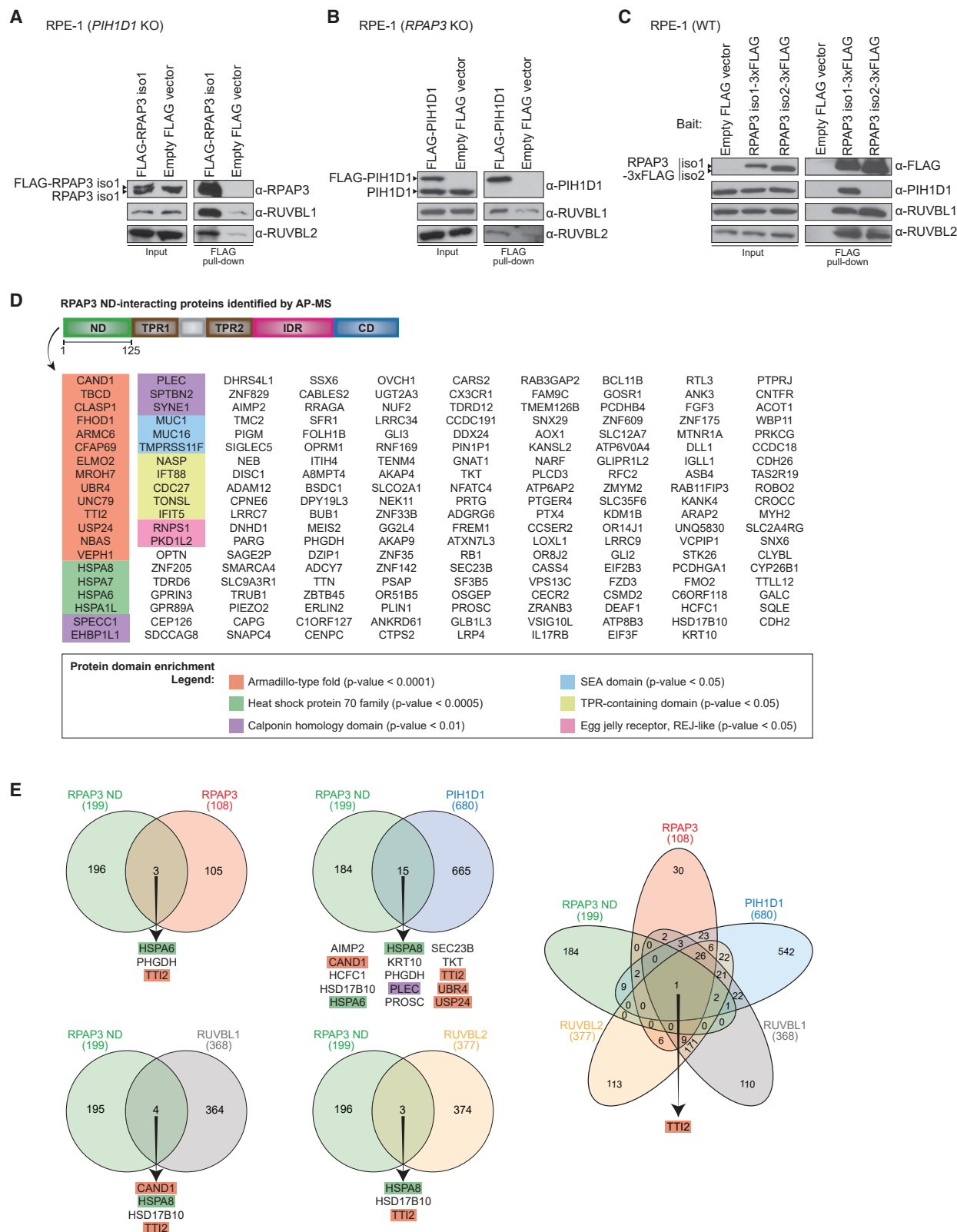


**Figure 8. The presence of R2T and R2P in cells and the identification of RPAP3 ND-interacting proteins**

(A) Pull-down of FLAG-tagged RPAP3 iso1 in RPE1 *PIH1D1* knockout cells.

(B) Pull-down of FLAG-tagged PIH1D1 in RPE1 *RPAP3* knockout cells.

(legend continued on next page)

non-fluorescent nucleotides induced dissociation of mant-ADP from RUVBL's ATP-binding pocket. Subsequently, ATP $\gamma$ S or ADP were titrated into mant-ADP-bound RUVBL1, RUVBL2, RUVBL1/2, R2TP, R2T, and R2P samples to determine the  $K_D^{app}$  of RUVBLs for nucleotides, shown in Figure 7C. All tested samples did not show significant differences in  $K_D^{app}$  for ADP; however, for ATP $\gamma$ S, RUVBL1 and RUVBL1/2 samples presented  $\sim$ 2-fold less affinity in comparison with RUVBL2, R2TP, R2T, and R2P. These results suggest that RPAP3, RPAP3-PIH1D1, and PIH1D1 do not significantly affect the affinity of RUVBL1/2 for nucleotides.

Next, using the sensitivity of mant-ADP to the physical-chemical properties of its surroundings, i.e., the spectral shift observed when mant-ADP is free (polar environment) versus protein-bound (hydrophobic environment), we analyzed the solvent accessibility of the ATP-binding pockets of RUVBLs. Figure 7D displays  $\langle\lambda\rangle$  values for RUVBL-bound and unbound mant-ADP.  $\langle\lambda\rangle$  refers to spectral center of mass (see STAR Methods). R2TP-bound mant-ADP exhibited lowest  $\langle\lambda\rangle$  values, indicating that the nucleotide-binding pocket is most protected from the polar environment in these complexes. Importantly, these results indicate that the binding of RPAP3 and RPAP3-PIH1D1 to RUVBL1/2 shields the ATP-binding pocket instead of opening it to the solvent, as proposed in previous work (Munoz-Hernandez et al., 2019).

Subsequently, we examined whether nucleotides affected the complex composition. To do so, we immobilized R2TP, R2T, and R2P complexes on Co<sup>2+</sup> beads through His-tagged RPAP3 or PIH1D1 and incubated them with buffer containing ATP, ADP, or no nucleotide. Released proteins were then visualized by western blot. None of the complexes disassembled upon nucleotide addition (Figures 7E–7G) except for the RUVBL1/2-PIH1D1 complex (Figure 7H).

Taken together, these results demonstrate that RPAP3 and RPAP3-PIH1D1 do not affect RUVBL1/2 ATPase activity or their binding affinity for nucleotides, and that only the R2P complex falls apart upon nucleotide binding to RUVBL1/2. In addition, ATP hydrolysis seems to be the rate-limiting step for RUVBL1/2 activity, since the  $K_M$  is significantly higher than the  $K_D^{app}$  (Figures 7A and 7C).

### In vivo implications for R2TP complex assembly

Our *in vitro* data indicate the presence of R2T and R2P complexes in addition to the R2TP. Using pull-downs of RPAP3 iso1 in *PIH1D1* deleted cells and of PIH1D1 in *RPAP3* deleted cells, we show that R2T and R2P, respectively can also be observed *in vivo* (Figures 8A and 8B). Furthermore, the pull-down of RPAP3 iso2 only brings down RUVBL1 and RUVBL2 and not PIH1D1 as expected (Figure 8C).

To further explore the role of the intrinsically disordered RPAP3 ND in substrate recognition, we also performed affinity purification followed by mass spectrometry (AP-MS). Using recombinant purified His<sub>12</sub>-SUMO-tagged RPAP3 ND, we pulled

down proteins from cell extracts that were then analyzed by mass spectrometry. Enrichment analysis on the identified proteins using the DAVID server (Huang et al., 2009a, 2009b) showed that RPAP3 ND preferentially binds to proteins containing Armadillo (ARM) repeats, HSP70 proteins, Calponin homology domain, SEA domains, TPR domain-containing proteins, and REJ-like structures (Figure 8D and Table S4). Of note, most of the domains present in  $\sim$ 70% of the interacting proteins are all  $\alpha$ -helical.

Comparison of RPAP3 ND interactors with R2TP interactors retrieved from BioGRID (Figure 8E) shows that TT12, which has ARM-type repeats, interacts with all four R2TP subunits and with RPAP3 ND, suggesting that TT12 might be an important component of the R2TP complex.

## DISCUSSION

In this work we have combined a series of biophysical and biochemical methods to comprehensively characterize the solution structure of human R2TP subunits and how they interact with one another to assemble the R2TP complex. Our data suggest the presence of three distinct complexes in the cell: R2T (RUVBL1-RUVBL2-RPAP3), R2P (RUVBL1-RUVBL2-PIH1D1), and R2TP (RUVBL1-RUVBL2-RPAP3-PIH1D1).

For the formation of the R2T complex (Figure 9, top panel), we propose that RPAP3 first interacts with the RUVBL1/2 AAA+ core via CD, locking RUVBL1/2 in a conformational state where the DILs are in the up position. This conformation blocks the binding of PIH1D1 to RUVBL1/2, and subsequently the RPAP3 IDR interacts with RUVBL1 DIL<sub>ext</sub> (Figure 1B) to promote the proper R2T architecture.

In the R2P complex (Figure 9, middle panel), PIH1D1 binds to RUVBL1 mainly via the  $\beta$ 5 strand of its CS domain but only in the absence of RPAP3 (Figures 1B, 4B, and S7A). In fact, the prior binding of PIH1D1 to RUVBL1/2 abolishes the RPAP3-RUVBL1/2 interaction (Figures S6A–S6C).

Contrary to what was suggested by the published cryo-EM structures (Martino et al., 2018; Munoz-Hernandez et al., 2019), here we show that, within the R2TP complex, PIH1D1 does not interact directly with RUVBL1/2 and does not act as an NEF for RUVBL1/2. We also found that RPAP3 and RPAP3-PIH1D1 have no significant effect on the ATPase activity of RUVBL1/2 (Figure 7B). RPAP3 is the link connecting PIH1D1 to and positioning it in the R2TP complex through (1) the anchoring of the RPAP3 CD on the apical surface of the RUVBL1/2 and (2) the interaction of the residues 430–441 and 492–500 in the RPAP3 IDR with RUVBL1 DIL<sub>ext</sub> (Figure 1B). This places PIH1D1 on the lower side of the RUVBL1/2 hexamer (Figure 9, bottom panel).

The association of PIH1D1 with RPAP3 is dependent on the very C terminus of PIH1D1 CS domain and residues 416–429 at the beginning of RPAP3 iso1 IDR (Figures 1B and 4A), which is in partial agreement with previously published data (Henri et al., 2018;

(C) Pull-downs of FLAG-tagged RPAP3 iso1 or RPAP3 iso2 proteins expressed in RPE1 cells.

(D) List of proteins interacting with RPAP3 ND identified by AP-MS. Protein domain enrichment analysis was performed using the DAVID server, and enriched proteins ( $p < 0.05$ ) are highlighted by colored boxes. Legend is shown in the bottom panel. See also Table S4.

(E) Venn diagram of RPAP3 ND-interacting proteins identified in this study and R2TP-interacting proteins obtained from BioGRID. Common interactors are shown below each Venn diagram, and proteins containing enriched domains are colored as in (A). Diagrams were obtained using the InteractiVenn tool.

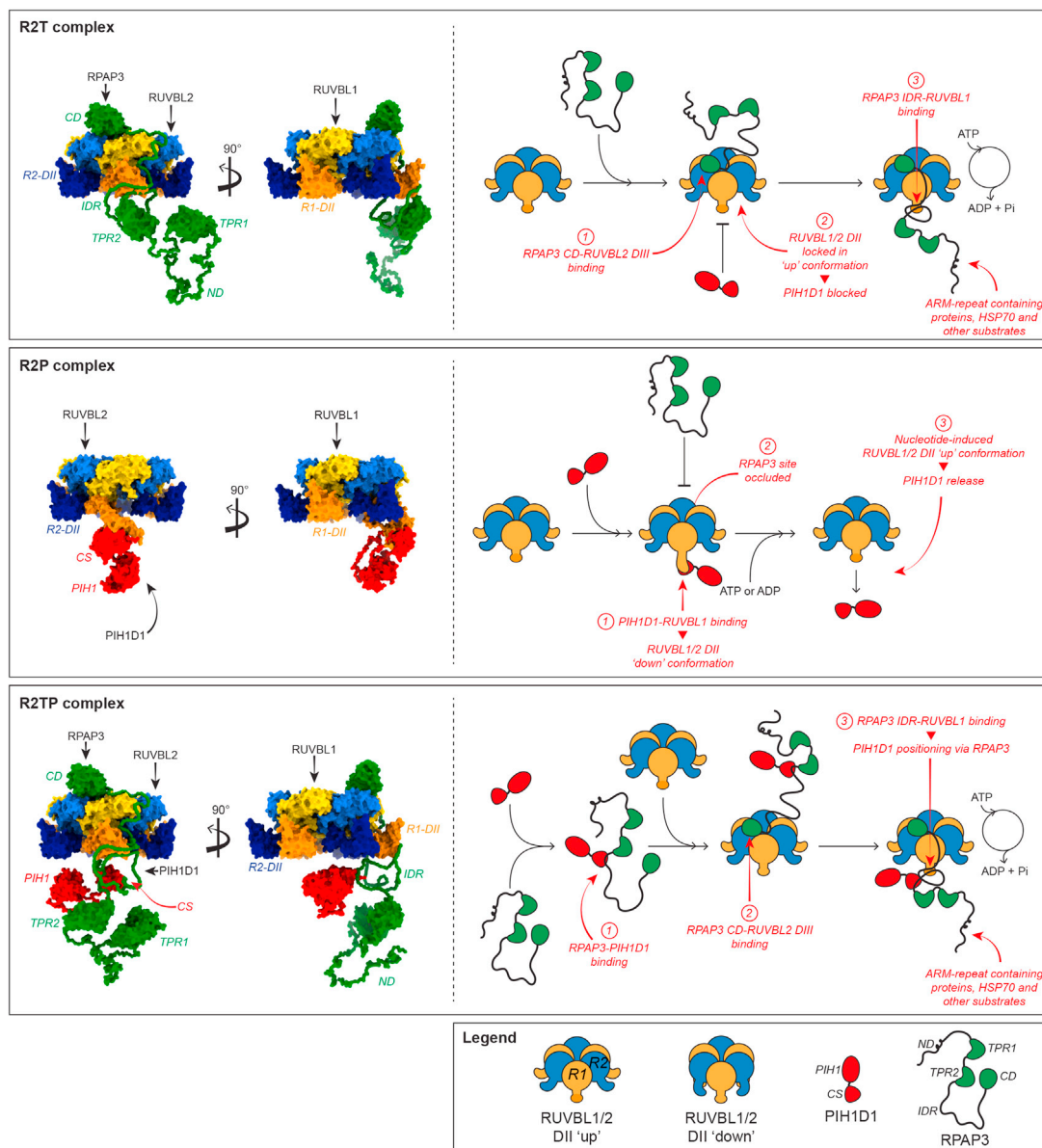


**Figure 9. Proposed model for the assembly of human R2TP, R2T, and R2P complexes**

For visualization purposes, only one RPAP3, RPAP3-PIH1D1, and PIH1D1 are shown bound to RUVBL1/2. See discussion for further details. Representative 3D structures shown were made using UCSF ChimeraX software (Pettersen et al., 2021). RUVBL1 (PDB: 2C9O), RPAP3, and PIH1D1 (hybrid SAXS models from this work) structures were employed. RUVBL1 DI + DIII are shown in yellow and RUVBL2 DI + DIII are shown in blue. DII domains of RUVBL1 and RUVBL2 are colored orange and dark blue, respectively. See also Figure S7.

Martino et al., 2018). Henri et al. (2018) had shown that the binding of PIH1D1 to RPAP3 involves extensive contacts between the two proteins, whereby the RPAP3 IDR residues 431–441 loop around the CS domain of PIH1D1 forming intermolecular  $\beta$  strands (Figure S7B). In contrast, we show that residues 416–429 of RPAP3 iso1 IDR are, in fact, responsible for binding PIH1D1. In our study, the RPAP3 IDR region reported to loop around the PIH1D1 CS domain is completely dispensable for the heterodimer formation. This region is also present in RPAP3 iso2, which does not bind to PIH1D1. The difference between our data and those of Henri et al. (2018) (Figure S7) might be due to spurious interactions induced

by crystal packing forces stabilizing the IDR of RPAP3 and the disordered C-terminal end of PIH1D1.

R2TP species containing one, two, and three bound RPAP3-PIH1D1 seem to co-exist in equilibrium (Figure 6). These observed stoichiometries, added to the RPAP3 flexibility, allow us to hypothesize that one RPAP3 and PIH1D1 in the R2TP complex may act to interact with R2TP clients, while the other two PIH1D1 subunits in complex with RPAP3 recruit other clients to R2TP. This would allow the different clients to interact and render R2TP a highly dynamic assembly platform for quaternary structure formation.

## STAR★METHODS

Detailed methods are provided in the online version of this paper and include the following:

- **KEY RESOURCES TABLE**
- **RESOURCE AVAILABILITY**
  - Lead contact
  - Materials availability
  - Data and code availability
- **EXPERIMENTAL MODEL AND SUBJECT DETAILS**
  - *Escherichia coli* cell cultures
  - *Saccharomyces cerevisiae* cell cultures
  - Mammalian cell cultures
- **METHOD DETAILS**
  - Protein expression and purification
  - *In vitro* pull-down experiments
  - *In vivo* pull-down experiments
  - Yeast two-hybrid assay
  - Analytical size exclusion chromatography (SEC)
  - Size exclusion chromatography coupled to multi-angle light scattering (SEC-MALS)
  - ATPase assays
  - Bioinformatics
  - Spectroscopy experiments
  - Analytical ultracentrifugation
  - Small angle X-ray scattering (SAXS)
  - Mant-ADP fluorescence assays
  - Mass photometry
  - Nanoflow electron spray ionization mass spectrometry (NanoESI)
  - Negative-stain electron microscopy
  - Cross-linking followed by mass spectrometry (XL-MS)
  - Affinity purification followed by mass spectrometry (AP-MS)
- **QUANTIFICATION AND STATISTICAL ANALYSIS**

## SUPPLEMENTAL INFORMATION

Supplemental information can be found online at <https://doi.org/10.1016/j.str.2021.08.002>.

## ACKNOWLEDGMENTS

T.V.S. was supported by a CNPq-Brazil (202192/2015-6), a SHRF and a CIHR (396113) postdoctoral fellowships. S.A. was supported by the Royal Golden Jubilee PhD Program of The Thailand Research Fund (PHD/0084/2553). C.C. was supported by FAPESP (2016/01603-9). Y.-Q.M. is supported by a fellowship from the Center for Pharmaceutical Oncology (University of Toronto). V.B. was supported by an Ontario Graduate Scholarship and the NSERC Postgraduate Scholarship-Doctoral award and a Jaro Sodek Award – Ontario Student Opportunity Trust Fund fellowship from the Department of Biochemistry at the University of Toronto. G.Y. was supported by a Zvi and Ofra Meitar Magdalen Graduate Scholarship. V.T. was supported by Mahidol University research grant and the Thailand Research Fund (IRN60W0004). P.K. was supported by an ERC Consolidator grant (PHOTOMASS 819593). This work was supported by a CIHR Project grant (PJT-173491) to W.A.H., and by Global Affairs Canada and CAPES (99999.004913/2015-09; Brazil) to W.A.H. and C.H.I.R. This study was partially supported by FAPESP (2015/15822-1, 2012/01953-9, 2016/05019-0) and a CNPq to L.R.S.B. who also holds a research fellowship from CNPq (306943/2015-8, 420567/2016-0). C.H.I.R. has a research fellowship from CNPq and FAPESP (2012/50161-8; 2017/

26131-5). J.C.B. has a research fellowship from CNPq and FAPESP (303262/2018-4; 2017/26131-5). M.B. is supported by a CIHR foundation grant (FDN-154318).

## AUTHOR CONTRIBUTIONS

T.V.S. and N.N. initiated this project with W.A.H. T.V.S. with the help of Y.W.S.C., S.A., and C.C. carried out or was involved in most of the experiments. S.A. was supervised by V.T., and C.C. was supervised by L.M.G. N.N. did the ATPase assays of Figure 7A and SEC experiments of Figures S2A and S2C. Y.-Q.M. did the experiments using mammalian cell cultures described in Figures 8A–8C. G.Y. under the supervision of P.K. carried out the mass photometry experiments of Figure 6. L.H., S.P., and T.V.S. under the supervision of M.B. did the mass spectrometry experiments of Figure 8D and the XL-MS experiments of Figure S4B. Y.G. under the supervision of C.V.R. did the mass spectrometry experiments of Figure S2B. D.R.S. did the EM experiments of Figure S2D. T.V.S., V.B., Y.-Q.M., J.C.B., L.R.S.B., and C.H.I.R. contributed to the SAXS experiments. T.V.S. and W.A.H. wrote the first draft of the manuscript. Everyone helped with editing of the draft.

## DECLARATION OF INTERESTS

The authors declare no competing interests. P.K. is a founder, director, and shareholder in Refeyn Ltd. G.Y. is a founder, consultant, and shareholder in Refeyn Ltd.

Received: April 19, 2021

Revised: July 16, 2021

Accepted: August 10, 2021

Published: August 30, 2021

## REFERENCES

- Andersen, K.R., Leksa, N.C., and Schwartz, T.U. (2013). Optimized *E. coli* expression strain LOBSTR eliminates common contaminants from His-tag purification. *Proteins* 81, 1857–1861. <https://doi.org/10.1002/prot.24364>.
- Aramayo, R.J., Willhoft, O., Ayala, R., Bythell-Douglas, R., Wigley, D.B., and Zhang, X. (2018). Cryo-EM structures of the human INO80 chromatin-remodeling complex. *Nat. Struct. Mol. Biol.* 25, 37–44. <https://doi.org/10.1038/s41594-017-0003-7>.
- Boulon, S., Pradet-Balade, B., Verheggen, C., Molle, D., Boireau, S., Georgieva, M., Azzag, K., Robert, M.C., Ahmad, Y., Neel, H., et al. (2010). HSP90 and its R2TP/Prefoldin-like cochaperone are involved in the cytoplasmic assembly of RNA polymerase II. *Mol. Cell* 39, 912–924. <https://doi.org/10.1016/j.molcel.2010.08.023>.
- Buchan, D.W.A., and Jones, D.T. (2019). The PSIPRED protein analysis workbench: 20 years on. *Nucleic Acids Res.* 47, W402–W407. <https://doi.org/10.1093/nar/gkz297>.
- Chemes, L.B., Alonso, L.G., Noval, M.G., and de Prat-Gay, G. (2012). Circular dichroism techniques for the analysis of intrinsically disordered proteins and domains. *Methods Mol. Biol.* 895, 387–404. [https://doi.org/10.1007/978-1-61779-927-3\\_22](https://doi.org/10.1007/978-1-61779-927-3_22).
- Chernushevich, I.V., and Thomson, B.A. (2004). Collisional cooling of large ions in electrospray mass spectrometry. *Anal. Chem.* 76, 1754–1760. <https://doi.org/10.1021/ac035406j>.
- Cheung, K.L., Huen, J., Kakiyama, Y., Houry, W.A., and Ortega, J. (2010). Alternative oligomeric states of the yeast Rvb1/Rvb2 complex induced by histidine tags. *J. Mol. Biol.* 404, 478–492. <https://doi.org/10.1016/j.jmb.2010.10.003>.
- Cloutier, P., Poitras, C., Durand, M., Hekmat, O., Fiola-Masson, E., Bouchard, A., Faubert, D., Chabot, B., and Coulombe, B. (2017). R2TP/Prefoldin-like component RUVBL1/RUVBL2 directly interacts with ZNHIT2 to regulate assembly of U5 small nuclear ribonucleoprotein. *Nat. Commun.* 8, 15615. <https://doi.org/10.1038/ncomms15615>.
- Cole, D., Young, G., Weigel, A., Sebesta, A., and Kukura, P. (2017). Label-free single-molecule imaging with numerical-aperture-shaped interferometric

- scattering microscopy. *ACS Photon.* 4, 211–216. <https://doi.org/10.1021/acsp Photonics.6b00912>.
- Crooks, G.E., Hon, G., Chandonia, J.M., and Brenner, S.E. (2004). WebLogo: a sequence logo generator. *Genome Res.* 14, 1188–1190. <https://doi.org/10.1101/gr.849004>.
- Delorenzi, M., and Speed, T. (2002). An HMM model for coiled-coil domains and a comparison with PSSM-based predictions. *Bioinformatics* 18, 617–625. <https://doi.org/10.1093/bioinformatics/18.4.617>.
- Eng, J.K., McCormack, A.L., and Yates, J.R. (1994). An approach to correlate tandem mass spectral data of peptides with amino acid sequences in a protein database. *J. Am. Soc. Mass Spectrom.* 5, 976–989. [https://doi.org/10.1016/1044-0305\(94\)80016-2](https://doi.org/10.1016/1044-0305(94)80016-2).
- Ewens, C.A., Su, M., Zhao, L., Nano, N., Houry, W.A., and Southworth, D.R. (2016). Architecture and nucleotide-dependent conformational changes of the Rvb1-Rvb2 AAA+ complex revealed by cryoelectron microscopy. *Structure* 24, 657–666. <https://doi.org/10.1016/j.str.2016.03.018>.
- Franke, D., Petoukhov, M.V., Konarev, P.V., Panjkovich, A., Tuukkanen, A., Mertens, H.D.T., Kikhney, A.G., Hajizadeh, N.R., Franklin, J.M., Jeffries, C.M., and Svergun, D.I. (2017). Atsas 2.8: a comprehensive data analysis suite for small-angle scattering from macromolecular solutions. *J. Appl. Crystallogr.* 50, 1212–1225. <https://doi.org/10.1107/S1600576717007786>.
- Franke, D., and Svergun, D.I. (2009). DAMMIF, a program for rapid ab-initio shape determination in small-angle scattering. *J. Appl. Crystallogr.* 42, 342–346. <https://doi.org/10.1107/S0021889809000338>.
- Gorynia, S., Bandejas, T.M., Pinho, F.G., McVey, C.E., Vonrhein, C., Round, A., Svergun, D.I., Donner, P., Matias, P.M., and Carrondo, M.A. (2011). Structural and functional insights into a dodecameric molecular machine—the RuvBL1/RuvBL2 complex. *J. Struct. Biol.* 176, 279–291. <https://doi.org/10.1016/j.jsb.2011.09.001>.
- Graham, M., Combe, C., Kolbowski, L., and Rappsilber, J. (2019). xView: a common platform for the downstream analysis of crosslinking mass spectrometry data. *bioRxiv*, 561829. <https://doi.org/10.1101/561829>.
- Heberle, H., Meirelles, G.V., da Silva, F.R., Telles, G.P., and Minghim, R. (2015). InteractiVenn: a web-based tool for the analysis of sets through Venn diagrams. *BMC Bioinformatics* 16, 169. <https://doi.org/10.1186/s12859-015-0611-3>.
- Henri, J., Chagot, M.E., Bourguet, M., Abel, Y., Terral, G., Maurizy, C., Aigueperse, C., Georgescauld, F., Vandermoere, F., Saint-Fort, R., et al. (2018). Deep structural analysis of RPAP3 and PIH1D1, two components of the HSP90 co-chaperone R2TP complex. *Structure* 26, 1196–1209.e8. <https://doi.org/10.1016/j.str.2018.06.002>.
- Hernandez, H., and Robinson, C.V. (2007). Determining the stoichiometry and interactions of macromolecular assemblies from mass spectrometry. *Nat. Protoc.* 2, 715–726. <https://doi.org/10.1038/nprot.2007.73>.
- Horejsi, Z., Stach, L., Flower, T.G., Joshi, D., Flynn, H., Skehel, J.M., O'Reilly, N.J., Ogradowicz, R.W., Smerdon, S.J., and Boulton, S.J. (2014). Phosphorylation-dependent PIH1D1 interactions define substrate specificity of the R2TP co-chaperone complex. *Cell Rep.* 7, 19–26. <https://doi.org/10.1016/j.celrep.2014.03.013>.
- Horejsi, Z., Takai, H., Adelman, C.A., Collis, S.J., Flynn, H., Maslen, S., Skehel, J.M., de Lange, T., and Boulton, S.J. (2010). CK2 phospho-dependent binding of R2TP complex to TEL2 is essential for mTOR and SMG1 stability. *Mol. Cell* 39, 839–850. <https://doi.org/10.1016/j.molcel.2010.08.037>.
- Houry, W.A., Bertrand, E., and Coulombe, B. (2018). The PAQosome, an R2TP-based chaperone for quaternary structure formation. *Trends Biochem. Sci.* 43, 4–9. <https://doi.org/10.1016/j.tibs.2017.11.001>.
- Huang, D.W., Sherman, B.T., and Lempicki, R.A. (2009a). Bioinformatics enrichment tools: paths toward the comprehensive functional analysis of large gene lists. *Nucleic Acids Res.* 37, 1–13. <https://doi.org/10.1093/nar/gkn923>.
- Huang, D.W., Sherman, B.T., and Lempicki, R.A. (2009b). Systematic and integrative analysis of large gene lists using DAVID bioinformatics resources. *Nat. Protoc.* 4, 44–57. <https://doi.org/10.1038/nprot.2008.211>.
- James, P., Halladay, J., and Craig, E.A. (1996). Genomic libraries and a host strain designed for highly efficient two-hybrid selection in yeast. *Genetics* 144, 1425–1436.
- Kamano, Y., Saeki, M., Egusa, H., Kakiyama, Y., Houry, W.A., Yatani, H., and Kamisaki, Y. (2013). PIH1D1 interacts with mTOR complex 1 and enhances ribosome RNA transcription. *FEBS Lett.* 587, 3303–3308. <https://doi.org/10.1016/j.febslet.2013.09.001>.
- Kikhney, A.G., and Svergun, D.I. (2015). A practical guide to small angle X-ray scattering (SAXS) of flexible and intrinsically disordered proteins. *FEBS Lett.* 589, 2570–2577. <https://doi.org/10.1016/j.febslet.2015.08.027>.
- Kozin, M.B., and Svergun, D.I. (2001). Automated matching of high- and low-resolution structural models. *J. Appl. Crystallogr.* 34, 33–41. <https://doi.org/10.1107/s0021889800014126>.
- Lakomek, K., Stoeck, G., Tosi, A., Schmailzl, M., and Hopfner, K.P. (2015). Structural basis for dodecameric assembly states and conformational plasticity of the full-length AAA+ ATPases Rvb1. Rvb2. *Struct.* 23, 483–495. <https://doi.org/10.1016/j.str.2014.12.015>.
- Laskowski, R.A., Jablonska, J., Pravda, L., Váreková, R.S., and Thornton, J.M. (2018). PDBsum: structural summaries of PDB entries. *Protein Sci.* 27, 129–134. <https://doi.org/10.1002/pro.3289>.
- Lee, C.D., Sun, H.C., Hu, S.M., Chiu, C.F., Homhuan, A., Liang, S.M., Leng, C.H., and Wang, T.F. (2008). An improved SUMO fusion protein system for effective production of native proteins. *Protein Sci.* 17, 1241–1248. <https://doi.org/10.1110/ps.035188.108>.
- Liu, F., Rijkers, D.T., Post, H., and Heck, A.J. (2015). Proteome-wide profiling of protein assemblies by cross-linking mass spectrometry. *Nat. Methods* 12, 1179–1184. <https://doi.org/10.1038/nmeth.3603>.
- Lopez-Perrote, A., Munoz-Hernandez, H., Gil, D., and Llorca, O. (2012). Conformational transitions regulate the exposure of a DNA-binding domain in the RuvBL1-RuvBL2 complex. *Nucleic Acids Res.* 40, 11086–11099. <https://doi.org/10.1093/nar/gks871>.
- Ludtke, S.J., Baldwin, P.R., and Chiu, W. (1999). EMAN: semiautomated software for high-resolution single-particle reconstructions. *J. Struct. Biol.* 128, 82–97. <https://doi.org/10.1006/jsbi.1999.4174>.
- Machado-Pinilla, R., Liger, D., Leulliot, N., and Meier, U.T. (2012). Mechanism of the AAA+ ATPases pontin and reptin in the biogenesis of H/ACA RNPs. *RNA* 18, 1833–1845. <https://doi.org/10.1261/ma.034942.112>.
- Madeira, F., Park, Y.M., Lee, J., Buso, N., Gur, T., Madhusoodanan, N., Basutkar, P., Tivey, A.R.N., Potter, S.C., Finn, R.D., and Lopez, R. (2019). The EMBL-EBI search and sequence analysis tools APIs in 2019. *Nucleic Acids Res.* 47, W636–w641. <https://doi.org/10.1093/nar/gkz268>.
- Malinova, A., Cvackova, Z., Mateju, D., Horejsi, Z., Abeza, C., Vandermoere, F., Bertrand, E., Stanek, D., and Verheggen, C. (2017). Assembly of the U5 snRNP component PRPF8 is controlled by the HSP90/R2TP chaperones. *J. Cell Biol.* 216, 1579–1596. <https://doi.org/10.1083/jcb.201701165>.
- Martino, F., Pal, M., Munoz-Hernandez, H., Rodriguez, C.F., Nunez-Ramirez, R., Gil-Carton, D., Degliesposti, G., Skehel, J.M., Roe, S.M., Prodromou, C., et al. (2018). RPAP3 provides a flexible scaffold for coupling HSP90 to the human R2TP co-chaperone complex. *Nat. Commun.* 9, 1501. <https://doi.org/10.1038/s41467-018-03942-1>.
- Matias, P.M., Gorynia, S., Donner, P., and Carrondo, M.A. (2006). Crystal structure of the human AAA+ protein RuvBL1. *J. Biol. Chem.* 281, 38918–38929. <https://doi.org/10.1074/jbc.M605625200>.
- Maurizy, C., Quinteret, M., Abel, Y., Verheggen, C., Santo, P.E., Bourguet, M., Paiva, A.C.F., Bragantini, B., Chagot, M.E., Robert, M.C., et al. (2018). The RPAP3-C terminal domain identifies R2TP-like quaternary chaperones. *Nat. Commun.* 9, 2093. <https://doi.org/10.1038/s41467-018-04431-1>.
- Mellacheruvu, D., Wright, Z., Couzens, A.L., Lambert, J.P., St-Denis, N.A., Li, T., Miteva, Y.V., Hauri, S., Sardi, M.E., Low, T.Y., et al. (2013). The CRAPome: a contaminant repository for affinity purification-mass spectrometry data. *Nat. Methods* 10, 730–736. <https://doi.org/10.1038/nmeth.2557>.
- Mir, R.A., Bele, A., Mirza, S., Srivastava, S., Olu, A.A., Ammons, S.A., Kim, J.H., Gurumurthy, C.B., Qiu, F., Band, H., and Band, V. (2015). A novel interaction of Ecdysoneless (ECD) protein with R2TP complex component RUVBL1 is

required for the functional role of ECD in cell cycle progression. *Mol. Cell. Biol.* 36, 886–899. <https://doi.org/10.1128/MCB.00594-15>.

Munoz-Hernandez, H., Pal, M., Rodriguez, C.F., Fernandez-Leiro, R., Prodromou, C., Pearl, L.H., and Llorca, O. (2019). Structural mechanism for regulation of the AAA-ATPases RUVBL1-RUVBL2 in the R2TP co-chaperone revealed by cryo-EM. *Sci. Adv.* 5, eaaw1616. <https://doi.org/10.1126/sciadv.aaw1616>.

Nano, N., Ugwu, F., Seraphim, T.V., Li, T., Azer, G., Isaac, M., Prakesch, M., Barbosa, L.R.S., Ramos, C.H.I., Datti, A., and Houry, W.A. (2020). Sorafenib as an inhibitor of RUVBL2. *Biomolecules* 10. <https://doi.org/10.3390/biom10040605>.

Norby, J.G. (1988). Coupled assay of Na<sup>+</sup>,K<sup>+</sup>-ATPase activity. *Methods Enzymol.* 156, 116–119. [https://doi.org/10.1016/0076-6879\(88\)56014-7](https://doi.org/10.1016/0076-6879(88)56014-7).

Ohi, M., Li, Y., Cheng, Y., and Walz, T. (2004). Negative staining and image classification—powerful tools in modern electron microscopy. *Biol. Proced. Online* 6, 23–34. <https://doi.org/10.1251/bpo70>.

Pal, M., Morgan, M., Phelps, S.E., Roe, S.M., Parry-Morris, S., Downs, J.A., Polier, S., Pearl, L.H., and Prodromou, C. (2014). Structural basis for phosphorylation-dependent recruitment of Tel2 to hsp90 by Pih1. *Structure* 22, 805–818. <https://doi.org/10.1016/j.str.2014.04.001>.

Pal, M., Muñoz-Hernandez, H., Bjorklund, D., Zhou, L., Degliesposti, G., Skehel, J.M., Hesketh, E.L., Thompson, R.F., Pearl, L.H., Llorca, O., and Prodromou, C. (2021). Structure of the TEO2-TT11-TT12 complex and its function in TOR recruitment to the R2TP chaperone. *Cell Rep.* 36, 109317. <https://doi.org/10.1016/j.celrep.2021.109317>.

Park, A.Y., Jergic, S., Politis, A., Ruotolo, B.T., Hirshberg, D., Jessop, L.L., Beck, J.L., Barsky, D., O'Donnell, M., Dixon, N.E., and Robinson, C.V. (2010). A single subunit directs the assembly of the *Escherichia coli* DNA sliding clamp loader. *Structure* 18, 285–292. <https://doi.org/10.1016/j.str.2010.01.009>.

Petoukhov, M.V., Franke, D., Shkumatov, A.V., Tria, G., Kikhney, A.G., Gajda, M., Gorba, C., Mertens, H.D., Konarev, P.V., and Svergun, D.I. (2012). New developments in the ATSAS program package for small-angle scattering data analysis. *J. Appl. Crystallogr.* 45, 342–350. <https://doi.org/10.1107/S0021889812007662>.

Pettersen, E.F., Goddard, T.D., Huang, C.C., Meng, E.C., Couch, G.S., Croll, T.I., Morris, J.H., and Ferrin, T.E. (2021). UCSF ChimeraX: structure visualization for researchers, educators, and developers. *Protein Sci.* 30, 70–82. <https://doi.org/10.1002/pro.3943>.

Petukhov, M., Dagkessamanskaja, A., Bommer, M., Barrett, T., Tsaneva, I., Yakimov, A., Queval, R., Shvetsov, A., Khodorkovskiy, M., Kas, E., and Grigoriev, M. (2012). Large-scale conformational flexibility determines the properties of AAA+ TAP49 ATPases. *Structure* 20, 1321–1331. <https://doi.org/10.1016/j.str.2012.05.012>.

Rivera-Calzada, A., Pal, M., Munoz-Hernandez, H., Luque-Ortega, J.R., Gil-Carton, D., Degliesposti, G., Skehel, J.M., Prodromou, C., Pearl, L.H., and Llorca, O. (2017). The structure of the R2TP complex defines a platform for recruiting diverse client proteins to the HSP90 molecular chaperone system. *Structure* 25, 1145–1152.e4. <https://doi.org/10.1016/j.str.2017.05.016>.

Scheich, C., Kummel, D., Soumailakakis, D., Heinemann, U., and Bussow, K. (2007). Vectors for co-expression of an unrestricted number of proteins. *Nucleic Acids Res.* 35, e43. <https://doi.org/10.1093/nar/gkm067>.

Schuck, P. (2000). Size-distribution analysis of macromolecules by sedimentation velocity ultracentrifugation and lamm equation modeling. *Biophys. J.* 78, 1606–1619. [https://doi.org/10.1016/S0006-3495\(00\)76713-0](https://doi.org/10.1016/S0006-3495(00)76713-0).

Seraphim, T.V., and Houry, W.A. (2020). AAA+ proteins. *Curr. Biol.* 30, R251–R257. <https://doi.org/10.1016/j.cub.2020.01.044>.

Silva, S.T.N., Brito, J.A., Arranz, R., Sorzano, C.O.S., Ebel, C., Douth, J., Tully, M.D., Carazo, J.M., Carrascosa, J.L., Matias, P.M., and Bandejas, T.M. (2018). X-ray structure of full-length human RuvB-Like 2—mechanistic insights into coupling between ATP binding and mechanical action. *Sci. Rep.* 8, 13726. <https://doi.org/10.1038/s41598-018-31997-z>.

Silva-Martin, N., Daudén, M.I., Glatt, S., Hoffmann, N.A., Kastiris, P., Bork, P., Beck, M., and Müller, C.W. (2016). The combination of X-ray crystallography and cryo-electron microscopy provides insight into the overall architecture of the dodecameric Rvb1/Rvb2 complex. *PLoS One* 11, e0146457. <https://doi.org/10.1371/journal.pone.0146457>.

Sobott, F., Hernandez, H., McCammon, M.G., Tito, M.A., and Robinson, C.V. (2002). A tandem mass spectrometer for improved transmission and analysis of large macromolecular assemblies. *Anal. Chem.* 74, 1402–1407. <https://doi.org/10.1021/ac0110552>.

Svergun, D. (1992). Determination of the regularization parameter in indirect-transform methods using perceptual criteria. *J. Appl. Crystallogr.* 25, 495–503. <https://doi.org/10.1107/S0021889892001663>.

Svergun, D.I. (1999). Restoring low resolution structure of biological macromolecules from solution scattering using simulated annealing. *Biophys. J.* 76, 2879–2886. [https://doi.org/10.1016/S0006-3495\(99\)77443-6](https://doi.org/10.1016/S0006-3495(99)77443-6).

Tria, G., Mertens, H.D., Kachala, M., and Svergun, D.I. (2015). Advanced ensemble modelling of flexible macromolecules using X-ray solution scattering. *IUCrJ* 2, 207–217. <https://doi.org/10.1107/S205225251500202X>.

Volkov, V.V., and Svergun, D.I. (2003). Uniqueness of ab initio shape determination in small-angle scattering. *J. Appl. Crystallogr.* 36, 860–864. <https://doi.org/10.1107/S0021889803000268>.

von Morgen, P., Burdova, K., Flower, T.G., O'Reilly, N.J., Boulton, S.J., Smerdon, S.J., Macurek, L., and Horejsi, Z. (2017). MRE11 stability is regulated by CK2-dependent interaction with R2TP complex. *Oncogene* 36, 4943–4950. <https://doi.org/10.1038/onc.2017.99>.

Wu, Z., Malt, R., Moutaoufik, M.T., Zhang, Q., Jessulat, M., and Babu, M. (2019). A tag-based affinity purification mass spectrometry workflow for systematic isolation of the human mitochondrial protein complexes. *Adv. Exp. Med. Biol.* 1158, 83–100. [https://doi.org/10.1007/978-981-13-8367-0\\_6](https://doi.org/10.1007/978-981-13-8367-0_6).

Yildiz, A., Forkey, J.N., McKinney, S.A., Ha, T., Goldman, Y.E., and Selvin, P.R. (2003). Myosin V walks hand-over-hand: single fluorophore imaging with 1.5-nm localization. *Science* 300, 2061–2065. <https://doi.org/10.1126/science.1084398>.

Yoshida, M., Saeki, M., Egusa, H., Irie, Y., Kamano, Y., Uruguchi, S., Sotozono, M., Niwa, H., and Kamisaki, Y. (2013). RPAP3 splicing variant isoform 1 interacts with PIH1D1 to compose R2TP complex for cell survival. *Biochem. Biophys. Res. Commun.* 430, 320–324. <https://doi.org/10.1016/j.bbrc.2012.11.017>.

Young, G., Hundt, N., Cole, D., Fineberg, A., Andrecka, J., Tyler, A., Olerinyova, A., Ansari, A., Marklund, E.G., Collier, M.P., et al. (2018). Quantitative mass imaging of single biological macromolecules. *Science* 360, 423–427. <https://doi.org/10.1126/science.aar5839>.

Zhao, R., Davey, M., Hsu, Y.C., Kaplanek, P., Tong, A., Parsons, A.B., Krogan, N., Cagney, G., Mai, D., Greenblatt, J., et al. (2005). Navigating the chaperone network: an integrative map of physical and genetic interactions mediated by the hsp90 chaperone. *Cell* 120, 715–727. <https://doi.org/10.1016/j.cell.2004.12.024>.

Zur Lage, P., Stefanopoulou, P., Styczynska-Soczka, K., Quinn, N., Mali, G., von Kriegsheim, A., Mill, P., and Jarman, A.P. (2018). Ciliary dynein motor pre-assembly is regulated by Wdr92 in association with HSP90 co-chaperone, R2TP. *J. Cell Biol.* 217, 2583–2598. <https://doi.org/10.1083/jcb.201709026>.

## STAR★METHODS

## KEY RESOURCES TABLE

REAGENT or RESOURCE	SOURCE	IDENTIFIER
<b>Antibodies</b>		
Rabbit polyclonal anti-RUVBL1	Abcam	Cat#ab109330; RRID: AB_11144720
Rabbit polyclonal anti-RUVBL1	Invitrogen	Cat#PA5-29278; RRID: AB_2546754
Rabbit polyclonal anti-RUVBL2	Abcam	Cat#ab36569; RRID: AB_2301439
Rabbit polyclonal anti-RUVBL2	Invitrogen	Cat#PA5-29871; RRID: AB_2547345
Rabbit polyclonal anti-RPAP3	Invitrogen	Cat#PA5-30816; RRID: AB_2548290
Mouse monoclonal anti-PIH1D1	Santa Cruz	Cat#sc-101000; RRID: AB_2164959
Mouse monoclonal anti-FLAG M2	Millipore	Cat#F3165; RRID: AB_259529
Mouse monoclonal anti-His tag	Millipore	Cat#05-949; RRID: AB_492660
Mouse monoclonal anti-His tag	Bio-Rad	Cat#MCA1396; RRID: AB_322084
<b>Bacterial and virus strains</b>		
<i>Escherichia coli</i> LOBSTR BI21(DE3) strain	(Andersen et al., 2013)	N/A
<b>Chemicals, peptides, and recombinant proteins</b>		
Adenosine 5'-triphosphate disodium salt hydrate	Bioshop	Cat#ATP007
Adenosine 5'-diphosphate sodium salt	Sigma-Aldrich	Cat#A2754
Adenosine 5'-( $\gamma$ -thio)-triphosphate (lithium salt)	Cayman Chemicals	Cat#14957
3-amino-1,2,4-triazole	Sigma-Aldrich	Cat#A8056
Phospho(enol)pyruvic acid monopotassium salt	Sigma-Aldrich	Cat#P7127
NADH disodium salt, trihydrate, reduced	Bio Basic	Cat#NB0642
Pyruvate Kinase/Lactic Dehydrogenase	Sigma-Aldrich	Cat#P0294
2'/3'-O-(N-Methyl-anthraniloyl)-adenosine-5'-diphosphate, triethylammonium salt (mant-ADP)	Jena Bioscience	Cat#JBNU201S
Disuccinimidyl sulfoxide (DSSO)	Thermo Fisher Scientific	Cat#A33545
Tobacco Etch Virus (TEV) protease	Laboratory of Walid Houry, University of Toronto	N/A
Ulp1 protease	(Lee et al., 2008)	N/A
ProteaseMAX	Promega	V2071
Trypsin Gold	Promega	V5280
25 mM Tris-HCl (pH 7.5), 500 mM NaCl	N/A	Buffer A
25 mM Tris-HCl (pH 7.5), 500 mM NaCl, 500 mM imidazole	N/A	Buffer B
25 mM Tris-HCl (pH 7.5), 50 mM KCl, 10% glycerol, 1 mM DTT	N/A	Buffer C
25 mM Tris-HCl (pH 7.5), 500 mM KCl, 10% glycerol, 1 mM DTT	N/A	Buffer D
40 mM Tris-HCl (pH 7.5), 200 mM KCl, 5 mM MgCl <sub>2</sub> , 1 mM DTT, 10% Glycerol	N/A	Buffer E
25 mM Tris-HCl (pH 7.5), 200 mM NaCl, 10% glycerol	N/A	Buffer F
25 mM Tris-HCl (pH 7.5), 50 mM NaCl	N/A	Buffer G
25 mM Tris-HCl (pH 7.5), 500 mM NaCl	N/A	Buffer H
25 mM Tris-HCl (pH 7.5), 200 mM NaCl	N/A	Buffer I

(Continued on next page)

**Continued**

REAGENT or RESOURCE	SOURCE	IDENTIFIER
25 mM Tris-HCl (pH 7.5), 200 mM NaCl, 250 mM imidazole	N/A	Buffer J
20 mM Tris-HCl, pH 7.5, 200 mM KCl, 8 mM MgCl <sub>2</sub> , 10% (v/v) glycerol	N/A	Buffer K
25 mM Tris-HCl (pH 7.5), 200 mM NaCl, 1 mM DTT, 10% glycerol	N/A	Buffer L
25 mM HEPES (pH 7.5), 200 mM NaCl, 5% glycerol	N/A	Buffer M
50 mM Tris-HCl (pH 7.4), 150 mM NaCl, 1 mM EDTA, 1% Triton X-100	N/A	Buffer N
50 mM Tris-HCl (pH 7.4), 150 mM NaCl, 0.05% Nonidet P-40	N/A	Buffer O
50 mM Tris-HCl (pH 7.4), 150 mM NaCl	N/A	Buffer P
40 mM Tris-HCl (pH 7.5), 200 mM KCl, 5 mM MgCl <sub>2</sub>	N/A	Buffer Q

**Deposited data**

Human RUVBL1 structure	(Matias et al., 2006)	PDB: 2C9O
Human RUVBL2 structure	(Silva et al., 2018)	PDB: 6H7X
Human RUVBL1/2 structure	(Aramayo et al., 2018)	PDB: 5OAF
Human RUVBL2ΔDII <sub>ext</sub> structure	(Petukhov et al., 2012)	PDB: 3UK6
Human RUVBL1ΔDII <sub>ext</sub> /2ΔDII <sub>ext</sub> complex structure	(Gorynia et al., 2011)	PDB: 2XSZ
<i>Chaetomium thermophilum</i> Rvb1/2 complex structure	(Silva-Martin et al., 2016)	PDB: 6FM6
Human RPAP3 TPR1 domain	(Pal et al., 2014)	PDB: 4CGV
Human RPAP3 TPR2 domain	(Henri et al., 2018)	PDB: 6FDT
Human RPAP3 C-domain	(Maurizy et al., 2018)	PDB: 6EZ4
Human RPAP3 TPR2-PIH1D1 CS complex structure	(Henri et al., 2018)	PDB: 6GXZ
Human PIH1D1 PIH1 domain	(Horejsi et al., 2014)	PDB: 4PSF

**Experimental models: Cell lines**

HEK293T	A gift from Dr. Liliana Attisano, University of Toronto	N/A
RPE-1	A gift from Dr. Peter Kim, The Hospital for Sick Children	N/A
RPE-1 <i>RPAP3</i> KO	This paper	N/A
RPE-1 <i>PIH1D1</i> KO	This paper	N/A

**Experimental models: Organisms/strains**

<i>Saccharomyces cerevisiae</i> PJ69-4α strain	(James et al., 1996)	N/A
--	----------------------	-----

**Recombinant DNA**

pACYC RIL (pRIL)	Agilent	N/A
pQLink H <sub>7</sub> -RUVBL1 <sub>1-456</sub>	This paper	N/A
pQLink H <sub>7</sub> -RUVBL2 <sub>1-463</sub>	This paper	N/A
p11 H <sub>6</sub> -RUVBL1 <sub>1-456</sub>	This paper	N/A
p11 H <sub>6</sub> -RUVBL2 <sub>1-463</sub>	This paper	N/A
pETSUMO2 H <sub>12</sub> -SUMO-RPAP3 iso1 <sub>1-665</sub>	This paper	N/A
pCOLA Duet-1 RPAP3 iso1 <sub>1-665</sub> , H <sub>6</sub> -PIH1D1 <sub>1-290</sub>	This paper	N/A
pQM18 H <sub>6</sub> -PIH1D1 <sub>1-290</sub> -H <sub>6</sub>	(Machado-Pinilla et al., 2012)	N/A
pCOLADuet-1 RPAP3 iso1 <sub>1-665</sub> , H <sub>6</sub> -PIH1D1 <sub>1-280</sub>	This paper	N/A

(Continued on next page)

**Continued**

REAGENT or RESOURCE	SOURCE	IDENTIFIER
pCOLADuet-1 RPAP3 iso1 <sub>1-430</sub> , H <sub>6</sub> -PIH1D1 <sub>1-290</sub>	This paper	N/A
pCOLADuet-1 RPAP3 iso1 <sub>1-415</sub> , H <sub>6</sub> -PIH1D1 <sub>1-290</sub>	This paper	N/A
pCOLADuet-1 RPAP3 iso1 <sub>1-390</sub> , H <sub>6</sub> -PIH1D1 <sub>1-290</sub>	This paper	N/A
pQLink RUVBL1 <sub>1-456</sub> -RUVBL2 <sub>1-463</sub>	This paper	N/A
pQLink RUVBL1 <sub>1-456</sub> , RUVBL2 <sub>1-463</sub> , H <sub>7</sub> -PIH1D1 <sub>1-290</sub>	This paper	N/A
pQLink RUVBL1 <sub>1-456</sub> , RUVBL2 <sub>1-463</sub> , H <sub>7</sub> -PIH1D1 <sub>1-280</sub>	This paper	N/A
pQLink RUVBL1 <sub>1-456</sub> , RUVBL2 <sub>1-463</sub> , H <sub>7</sub> -PIH1D1 <sub>1-270</sub>	This paper	N/A
pQLink RUVBL1 <sub>1-456</sub> , RUVBL2 <sub>1-463</sub> , H <sub>7</sub> -PIH1D1 <sub>1-260</sub>	This paper	N/A
pQLink RUVBL1 <sub>1-456</sub> , RUVBL2 <sub>1-463</sub> , H <sub>7</sub> -PIH1D1 <sub>1-250</sub>	This paper	N/A
pQLink RUVBL1 <sub>1-456</sub> , RUVBL2 <sub>1-463</sub> , H <sub>7</sub> -PIH1D1 <sub>1-240</sub>	This paper	N/A
pQLink RUVBL1 <sub>1-456</sub> , H <sub>7</sub> -PIH1D1 <sub>1-290</sub>	This paper	N/A
pQLink RUVBL2 <sub>1-463</sub> , H <sub>7</sub> -PIH1D1 <sub>1-290</sub>	This paper	N/A
pQLink RUVBL1 <sub>Δ126-234</sub> , RUVBL2 <sub>Δ133-238</sub>	This paper	N/A
pQLink RUVBL1 <sub>Δ126-234</sub> , RUVBL2 <sub>1-463</sub>	This paper	N/A
pQLink RUVBL1 <sub>1-456</sub> , RUVBL2 <sub>1-463</sub> , H <sub>7</sub> -RPAP3 iso1 <sub>1-665</sub>	This paper	N/A
pQLink RUVBL1 <sub>1-456</sub> , RUVBL2 <sub>1-463</sub> , H <sub>7</sub> -RPAP3 iso1 <sub>125-665</sub>	This paper	N/A
pQLink RUVBL1 <sub>1-456</sub> , RUVBL2 <sub>1-463</sub> , H <sub>7</sub> -RPAP3 iso1 <sub>1-540</sub>	This paper	N/A
pQLink RUVBL1 <sub>1-456</sub> , H <sub>7</sub> -RPAP3 iso1 <sub>1-665</sub>	This paper	N/A
pQLink RUVBL2 <sub>1-463</sub> , H <sub>7</sub> -RPAP3 iso1 <sub>1-665</sub>	This paper	N/A
pQLink RUVBL1 <sub>1-456</sub> , H <sub>7</sub> -RPAP3 iso1 <sub>540-665</sub>	This paper	N/A
pQLink RUVBL2 <sub>1-463</sub> , H <sub>7</sub> -RPAP3 iso1 <sub>540-665</sub>	This paper	N/A
pQLink RUVBL1 <sub>Δ126-234</sub> , RUVBL2 <sub>Δ133-238</sub> , H <sub>7</sub> -RPAP3 iso1 <sub>1-665</sub>	This paper	N/A
pQLink RUVBL1 <sub>1-456</sub> , H <sub>7</sub> -RPAP3 iso1 <sub>385-665</sub>	This paper	N/A
pQLink RUVBL2 <sub>1-463</sub> , H <sub>7</sub> -RPAP3 iso1 <sub>385-665</sub>	This paper	N/A
pQLink RUVBL1 <sub>1-456</sub> , H <sub>7</sub> -RPAP3 iso1 <sub>442-665</sub>	This paper	N/A
pQLink RUVBL2 <sub>1-463</sub> , H <sub>7</sub> -RPAP3 iso1 <sub>442-665</sub>	This paper	N/A
pQLink RUVBL1 <sub>1-456</sub> , H <sub>7</sub> -RPAP3 iso1 <sub>385-665/Δ492-500</sub>	This paper	N/A
pQLink RUVBL2 <sub>1-463</sub> , H <sub>7</sub> -RPAP3 iso1 <sub>385-665/Δ492-500</sub>	This paper	N/A
pQLink RUVBL1 <sub>1-456</sub> , H <sub>7</sub> -RPAP3 iso1 <sub>442-665/Δ492-500</sub>	This paper	N/A
pQLink RUVBL2 <sub>1-463</sub> , H <sub>7</sub> -TEV-RPAP3 iso1 <sub>442-665/ Δ492-500</sub>	This paper	N/A

(Continued on next page)

**Continued**

REAGENT or RESOURCE	SOURCE	IDENTIFIER
pQLink H <sub>7</sub> -RPAP3 iso1 <sub>1-665</sub> , PIH1D1 <sub>1-290</sub>	This paper	N/A
pQLink H <sub>7</sub> -RPAP3 iso2 <sub>1-631</sub> , PIH1D1 <sub>1-290</sub>	This paper	N/A
pQLink H <sub>7</sub> -RPAP3 iso1 <sub>385-665</sub> , PIH1D1 <sub>1-290</sub>	This paper	N/A
pQLink H <sub>7</sub> -RPAP3 iso2 <sub>385-631</sub> , PIH1D1 <sub>1-290</sub>	This paper	N/A
pQLink H <sub>7</sub> -RPAP3 iso1 <sub>1-665</sub> , PIH1D1 <sub>1-280</sub>	This paper	N/A
pQLink H <sub>7</sub> -RPAP3 iso1 <sub>540-665</sub> , PIH1D1 <sub>1-290</sub>	This paper	N/A
pQLink H <sub>7</sub> -RPAP3 iso1 <sub>1-540</sub> , PIH1D1 <sub>1-290</sub>	This paper	N/A
p11 H <sub>6</sub> -RUVBL1 <sub>1-456</sub> WB	This paper	N/A
p11 H <sub>6</sub> -RUVBL2 <sub>1-463</sub> WB	This paper	N/A
pCOLADuet-1 RUVBL1 <sub>1-456</sub> -H <sub>6</sub> , eXact tag-RUVBL2 <sub>1-463</sub>	This paper	N/A
pETSUMO2 H <sub>12</sub> -SUMO-RPAP3 iso1 <sub>540-665</sub>	This paper	N/A
pQLink RUVBL1 <sub>1-456</sub> , H <sub>7</sub> -RPAP3 iso2 <sub>1-631</sub>	This paper	N/A
pQLink RUVBL2 <sub>1-463</sub> , H <sub>7</sub> -RPAP3 iso1 <sub>1-631</sub>	This paper	N/A
pQLink RUVBL1 <sub>1-456</sub> , H <sub>7</sub> -RPAP3 iso2 <sub>385-631</sub>	This paper	N/A
pQLink RUVBL2 <sub>1-463</sub> , H <sub>7</sub> -RPAP3 iso2 <sub>385-631</sub>	This paper	N/A
pCOLADuet-1 RPAP3 iso2 <sub>1-631</sub> , H <sub>6</sub> -PIH1D1 <sub>1-290</sub>	This paper	N/A
pQLink RPAP3 iso1 <sub>385-665</sub> -FLAG, H <sub>7</sub> -PIH1D1 <sub>1-290</sub>	This paper	N/A
pQLink RPAP3 iso2 <sub>385-631</sub> -FLAG, H <sub>7</sub> -PIH1D1 <sub>1-290</sub>	This paper	N/A
pQLink RPAP3 iso1 <sub>540-665</sub> -FLAG, H <sub>7</sub> -PIH1D1 <sub>1-290</sub>	This paper	N/A
pQLink RPAP3 iso1 <sub>1-540</sub> , H <sub>7</sub> -PIH1D1 <sub>1-290</sub>	This paper	N/A
pOBD2	A gift from Stanley Fields Lab, University of Washington	<a href="http://www.fieldslab.org/vector-pobd2.html">http://www.fieldslab.org/vector-pobd2.html</a>
pOAD	A gift from Stanley Fields Lab, University of Washington	<a href="http://www.fieldslab.org/vector-poad.html">http://www.fieldslab.org/vector-poad.html</a>
pOBD2 RPAP3 <sub>1-665</sub>	This paper	N/A
pOBD2 RPAP3 <sub>1-565</sub>	This paper	N/A
pOBD2 RPAP3 <sub>1-465</sub>	This paper	N/A
pOBD2 RPAP3 <sub>1-415</sub>	This paper	N/A
pOBD2 RPAP3 <sub>1-390</sub>	This paper	N/A
pOAD PIH1D1 <sub>1-290</sub>	This paper	N/A
pOAD PIH1D1 <sub>1-280</sub>	This paper	N/A
pcDNA5 FLAG-PIH1D1	This paper	N/A
pcDNA5 RPAP3 iso1-3xFLAG	This paper	N/A
pcDNA5 RPAP3 iso1-3xFLAG	This paper	N/A
pcDNA5 FLAG-RPAP3 iso1	This paper	N/A
pcDNA5 RPAP3 iso1-3xFLAG	This paper	N/A
pcDNA5 RPAP3 iso1-3xFLAG	This paper	N/A
pcDNA5 FLAG-RPAP3 iso1	This paper	N/A

**Software and algorithms**

ATSAS 2.7.2 package	(Franke et al., 2017)	<a href="http://www.embl-hamburg.de/biosaxs/download.html">www.embl-hamburg.de/biosaxs/download.html</a> ; RRID: SCR_015648
ASTRA 7.1.2	Wyatt Technology	<a href="https://www.wyatt.com/products/software/astra.html">https://www.wyatt.com/products/software/astra.html</a> ; RRID: SCR_016255

(Continued on next page)

**Continued**

REAGENT or RESOURCE	SOURCE	IDENTIFIER
UCSF ChimeraX 1.1	(Pettersen et al., 2021)	<a href="https://www.cgl.ucsf.edu/chimerax/download.html">https://www.cgl.ucsf.edu/chimerax/download.html</a> ; RRID: SCR_015872
Clustal Omega	(Madeira et al., 2019)	<a href="https://www.ebi.ac.uk/Tools/msa/clustalo/">https://www.ebi.ac.uk/Tools/msa/clustalo/</a> ; RRID: SCR_001591
Weblogo 3	(Crooks et al., 2004)	<a href="http://weblogo.threeplusone.com/">http://weblogo.threeplusone.com/</a> ; RRID: SCR_010236
PSIPRED and DISOPRED	(Buchan and Jones, 2019)	<a href="http://bioinf.cs.ucl.ac.uk/psipred/">http://bioinf.cs.ucl.ac.uk/psipred/</a> ; RRID: SCR_010246
MARCOIL	(Delorenzi and Speed, 2002)	<a href="https://bcf.isb-sib.ch/webmarcoil/webmarcoilINFO1.html">https://bcf.isb-sib.ch/webmarcoil/webmarcoilINFO1.html</a>
PONDR	Molecular Kinetics Inc.	<a href="http://www.pondr.com/">http://www.pondr.com/</a>
PDBSum	(Laskowski et al., 2018)	<a href="http://www.ebi.ac.uk/thornton-srv/databases/cgi-bin/pdbsum/GetPage.pl?pdbcode=index.html">http://www.ebi.ac.uk/thornton-srv/databases/cgi-bin/pdbsum/GetPage.pl?pdbcode=index.html</a> ; RRID: SCR_006511
Sedfit	(Schuck, 2000)	<a href="http://www.analyticalultracentrifugation.com/download.htm">http://www.analyticalultracentrifugation.com/download.htm</a> ; RRID: SCR_018365
Origin 7.0	OriginLab Corporation	<a href="http://www.originlab.com">www.originlab.com</a>
EMAN: Boxer	(Ludtke et al., 1999)	<a href="https://blake.bcm.edu/emanwiki/EMAN1">https://blake.bcm.edu/emanwiki/EMAN1</a> ; RRID: SCR_016867
XCalibur 4.1.31.9	Thermo Fisher Scientific	<a href="https://www.thermofisher.com/order/catalog/product/OPTON-30965#/OPTON-30965">https://www.thermofisher.com/order/catalog/product/OPTON-30965#/OPTON-30965</a> ; RRID: SCR_014593
Proteome Discoverer 2.2	Thermo Fisher Scientific	<a href="https://www.thermofisher.com/order/catalog/product/OPTON-30945#/OPTON-30945">https://www.thermofisher.com/order/catalog/product/OPTON-30945#/OPTON-30945</a> ; RRID: SCR_014477
xiVIEW	(Graham et al., 2019)	<a href="https://xiview.org/xiNET_website/index.php">https://xiview.org/xiNET_website/index.php</a>
SEQUEST	(Eng et al., 1994)	<a href="http://fields.scripps.edu/yates/wp/?page_id=17">http://fields.scripps.edu/yates/wp/?page_id=17</a>
CRAPome	(Mellacheruvu et al., 2013)	<a href="https://reprint-apms.org/?q=reprint-home">https://reprint-apms.org/?q=reprint-home</a>
DAVID	(Huang et al., 2009b)	<a href="https://david.ncifcrf.gov/">https://david.ncifcrf.gov/</a> ; RRID: SCR_001881
InteractiVenn	(Heberle et al., 2015)	<a href="http://www.interactivenn.net/">http://www.interactivenn.net/</a>
<b>Other</b>		
Ni Sepharose 6 Fast Flow	GE Healthcare Life Sciences	Cat#17531802
Mono Q 5/50 GL	GE Healthcare Life Sciences	Cat#17516601
HiLoad Superdex 200 16/600 pg	GE Healthcare Life Sciences	Cat#28989335
Superdex 200 Increase 10/300 GL	GE Healthcare Life Sciences	Cat#28990944
Superdex 200 HR10/300 GL	GE Healthcare Life Sciences	Cat#54801-U
HisPur cobalt resin	Thermo Fisher Scientific	Cat#89965
Anti-FLAG M2 magnetic beads	Millipore	Cat#M8823; RRID: AB_2637089
MiniDAWN TREOS II	Wyatt Technology	Part#WTS2
Optilab T-rEX	Wyatt Technology	Part#WTREX
EnSpire 2300 multilabel reader	Perkin-Elmer	<a href="http://www.perkinelmer.com/product/enspire-base-unit-2300-0000">http://www.perkinelmer.com/product/enspire-base-unit-2300-0000</a>
J-810 spectropolarimeter	Jasco	Part#0302-0407A
ProteomeLab XL-A analytical ultracentrifuge	Beckman Coulter	RRID: SCR_019567
Fluorolog-3 spectrophotometer	HORIBA	Model#FL3-22; RRID: SCR_020061
Pilatus 300K detector	Dectris, SAXS1 – Brazilian Synchrotron Light Laboratory	<a href="https://www.lnls.cnpem.br/saxs1-5/">https://www.lnls.cnpem.br/saxs1-5/</a>
Mass photometry instrumentation	(Young et al., 2018)	N/A

(Continued on next page)

**Continued**

REAGENT or RESOURCE	SOURCE	IDENTIFIER
High mass Q-TOF-type instrument adapted for a QSTAR CL platform	(Chernushevich and Thomson, 2004; Sobott et al., 2002)	N/A
2010F TEM	JEOL	N/A
Super COOLSCAN 9000 ED	Nikon	<a href="https://www.nikonusa.com/en/nikon-products/product-archive/film-scanners/super-coolscan-9000-ed.html">https://www.nikonusa.com/en/nikon-products/product-archive/film-scanners/super-coolscan-9000-ed.html</a>
SO-163 film	Kodak	N/A
Tecnai T12	FEI	N/A
4k CCD camera	Gatan	N/A
C-18 TopTip	Glygen	<a href="http://www.glysci.com/products/TopTip.html">http://www.glysci.com/products/TopTip.html</a>
SpeedVac	Savant	Model#SVC-100H
Luna SCX (50 x 2 mm, 5 $\mu$ m, 100 Å)	Phenomenex	Part#00B-4398-B0
EASY-nLC 1000	Thermo Fisher Scientific	Cat#LC120; RRID: SCR_014993
Reposil-Pur 120 (75 $\mu$ m I.D., 25 cm length, 3 $\mu$ m, 120 Å)	Dr. Maisch	C-18-AQ
1100 HPLC	Agilent	RRID: SCR_019348
Orbitrap Fusion Tribrid	Thermo Fisher Scientific	Cat#IQLAAEGAAPFADBMBXC; RRID: SCR_020559
Nanospray Flex NG	Thermo Fisher Scientific	Cat#ES072
Nano C18 column (10 cm x 75 $\mu$ m ID, 3 $\mu$ m, 100 Å)	Laboratory of Mohan Babu, University of Regina	N/A
Orbitrap Elite	Thermo Fisher Scientific	RRID: SCR_020548
Äkta Pure	GE Healthcare Life Sciences	Part#29018225; RRID: SCR_019958
Äkta FPLC	Amersham Biosciences	N/A

## RESOURCE AVAILABILITY

### Lead contact

Further information and requests for resources and reagents should be directed to and will be fulfilled by Walid A. Houry ([walid.houry@utoronto.ca](mailto:walid.houry@utoronto.ca)).

### Materials availability

Unique/stable reagents generated in this study will be made available upon request as long as in stock; the University of Toronto may require a completed Materials Transfer Agreement.

### Data and code availability

No novel code was generated during this work. Raw data are available from the authors upon request. Any additional information required to reanalyze the data reported in this paper is available from the lead contact upon request.

## EXPERIMENTAL MODEL AND SUBJECT DETAILS

### *Escherichia coli* cell cultures

*E. coli* LOBSTR BI21(DE3) strain, carrying mutations in *arnA* and *slyD* genes (Andersen et al., 2013) and transformed with the pRIL (Cam<sup>R</sup>) vector (Agilent), was grown at 37°C in Lysogenic Broth (LB) supplemented with 34  $\mu$ g/mL of chloramphenicol (LB-Clo). LOBSTR BI21(DE3) pRIL cells transformed with Kan<sup>R</sup> or Amp<sup>R</sup>-containing plasmids were grown in LB-Clo containing 35  $\mu$ g/mL of kanamycin or 100  $\mu$ g/mL of ampicillin, respectively.

### *Saccharomyces cerevisiae* cell cultures

*S. cerevisiae* cells PJ69-4 $\alpha$  strain, genotype MAT $\alpha$  *trp1-901 leu2-3,112 ura3-52 his3-200 gal4 $\Delta$  gal80 $\Delta$  LYS2::GAL1-HIS3 GAL2-ADE2 met2::GAL7-lacZ* (James et al., 1996), were cultured in YPD medium at 30°C. When transformed with pOBD2 and pOAD vectors, yeast cells were grown in synthetic defined (SD) medium lacking leucine and tryptophan at 30°C.

### Mammalian cell cultures

HEK293T cells were grown at 37°C with 5% CO<sub>2</sub> in Dulbecco's Modified Eagle Medium (DMEM) supplemented with 10% fetal bovine serum (FBS) and 100 U/mL penicillin-streptomycin. RPE-1, RPE-1 *RPAP3* KO and RPE-1 *PIH1D1* KO cells were cultured at 37°C with 5% CO<sub>2</sub> in DMEM/Nutrient Mixture F-12 containing 10% FBS and 100 U/mL penicillin-streptomycin.

### METHOD DETAILS

#### Protein expression and purification

All recombinant proteins were expressed using the *E. coli* LOBSTR strain (Andersen et al., 2013) previously transformed with pACYC RIL (pRIL) (Agilent Technologies), and plasmids used in this work are described in Table S5. Buffer solutions used throughout this work are given in Table S6. Briefly, bacterial cells transformed with the plasmid of interest were initially grown overnight in LB medium at 37°C. Next day, cells were transferred to fresh LB medium (1-5% culture, v/v) and incubated at 37°C in an orbital shaker incubator (200 rpm) until OD<sub>600</sub> = 0.6-0.8. Subsequently, temperature was decreased to 18°C and IPTG was added to 1 mM final concentration to induce protein expression and, after 15 hours, cells were harvested by centrifugation at 3,000 x g for 10 minutes. Cellular extracts were prepared by resuspending cells in the buffer A (15 mL/liter of culture), followed by sonication on ice. Lysates were spun down at 12,000 x g for 30 min at 4°C for cellular debris removal, and supernatants were further purified by immobilized metal affinity chromatography (IMAC), since all recombinant proteins produced were fused to a His-tag.

IMAC was performed as the first purification step for all proteins using Ni Sepharose 6 Fast Flow beads (GE Healthcare Life Sciences) packed into an Econo-column (Bio-Rad). Buffer A was used for washing, whereas the elution step was done with buffer B. Proteins expressed from pQLinkH (Scheich et al., 2007) or p11 (Toronto SGC) had their His-tag cleaved off by tobacco etch virus (TEV), while those expressed from the pET-SUMO plasmid (Invitrogen) had their His-SUMO tag removed by incubation with the Ulp1 protease (Lee et al., 2008). H<sub>6</sub>-PIH1D1-H<sub>6</sub> expressed from pRM18 vector (Machado-Pinilla et al., 2012) was kept tagged.

For wild type RUVBL1, RUVBL2 and their mutants, the second and final step of purification consisted of ion exchange chromatography using a Mono Q 5/50 GL column (GE Healthcare Life Sciences) connected to an Äkta Pure system (GE Healthcare Life Sciences). Proteins purified using IMAC were dialyzed against buffer C for 4 hours and submitted to ion-exchange chromatography. The elution was done by a linear gradient from 0% to 100% of buffer D. RUVBL proteins were dialyzed and stored in buffer E.

For structural characterization of RPAP3, PIH1D1 and related constructs were submitted to size exclusion chromatography using a HiLoad Superdex 200 16/600 prep grade (GE Healthcare Life Sciences) equilibrated with buffer F and connected to an Äkta Pure system. For ATPase assays, proteins were dialyzed against buffer G and submitted to an extra purification step of ion exchange in a Mono Q 5/50 GL column (GE Healthcare Life Sciences). Elution was carried out using a linear gradient of buffer H. Samples were dialyzed in buffer E prior to performing the ATPase assays.

#### In vitro pull-down experiments

All plasmids used for pull-downs throughout this work are described in Table S5. For recombinant protein expression or co-expression, *E. coli* LOBSTR pRIL cells containing the plasmid of interest were grown in 50 mL LB medium at 37°C in an orbital shaker incubator (200 rpm) until OD<sub>600</sub> = 0.6-0.8. Subsequently, the temperature was changed to 18°C and protein expression was induced by 1 mM IPTG final concentration. After 15 hrs, cells were harvested by centrifugation (10 min, 3,000 x g, 4°C), frozen and kept at -20°C until use. Bacterial cell lysis was done by sonication after resuspension of the frozen pellets in 2 mL of buffer I. Cellular debris was separated from the soluble fraction of the lysate by centrifugation at 10,000 x g for 10 min at 4°C. Using 2 mL Econo-columns (Bio-Rad), 100 µL of 50% slurry HisPur Co<sup>2+</sup> metal affinity beads (Thermo Fisher Scientific) were pipetted in and then washed with 1 mL of buffer I.

The soluble fraction of the lysates was loaded into columns and flowed-through the beads by gravity. Lysates from co-expression were loaded directly into the columns, whereas lysates coming from individually expressed proteins were mixed and incubated for 30 min on ice prior to loading. After loading, beads were washed 8 times with 1 mL of buffer I in order to remove contaminants and unbound proteins. The elution step was performed by adding 100 µL of buffer J. In addition to the eluate, input, flow-through and last wash fractions were collected and analyzed by SDS-PAGE and Western blot. Polyclonal anti-RUVBL1 (Abcam and Invitrogen), anti-RUVBL2 (Abcam and Invitrogen), anti-RPAP3 (Invitrogen) antibodies, and monoclonal anti-PIH1D1 (Santa Cruz) and anti-His tag (Millipore and Bio-Rad) antibodies, were used for immunodetection of proteins.

The dissociation of RUVBL proteins from RPAP3, PIH1D1 and RPAP3-PIH1D1 upon nucleotide binding and/or hydrolysis (Figures 7E-7H) was performed following the same procedures described for pull-down experiments, except for the elution step. After the washes, instead of adding elution buffer containing imidazole, 100 µL of buffer I containing either 1 mM ATP or ADP were added to beads containing immobilized complexes. Samples were incubated at 37°C for 30 min and supernatants containing released proteins were collected. Detection of proteins was done by Western blot using the antibodies described above. All *in vitro* pull-down experiments were performed at least in triplicates.

#### In vivo pull-down experiments

Plasmids used for *in vivo* pull-downs are described in Table S5. Retinal pigment epithelial (RPE-1) cells were transfected with plasmids, and, after 24 hours, cells were washed with PBS. Cell lysis was done in buffer N supplemented with protease inhibitor cocktail

(Roche), followed by immunoprecipitation with anti-FLAG M2 magnetic beads (Millipore) according to the manufacturer's protocol. Samples were resolved using SDS-PAGE and visualized by western Blot using PVDF membrane. Antibodies are described above in addition to the monoclonal anti-FLAG M2 antibody (Millipore).

### Yeast two-hybrid assay

For the yeast two-hybrid assays, the *S. cerevisiae* PJ69-4 $\alpha$  strain (MAT $\alpha$  *trp1-901 leu2-3,112 ura3-52 his3-200 gal4 $\Delta$  gal80 $\Delta$  LYS2::GAL1-HIS3 GAL2-ADE2 met2::GAL7-lacZ*) (James et al., 1996), pOBD2 (*TRP1* plasmid) and pOAD (*LEU2* plasmid) plasmids were used (Table S5). Yeast cells containing both pOBD2 and pOAD-derived plasmids were grown overnight at 30 °C in liquid synthetic defined (SD) medium lacking leucine (-L) and tryptophan (-W). Next day, cells were diluted to OD<sub>600</sub> = 0.1 in SD -L -W -H medium and serial dilutions (from 1 to 1000-fold dilution) were prepared. 5  $\mu$ L of the dilutions were spotted on SD -L -W and SD -L -W +100 mM 3-amino-1,2,4-triazole (3-AT, Sigma-Aldrich) plates, which were incubated for 56-72 hrs at 30 °C. These experiments were performed in triplicates.

### Analytical size exclusion chromatography (SEC)

SEC experiments were performed at 4 °C using a Superdex 200 HR 10/30 column (GE Healthcare Life Sciences) connected to an Äkta FPLC system (Amersham Biosciences) and equilibrated with buffer E. Proteins were prepared at the desired monomer concentrations, with ATP added, when required, at 1.5 mM final concentration. In general, 200  $\mu$ L of samples were injected onto the column and their elution profile monitored by absorbance at 280 nm. Fractions of 1 mL were collected, separated on 12% SDS-PAGE gels, and visualized by silver-staining. Protein molecular mass standards consisting of thyroglobulin (669 kDa), apoferritin (443 kDa),  $\beta$ -amylase (200 kDa), alcohol dehydrogenase (150 kDa), bovine serum albumin (66 kDa), carbonic anhydrase (29 kDa), and cytochrome C (12.4 kDa) (GE Healthcare Life Sciences) were used for molecular mass estimations.

### Size exclusion chromatography coupled to multi-angle light scattering (SEC-MALS)

SEC-MALS experiments were performed using a Superdex 200 Increase 10/300 column (GE Healthcare Life Sciences) connected to an Äkta Pure system (GE Healthcare Life Sciences) in line with a miniDAWN TREOS II light scattering detector (Wyatt Technology) and an Optilab T-REX refractive index detector (Wyatt Technology). In all SEC-MALS experiments, 100  $\mu$ L of protein solution was injected into the size exclusion column equilibrated with buffer I at a 0.5 mL/min flow rate and at 4 °C. Data analysis was done using the ASTRA 7.1.2 software (Wyatt Technology).

### ATPase assays

ATPase activity measurements were performed using the ATP/NADH coupled ATPase assay (Norby, 1988). The reactions consisted of 3 mM phosphoenolpyruvate, 0.2 mM NADH, 40 U/mL pyruvate kinase, 58 U/mL lactate dehydrogenase in the buffer K. Proteins of interest and ATP were added to a final volume of 150  $\mu$ L and all the reaction components were incubated for 10 min at 37 °C prior to ATP addition. Samples were placed in a 96-well flat-bottom plate (Greiner Bio-One) and measurements of absorbance at 340 nm were done at 37 °C for 1 hour in an EnSpire 2300 Multilabel Reader (Perkin Elmer). Samples containing no proteins were used as controls for background NADH decomposition. ATP hydrolysis rates were calculated from the slope of the change in absorbance at 340 nm over time. All experiments were done at least in triplicate and standard deviations are presented.

End-point measurements in the presence of RPAP3, RPAP3-PIH1D1 and RPAP3 C-domain were performed using 5 mM ATP and RUVBL1/2 at 2  $\mu$ M hexamers; complexes were formed by mixing equimolar concentrations of RUVBL1 and RUVBL2, followed by incubation for at least 1 hour at 4 °C. Controls containing only RPAP3, RPAP3 C-domain and RPAP3-PIH1D1 were subtracted from their respective samples containing RUVBL1/2.

To obtain kinetic parameters of RUVBL1, RUVBL2, RUVBL1/2 ATPase activities, ATPase assays were performed using protein concentration of 10  $\mu$ M (monomers) and ATP concentrations varying from 0.1 mM to 7 mM. Michaelis-Menten constant ( $K_M$ ), maximum velocity ( $V_{max}$ ) and turnover number ( $k_{cat}$ ) were calculated by fitting experimental initial velocity values of the proteins at different ATP concentrations using the equation:

$$V = \frac{V_{max}[S]}{K_M + [S]}$$

where  $V$  is the initial velocity,  $V_{max}$  is the maximum velocity,  $K_M$  is the Michaelis-Menten constant and  $[S]$  is the molar concentration of the substrate.

### Bioinformatics

Global sequence alignment was done using Clustal Omega (Madeira et al., 2019). Sequence logos were constructed using the Weblogo 3 program (Crooks et al., 2004). Protein secondary structure and disorder were predicted by PSIPRED and DISOPRED servers (Buchan and Jones, 2019). The probability of coiled-coil formation was predicted by MARCOIL (Delorenzi and Speed, 2002) and hydropathy index was calculated using PONDR tool. Protein structure diagrams were generated using the PDBsum server (Laskowski et al., 2018).

### Spectroscopy experiments

Circular dichroism spectra were collected on a J-810 spectropolarimeter (Jasco) using full-length R2TP proteins at 0.10 mg/mL – 0.4 mg/mL in the buffer I. Data were collected from 198 to 260 nm, 0.5 nm data pitch, at scanning speed of 100 nm/min and response time of 0.5 sec. For RPAP3 ND, samples were used at 0.07 and 0.14 mg/mL and data were collected from 196 nm to 260 nm using the same spectropolarimeter setup. Thermal unfolding of RPAP3 ND was performed from 20°C to 80°C using 1°C/min heating rate, with acquisition of spectra every 20°C. All experiments were done using a 1 mm quartz cuvette. Protein spectra were subtracted from the blank and converted to mean residue ellipticity,  $[\theta]$ , using the equation:

$$[\theta] = \frac{\theta \times M \times 100}{n \times c \times l}$$

Where,  $\theta$  is the circular dichroism signal in millidegrees,  $M$  is the molecular mass in kDa,  $n$  is the number of amino acid residues,  $c$  is the concentration in mg/mL and  $l$  is the pathlength in cm.

RPAP3 ND fluorescence emission spectra were acquired using a Fluorolog spectrofluorometer (HORIBA) with samples at 5  $\mu$ M, excitation wavelength at 280 nm and emission fluorescence collected from 300 nm to 450 nm, using 1 nm data pitch. Spectra from samples were subtracted from their respective blanks.

### Analytical ultracentrifugation

Sedimentation velocity (SV-AUC) experiments were done with a ProteomeLab XL-A analytical ultracentrifuge (Beckman) using the An60-Ti rotor. RPAP3 samples were prepared at 0.8 mg/mL in buffer I and data from 200 scans were collected at 20 °C, 25,000 rpm, using absorbance at 280 nm. Data analysis was performed using the Sedfit software (Schuck, 2000) with RPAP3 V of 0.73591 cm<sup>3</sup>/g, and buffer density and viscosity of 1.0194 g/cm<sup>3</sup> and 0.010556 P, respectively.

### Small angle X-ray scattering (SAXS)

SAXS experiments were carried out at the SAXS1 beamline located at the Brazilian Synchrotron Light Laboratory (LNLS – CNPEM, Campinas, SP, Brazil). Scattering profiles were recorded using a 1.544 Å wavelength electron beam and a Pilatus 300K detector (Dectris), with a sample-to-detector distance of 898.39 mm, corresponding to the range 0.013 <  $q$  < 0.49. RPAP3 and RPAP3-PIH1D1 samples were prepared in buffer L. RPAP3 samples were used at 0.6 mg/mL, 1 mg/mL, and 1.4 mg/mL; samples of RPAP3-PIH1D1 complex were used at 0.8 mg/mL, 1.8 mg/mL, and 2.6 mg/mL; RUVBL2 and RUVBL1/2 samples were prepared at 0.85 mg/mL (16.6  $\mu$ M protomer for RUVBL2 and 16.8  $\mu$ M protomer for RUVBL1/2) and 1.7 mg/mL (33.2  $\mu$ M and 33.5  $\mu$ M protomer for RUVBL2 and RUVBL1/2, respectively) in buffer E. To obtain protein scattering profiles, scattering curves of buffers were subtracted from their respective samples. All samples were collected at various time frames (10 sec to 300 sec) in order to inspect for X-ray damage. Standard deviations are shown for Guinier approximation analyses.

The ATSAS 2.7.2 package (Franke et al., 2017) was used for SAXS data processing. Scattering curves were compared and merged into a single curve by PRIMUS and DATMERGE programs, respectively. The generation of pair distance distribution functions,  $P(r)$ , was done using the GNOM software (Svergun, 1992). *Ab initio* dummy atoms (DA) models were generated using a simulated-annealing methodology implemented in DAMMIN and DAMMIF software (Franke and Svergun, 2009; Svergun, 1999). Using DAMMIF, twenty models were generated for each protein and P1 symmetry axis was imposed for RPAP3 and RPAP3-PIH1D1. Alignment, averaging and selection of the most probable DA models were done by the DAMAVER software package (Volkov and Svergun, 2003). DA model refinement was done by DAMMIN.

Ensemble optimization method was performed using the EOM 2.0 package (Tria et al., 2015). Crystal structures of RPAP3 TPR1 (Pal et al., 2014) and TPR2 (Henri et al., 2018) domains and C-domain (Maurizy et al., 2018) were used in this approach. The high-resolution structures were connected by flexible linkers using C $\alpha$  distribution compatible to those from natively disordered structures. Ten thousand RPAP3 conformers were generated, and their respective size and dimension computed by the RANCH (Random Chains) program. The best ensemble of conformers describing the experimental RPAP3 scattering profile was selected by the genetic algorithm implemented in the GAJOE (Genetic Algorithm Judging Optimization of Ensembles) program. This selection was done 10 times and the curves represent the average of the results.

Rigid-body modeling simulations of complexes were done with the CORAL (Complexes with Random Loops) program (Petoukhov et al., 2012). In the RUVBLs simulations, the crystal structures of RUVBL1 (Matias et al., 2006) and RUVBL2 (Silva et al., 2018) were used. The regions of RUVBL1 comprising amino acid residues 1–42, 122–132, 202–239 and 450–456 were filled with dummy residues in order to obtain the full-length structure and to account for DII<sub>ext</sub> flexibility. Similarly, amino acid residues from 1–48, 127–137, 212–243 and 457–463 were modeled by dummy residues in the RUVBL2 rigid-body models. RUVBL1 and RUVBL2 were positioned in the RUVBL1/2 heterodimer based on the crystal structure of RUVBL1/2 lacking their DII (Gorynia et al., 2011). P6 symmetry axis was applied for RUVBL2, whereas P32 symmetry axis was used for RUVBL1/2. Generation of rigid-body models was done 5 times for each protein complex and structures displaying the best fit to the experimental SAXS curves are shown. Centering of structures to the origin and alignment of PDB chains to coordinate axis were done by the ALPRAXIN software (Kozin and Svergun, 2001).

RPAP3-PIH1D1 rigid-body modelling was performed using a combination of CORAL and DAMCLUST (Petoukhov et al., 2012) programs. Fifty RPAP3-PIH1D1 models were generated using RPAP3 crystal structures as described for EOM, and PIH1D1 PIH1 (Hor-ejsi et al., 2014) and CS (Henri et al., 2018) domains structures applying P1 symmetry axis. DAMCLUST was employed to cluster all 50 RPAP3-PIH1D1 models based on their normalized spatial discrepancy.

### Mant-ADP fluorescence assays

Experiments with the fluorescent ADP analogue mant-ADP (Jena Bioscience) were performed using a Fluorolog spectrofluorometer (HORIBA). Samples were prepared in buffer Q as follows: (1) RUVBL1 = 1  $\mu$ M as hexamers, (2) RUVBL2 = 1  $\mu$ M as hexamers, (3) RUVBL1/2 = 1  $\mu$ M as heterohexamers, (4) R2TP = 1  $\mu$ M RUVBL1/2 as heterohexamers + 3  $\mu$ M RPAP3-PIH1D1 as heterodimers, (5) R2T = 1  $\mu$ M RUVBL1/2 as heterohexamers + 3  $\mu$ M RPAP3 as monomers, and (6) R2P = 1  $\mu$ M RUVBL1/2 as hexamers + 3  $\mu$ M PIH1D1 as monomers. Samples were incubated for 15 min on ice followed by 30 min with 6  $\mu$ M mant-ADP. Titration of ATP $\gamma$ S and ADP were performed by adding increasing concentrations of the non-fluorescent nucleotides (0 to 60  $\mu$ M) to samples followed by incubation for at least 60 min on ice. Mant-ADP was excited at 355 nm (2 nm slit) and its fluorescence emission was collected from 400 nm to 600 nm (5 nm slit), using data pitch of 1 nm. Blank and control samples were submitted to the same procedures. Fluorescence spectra were analyzed by means of spectral center of mass  $\langle\lambda\rangle$ , using the equation:

$$\langle\lambda\rangle = \frac{\sum F_i \times \lambda_i}{\sum F_i}$$

Where,  $F_i$  is the fluorescence intensity at each wavelength and  $\lambda_i$  is the wavelength.

Calculation of apparent dissociation constants ( $K_d^{app}$ ) was done by fitting the normalized difference between initial and final  $\langle\lambda\rangle$  ( $\Delta\langle\lambda\rangle$ ) as function of ADP or ATP $\gamma$ S concentration to a OneSiteBind function using Origin 7 software.

### Mass photometry

Mass photometry measurements were performed as described in reference (Young et al., 2018). Briefly, the output of a 520 nm laser diode (Lasertack) was collimated and sent through a pair of acousto-optic deflectors (AODs, AA Optoelectronic DTSXY-400). A 4f telecentric lens system imaged the deflection by the AODs into the back focal plane of the microscope objective (Olympus UApo N, 100x, 1.49 NA). The objective collected light reflected at the interface between a glass coverslip and some of the light scattered by the sample, with efficient separation of illumination and detection achieved through the combination of a polarizing beam splitter and quarter-wave plate (Thorlabs). The same telecentric lens system imaged the back focal plane of the objective onto a partial reflector made from a thin layer of silver of 2.5 mm diameter deposited onto a window, which selectively attenuates the reflected light compared to light from point scatters at the surface. A final lens imaged the sample onto a CMOS camera (Ximea, MC023MG-SY) with 277.8x magnification, resulting in a final pixel size of 21.1 nm/pixel. Borosilicate microscope coverslips (24x50 mm<sup>2</sup>, #1.5H from Thorlabs, and 24x24 mm<sup>2</sup>, No. 1.5 from VWR) used in these experiments were cleaned by ultra-sonication for 10 min in ultrapure water, followed by isopropanol and again ultrapure water, before being dried under a clean stream of nitrogen. Cleaned coverslips were assembled into flow chambers (Yildiz et al., 2003). After introduction of  $\sim$ 15  $\mu$ L of sample to the flow chamber, images of a 3.5 x 12.2  $\mu$ m<sup>2</sup> region of the glass coverslip surface as proteins bind non-specifically from solution were acquired at 1000 frames/s. The illuminating power density was 800 kW cm<sup>-2</sup>. Prior to saving each movie file, areas of 4x4 pixels were binned for an effective pixel size of 84.4 nm/pixel, and frames were averaged 5-fold in time. Ratiometric frames were calculated, and mass distributions extracted as described previously (Cole et al., 2017; Young et al., 2018).

The contrast-to-mass conversion of the instrument was calibrated using the molecular weight standard proteins alcohol dehydrogenase and  $\beta$ -amylase, purchased from Sigma-Aldrich. Each protein was measured twice, and the measured contrasts of the dimer and tetramer peaks of each taken for calibration.

For the titration experiments, solutions of RUVBL1/2 at 0.2  $\mu$ M (heterohexamer concentration) were incubated on ice for  $\sim$ 30 mins together with the other component (RPAP3 iso1-PIH1D1, RPAP3 iso1, or PIH1D1) in concentrations of 0, 0.2, 0.4, 0.8 and 1.6  $\mu$ M. Solutions were diluted a further 10-fold immediately ( $<$ 10 s) before adding to the flow chamber, to ensure sufficient separation in the images between the diffraction-limited features of single protein binding events. Two measurements were performed for each condition, and the data reported here are the combined results of the two. To characterize each component individually, the same procedure was carried for RPAP3-PIH1D1, RPAP3 and PIH1D1 at an incubation concentration of 0.4  $\mu$ M. The distribution shown for RUVBL1/2 was taken from 6 measurements of RUVBL1/2 without any other protein component present. Mass distributions were plotted as kernel density estimates (KDEs). A kernel bandwidth of 5 kDa was used to generate the KDEs for the individual protein components, while a bandwidth of 10 kDa was used for the titration experiments. In the latter case, the number of lower mass species can increase simply through the increasing concentration of the non-RUVBL1/2 component, potentially influencing the probability density estimate of the complexes containing at least one RUVBL1/2 unit even if no binding were to occur. To minimize this effect, therefore, only species of a mass greater than 240 kDa were considered in generating the KDE. The value of 240 kDa was chosen since it does not truncate the RUVBL1/2 peak around 300 kDa but does exclude most of the species arising from any of RPAP3, PIH1D1 or RPAP3-PIH1D1.

### Nanoflow electron spray ionization mass spectrometry (NanoESI)

NanoESI mass spectrometry experiments were done in on a high mass Q-TOF-type instrument (Sobott et al., 2002) adapted for a QSTAR CL platform (MDS Sciex) (Chernushevich and Thomson, 2004). Proteins samples were prepared in 100-500 mM ammonium acetate (pH 7.5) to a final concentration of 3.5-16  $\mu$ M, and 2  $\mu$ L of solutions were electrosprayed from gold-plated borosilicate glass capillaries made in-house as described elsewhere (Hernandez and Robinson, 2007). For mass spectrometry experiments, typical conditions employed capillary voltage at 1.3 kV, declustering potential of 90-100 V, focusing potential of 150 V, declustering potential

two of 15 V, focusing rod offset varied from 60 to 100V, and MCP of 2550 V. External calibration was done by using a 100 mg/mL aqueous solution of cesium iodide (Sigma-Aldrich) (Park et al., 2010).

### Negative-stain electron microscopy

Untagged RUVBL1/2 samples were used at 0.05 mg/mL, and 10  $\mu$ L were applied to a carbon-plated grid previously glow-discharged and, subsequently, negatively stained with 0.8% (w/v) uranyl formate or 1% (w/v) uranyl acetate. Samples were imaged in a JEOL 2010F transmission electron microscope operated at 200 kV. Images were collected at 50,000x magnification with an electron dose of  $10 \text{ e}^-/\text{\AA}^2$ , recorded on SO-163 films (Kodak), scanned on a Super COOLSCAN 9000 ED (Nikon) at 6.35  $\mu\text{m}/\text{pixel}$  and averaged 2x to produce data at 2.54  $\text{\AA}/\text{pixel}$ . Particles were extracted interactively from digitalized fields using the “Boxer” program (EMAN) (Ludtke et al., 1999). For eXact tag RUVBL1/2 complexes, proteins were expressed and purified as previously reported by our group (Nano et al., 2020). Briefly, bacterial cells transformed with the plasmid for co-expression of RUVBL1-H<sub>6</sub> and eXact tag-RUVBL2 (Table S5) were grown at 37 °C until OD<sub>600</sub> = 0.6. The temperature was then decreased to 18 °C and protein expression was induced overnight by 1 mM IPTG. Cells were harvested by centrifugation at 3,000 x g for 10 minutes, resuspended in buffer A and disrupted by sonication on ice. The lysate was spun down at 12,000 x g for 30 min at 4 °C, the supernatant collected and submitted to IMAC, His-tag removal and ion exchange chromatography as described in the second and third paragraphs of the “Protein expression and purification” section of Method Details. Negative staining was done by deposition of eXact tag RUVBL1/2 on a glow-discharged carbon-coated copper grid, followed by washing with two drops of ultrapure water and staining with two drops of 0.75% (w/v) uranyl formate (Ohi et al., 2004). Images were collected in a T12 (FEI) at 1-2 mm defocus and recorded using a 4k CCD camera (Gatan) (Ewens et al., 2016).

### Cross-linking followed by mass spectrometry (XL-MS)

Cross-linking of human R2TP was done with 4.4  $\mu\text{M}$  of the complex consisting of one RUVBL1/2 hexamer bound to three RPAP3-PIH1D1 in buffer M. Proteins were crosslinked with a 250-fold molar excess MS-cleavable membrane-permeable crosslinker, disuccinimidyl sulfoxide (DSSO, Thermo Scientific). Briefly, proteins were reduced with 10 mM (DTT), alkylated with 50 mM iodoacetamide, denatured with 2 M Urea and 0.01 % ProteaseMAX surfactant (Promega) and digested with Trypsin Gold 1:20 (w/w) (Promega) at 37 °C for two hours. Peptides were desalted using C-18 packed TopTip (Glygen) and dried using a SpeedVac Concentrator (SVC 100H, Savant). After resuspension in 10% formic acid, peptides were subjected to strong cation exchange chromatography in a Luna SCX column (50 x 2 mm, 5  $\mu\text{m}$ , 100  $\text{\AA}$ , Phenomenex) connected to an Agilent 1100 HPLC system following the method previously described (Liu et al., 2015). Fractions (96 in total) were compiled into 5 pools based on the elution profile. Peptides were desalted using C-18 packed TopTip (Glygen) and dried.

After 100-fold dilution, 5  $\mu\text{L}$  of the DSSO cross-linked peptides were separated by reverse phase chromatography using an EASY-nLC 1000 (Thermo Fisher Scientific) with an in-house prepared reverse phase nano-analytical column Reprosil-Pur 120 C-18-AQ (75  $\mu\text{m}$  I.D., 25 cm length, 3  $\mu\text{m}$ , 120  $\text{\AA}$ , Dr. Maisch GmbH), at a flow rate of 400 nL/min. The chromatography system was coupled to an Orbitrap Fusion Tribrid mass spectrometer (Thermo Fisher Scientific) equipped with a Nanospray Flex NG source (Thermo Fisher Scientific). The Orbitrap Fusion 3.0 instrument parameters were as follows for the Orbitrap (OT-MS) with MS2 OT-CID and DSSO mass doublet triggered MS3 IT-CID analysis: Nano-electrospray ion source with spray voltage 2.55 kV, capillary temperature 275 °C. Survey MS1 scan m/z range 400-1800 profile mode, resolution 60,000 FWHM@200m/z one microscan with maximum inject time 50 msec. Data-dependent acquisition Orbitrap survey spectra were scheduled at least every 5 sec, with the software determining ‘Top-speed’ number of MS/MS acquisitions during this period. The automatic gain control (AGC) target values for FTMS and MSn were 400,000 and 50,000 (MS2) and 10,000 (MS3) respectively. The most intense ions charge state 4-10 exceeding 50,000 counts were selected for CID MSMS fragmentation with orbitrap detection in centroid mode. Monoisotopic Precursor Selection (MIPS) was enabled, and Dynamic exclusion settings were as follows: repeat count 1; exclusion duration 18 sec with a 5 ppm mass window. The ddMS2 OT CID scan used a quadrupole isolation window of 1.6 Da; 15,000 Orbitrap resolution normal scan range, centroid detection, first mass 120 m/z, 1 microscan, 120 msec maximum injection time and normalized collision energy setting 25%. When a mass difference of 31.9721 m/z corresponding to a DSSO crosslink signature was observed in the CID-MS2 scan, an additional ddMS<sup>3</sup> IT CID was triggered on both ions for the top 4 most intense signals, charge state 2-6 using an MS isolation window 2 m/z, MS2 isolation window 2 m/z, IonTrap rapid scan rate centroid detection, 1 microscan, 100 msec maximum injection time, CID activation time 10 msec injection time, AGC target 10,000 and collision energy 30%.

Raw files were created by XCalibur 4.1.31.9 (Thermo Fisher Scientific) software and analyzed with the Proteome Discoverer software suite 2.2 (Thermo Fisher Scientific) with incorporated XlinkX nodes. Spectra were matched against the *H. sapiens* database from SwissProt (version 2018\_06, 20 349 sequences, downloaded from UniProt). The protease was set to ‘Trypsin’, and the maximum number of missed cleavages was defined as 2. Carbamidomethylation of cysteines was set as a fixed modification and oxidation of methionine as variable modification. For the linear peptide search, precursor mass tolerance was defined as 10 ppm, and fragment mass tolerance was defined as 0.6 Da. Cross-linked peptides were matched against a protein sequence database of RT2P complex subunits, with crosslink modification set to DSSO/ +158.004 Da (K), the minimum peptide length to 5, minimum peptide mass to 300, and the maximum peptide mass to 7000. The precursor mass tolerance was set to 10 ppm, FTMS fragment mass tolerance was set at 20 ppm and ITMS fragment mass was set at 0.5 Da. FDR threshold was set to 0.01 (1%), and FDR strategy was set as ‘Percolator’. Visualization of cross-linked peptides was done using the xiVIEW tool (Graham et al., 2019).

### Affinity purification followed by mass spectrometry (AP-MS)

HEK293T extracts were produced by lysing cells using buffer O, followed by sonication. After removal of cellular debris by centrifugation (10,000 x g, 10 min, 4°C), cell lysates were incubated for 30 min on ice with recombinant purified His<sub>12</sub>-SUMO-RPAP3 ND previously immobilized on HisPur Co<sup>2+</sup> beads (Thermo Fisher Scientific). Control experiments were performed incubating cell extracts with immobilized His<sub>12</sub>-SUMO on Co<sup>2+</sup> beads. Beads were washed four times with buffer P and elution of His<sub>12</sub>-SUMO-RPAP3 ND-interacting proteins was performed using Ulp1 protease. All control samples were submitted to the same treatment. Mass spectrometry analysis was performed based on previously described (Wu et al., 2019). Samples were reduced with 5 mM TCEP for 30 min, alkylated with 15 mM iodoacetamide for 30 min in the dark, followed by denaturation with 2M Urea and subsequent digestion by overnight incubation with Trypsin Gold 1:20 (w/w) (Promega) at 37 °C. C18 packed TopTip (Glygen) was used to desalt tryptic peptides, that were subsequently dried in a SpeedVac vacuum concentrator (SVC 100H, Savant) and resuspended in 0.1% (v/v) formic acid. Peptides were separated by chromatography using an in-house packed nano C18 column (10 cm x 75 µm ID, 3 µm, 100 Å) connected to a Proxeon EASY-nCL 1000 (Thermo Fisher Scientific). A water/acetonitrile/0.1% (v/v) formic acid 100 min gradient at flow rate of 300 nL/min, consisting of 1% to 3% acetonitrile increase in the first 2 min, followed by a linear gradient from 3% to 24% acetonitrile for 74 min, a linear gradient from 24% to 100% for 14 min, and a 10 min wash with 100% acetonitrile, was employed. Eluted peptides were directly sprayed into the Orbitrap Elite Mass Spectrometer (Thermo Fisher Scientific) by positive electrospray ionization at an ion source temperature of 250 °C and ion spray voltage of 2.1 kV. Full-scan mass spectrometry spectra (m/z 350-2,000) were collected in the Orbitrap at 60,000 (m/z 400) resolution. Automatic gain control was set to 1e6 for full FTMS scans and 5e4 for MS/MS scans. The 15 most intense ions with charge state ≥ 2 were isolated and fragmented in the linear ion trap by low-energy CID. Ions intensity exceeding 1,500 counts were submitted to CID with normalized collision energy set at 35%, activation Q at 0.250 and an activation time of 10 ms. MS raw files were converted into mzXML format and identification of peptides was performed using SEQUEST (Eng et al., 1994) against human proteins sequences. Only identified peptides with probability higher than 80% were used for further analysis. Filtering of identified proteins was performed using CRAPome server (Mellacheruvu et al., 2013). DAVID server (Huang et al., 2009b) was used for functional enrichment analysis and InteractiVenn (Heberle et al., 2015) was employed for generation of Venn diagrams.

### QUANTIFICATION AND STATISTICAL ANALYSIS

Statistical analyses are described in figures and tables. Data in Table S1 represents mean ± SD for each experiment calculated by ASTRA 7.1 software. In Table S2, Guinier data represents mean ± SD calculated by PRIMUS software for individual merged curves. In Figure 3F and Table S2, EOM data for RPAP3 are described as mean ± SD from 10 simulations calculated in Origin 7 software. In Table S2, RPAP3-PIH1D1 CORAL data represents mean ± SD from the 7 representative models calculated using Origin 7 software. In Figures 7A–7C and S3F, values representing mean ± SD were calculated in Origin 7 software from at least 3 experiments. Data in Figure 7D are described as box charts, where interquartile range (large box), mean (small box), median (horizontal line), 5<sup>th</sup> and 95<sup>th</sup> percentile (whiskers) and maximum and minimum values (asterisks), were calculated in Origin 7 software from at least 3 experiments. Statistical *p*-values in Figure 8 and Table S3 were determined by a modified Fisher Exact *p*-value, EASE score, by DAVID server.

**Figure S1. Far-UV circular dichroism spectra of R2TP proteins, Related to Figures 2 and 3.**

The folded state of the recombinant proteins used in this work are shown as monitored by CD.

Figure S1

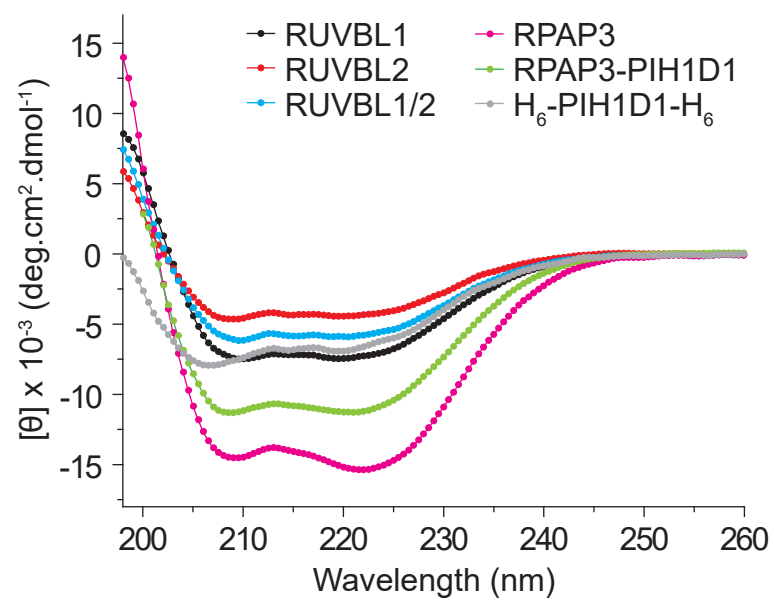


**Figure S2. Characterization of RUVBL1 and RUVBL2 assembly and structure, Related to Figure 2.**

(A) The oligomeric states of RUVBL1, RUVBL2 and RUVBL1/2 at several concentrations (concentrations refer to monomers) in the absence or presence of 1.5 mM ATP were analyzed by SEC. 1 mL fractions were collected and inspected by silver-stained 12% SDS-PAGE gels. Molecular masses of protein standards are indicated on top.

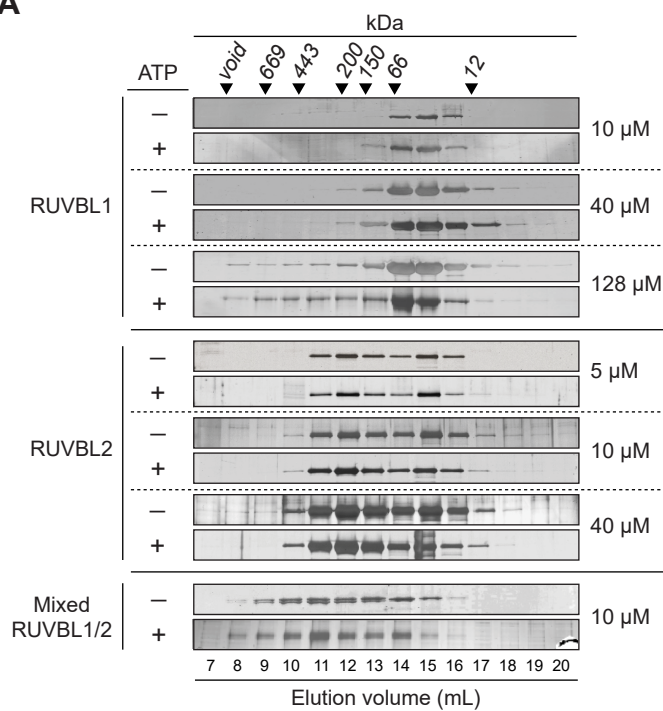
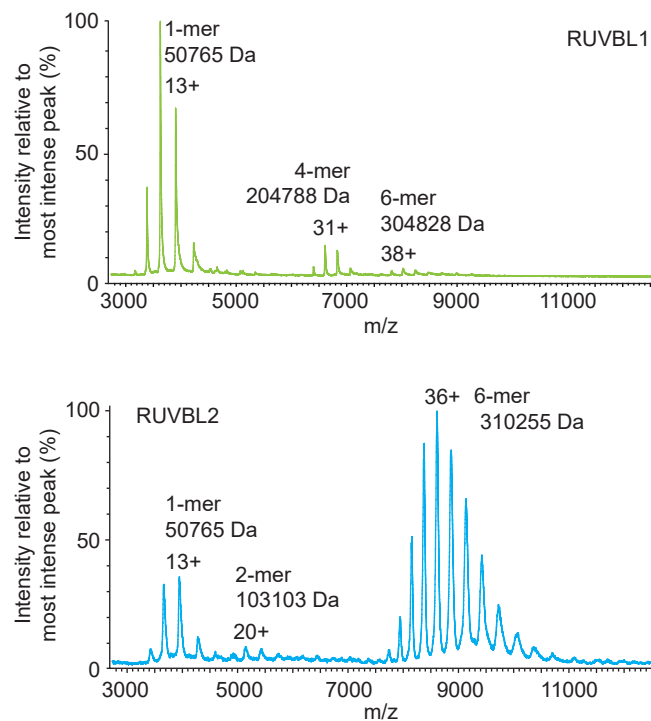
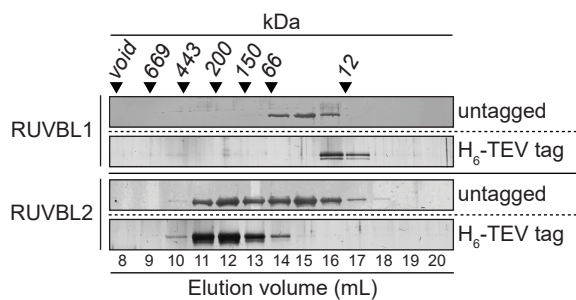
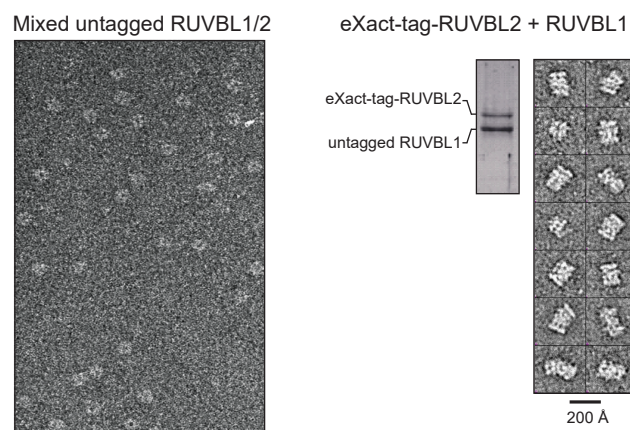
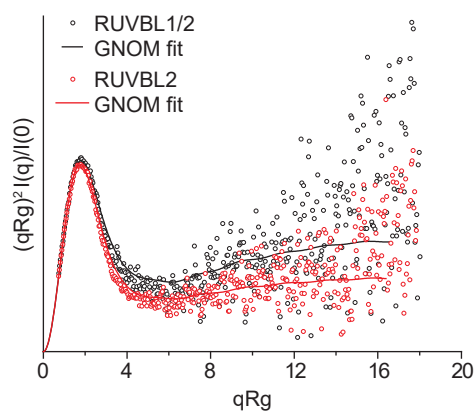
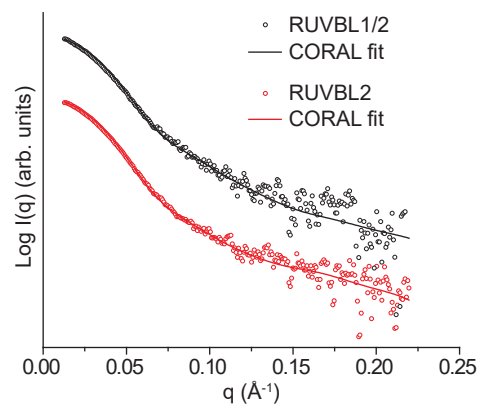
(B) NanoESI mass spectrometry analysis of RUVBL1 (top graph) and RUVBL2 (bottom graph). Identified species and their respective molecular masses are indicated in the graphs.

(C) Effect of the N-terminal His-tag on the RUVBL1 and RUVBL2 oligomeric states as determined by SEC. 1 mL fractions were evaluated by silver-stained 12% SDS-PAGE gels.

(D) Negative-stain transmission electron microscopy of the RUVBL1/2 complex. On the left side, single heterohexamers of untagged RUVBL1/2 are shown, whereas untagged RUVBL1/eXact-tag-RUVBL2 heterododecamers are displayed on the right.

(E) Dimensionless Kratky analysis of the RUVBL2 (red) and RUVBL1/2 complex (black). Experimental data are shown as circles and GNOM fits are represented by solid lines.

(F) Comparison between experimental (circles) and simulated (CORAL fit, solid lines) SAXS profiles of RUVBL2 (red) and RUVBL1/2 (black) obtained after the generation of high-resolution CORAL models.

**Figure S2****A****B****C****D****E****F**

**Figure S3. Characterization of RPAP3 iso1 and RPAP3 iso1-PIH1D1 complex structures, Related to Figure 3.**

(A) Analytical ultracentrifugation sedimentation velocity of RPAP3 iso1. Sedimentation coefficient, frictional ratio ( $f/f_0$ ) and molecular mass are shown in the graph.

(B) RPAP3 iso1 secondary structure (performed by PSIPRED server), disorder (performed using DISOPRED server) and coiled-coil potential (performed by MARCOIL server) predictions. Amino acid residues containing disorder index above 0.5 (black dashed line) are considered as part of disordered regions; the closer to 1.0 the red line is, the higher is the probability of coiled-coil formation.

(C) Far-UV circular dichroism spectrum of RPAP3 N-terminal domain (RPAP3 ND, amino acids 1-125) showing its intrinsic disordered state. The spectrum of GdnHCl-denatured RPAP3 ND is shown for comparison.

(D) Far-UV circular dichroism spectra of RPAP3 ND at increasing temperatures (20°C to 80°C). Inset shows the spectra normalized by the MRE-values at 222 nm.

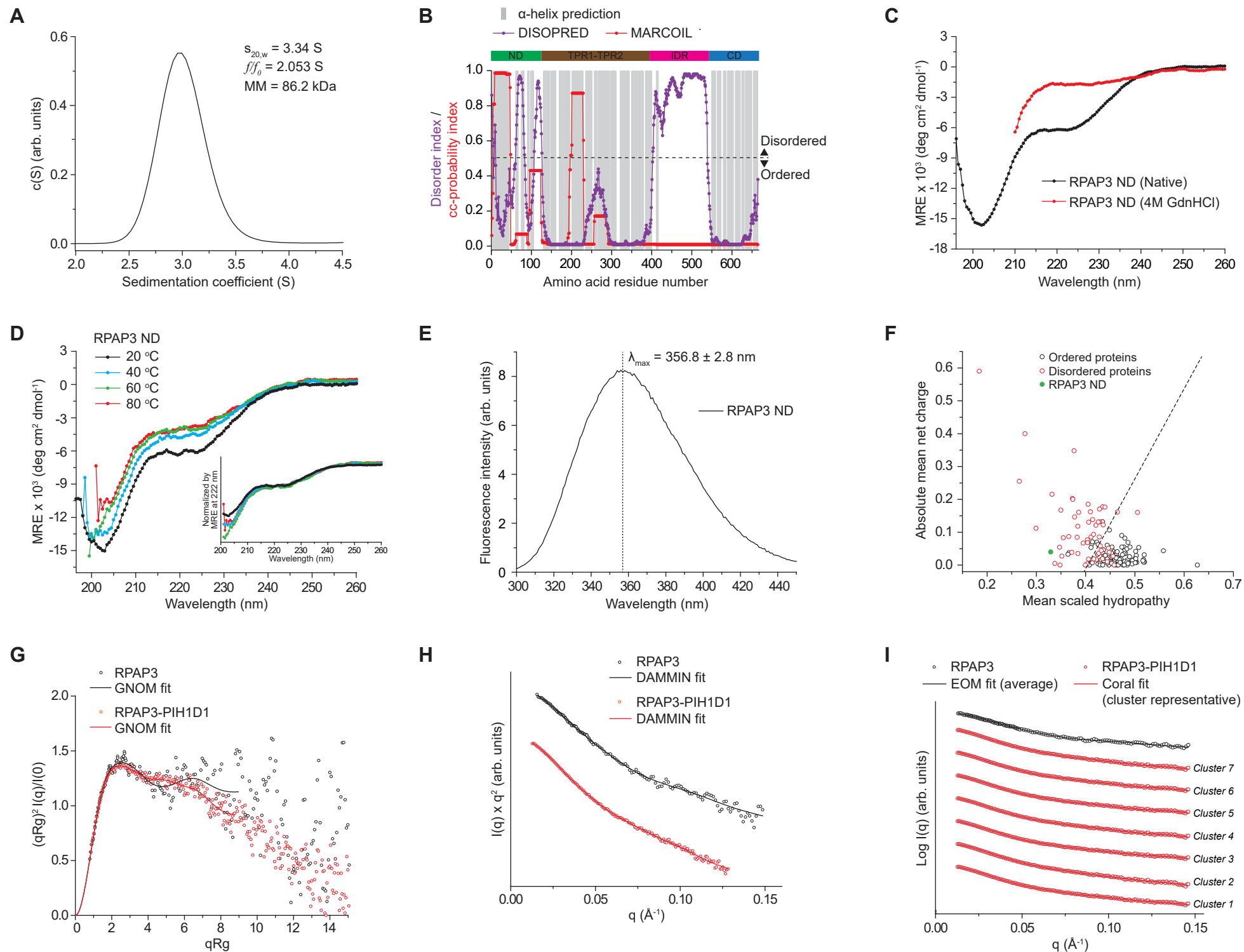
(E) Tryptophan fluorescence emission spectrum of RPAP3 ND. The two tryptophan residues (W31 and W93) within the ND were found to be solvent-exposed ( $\lambda_{\text{max}} = 356.8 \pm 2.8$  nm).

(F) Hydropathy index calculated for RPAP3 ND (green solid circle) by PONDR server. Typical hydropathy indices for ordered (black empty circles) and disordered proteins (red empty circles) are shown as references.

(G) Dimensionless Kratky analysis of RPAP3 iso1 (black) and RPAP3 iso1-PIH1D1 complex (red). Experimental data are shown as circles and GNOM curves are displayed as solid lines.

(H) RPAP3 iso1 (black) and RPAP3 iso1-PIH1D1 (red) experimental SAXS curves (circles) compared to simulated SAXS curves of the *ab initio* DA models (solid lines).

**(I)** Colored in black is the comparison between RPAP3 iso1 experimental SAXS profile (circles) and the averaged simulated SAXS curve obtained for the selected ensemble of RPAP3 iso1 conformers (EOM fit, solid line) generated by EOM analysis. Shown in red are the comparisons between RPAP3 iso1-PIH1D1 experimental SAXS curve (circles) and cluster representative CORAL structures curves (solid line).

**Figure S3**

**Figure S4. Mapping interactions among the R2TP subunits, Related to Figures 4 and 5.**

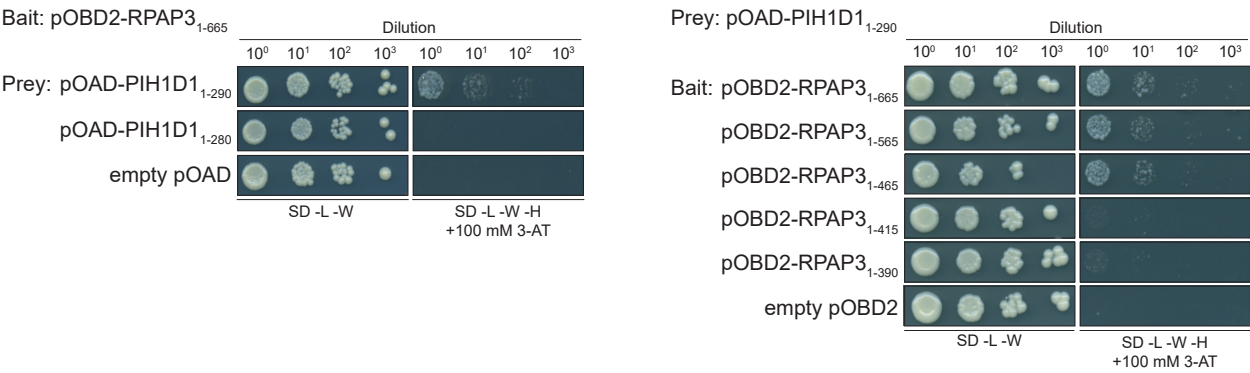
**(A)** Identification of interacting interfaces between RPAP3 iso1 and PIH1D1 by yeast 2-hybrid assay. On the left, PIH1D1<sub>1-290</sub> and PIH1D1<sub>1-280</sub> were used as preys, and full-length RPAP3 iso1 was used as bait. On the right, PIH1D1<sub>1-290</sub> was used as prey, whereas full-length RPAP3 iso1 and its C-terminal truncation mutants were used as baits. Yeast cells transformed with both RPAP3 and PIH1D1-containing plasmids were grown in SD -L -W and SD -L -W -H +100 mM 3-AT plates. Cells transformed with empty plasmids were used as negative controls (empty pOBD2 or pOAD).

**(B)** Analysis of R2TP complex assembly by cross-linking mass spectrometry analysis (XL-MS). RPAP3 iso1, PIH1D1, RUVBL1 and RUVBL2 are colored in green, red, yellow, and blue, respectively. Domain boundaries are indicated. Crosslinked peptides between two of the R2TP subunits are shown as black solid lines; intra-crosslinked peptides are depicted by solid gray lines.

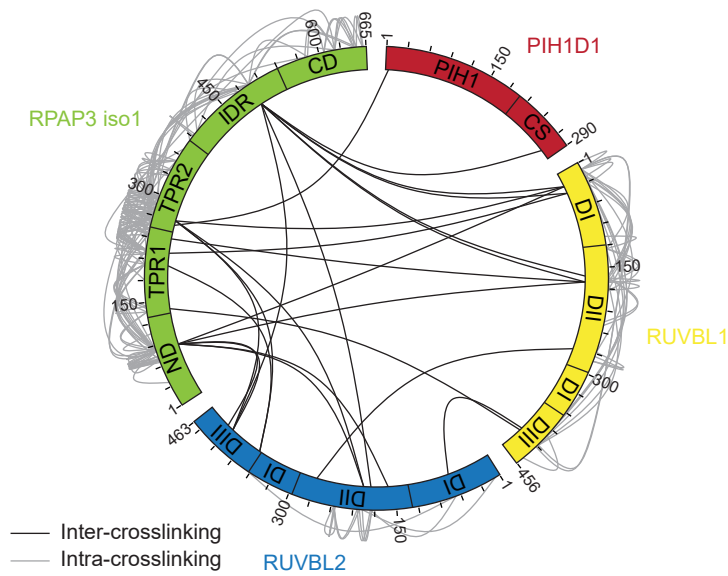
**(C)** Pull-down experiments were carried out with untagged RUVBL proteins constructs to test for unspecific protein binding to Co<sup>2+</sup> beads.

Figure S4

A



B



C

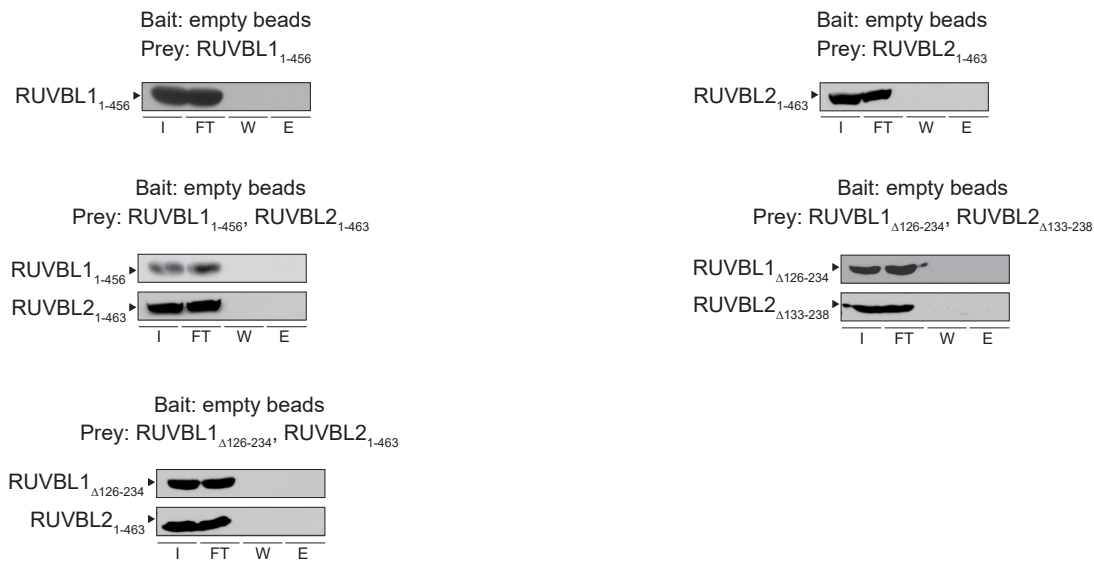
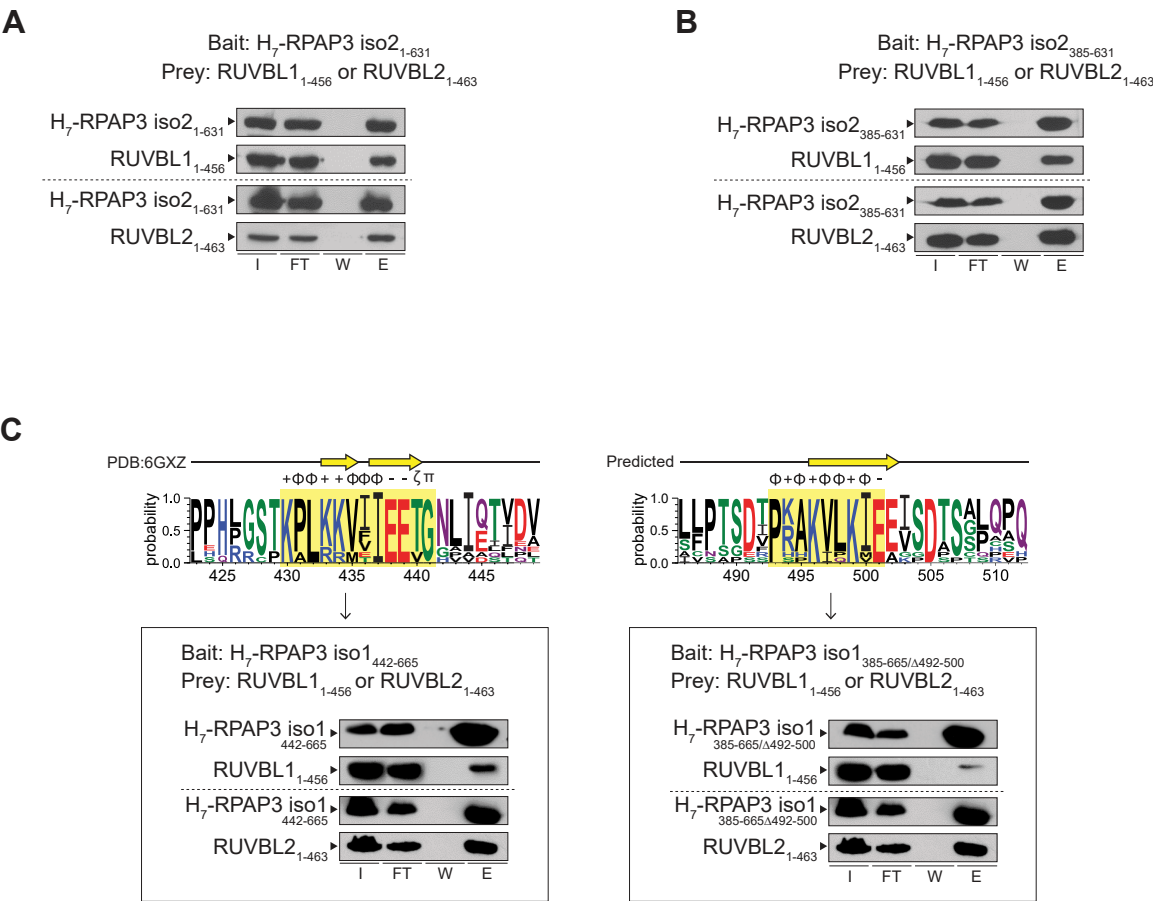


**Figure S5. Pull-down assays to identify regions required for interactions among R2TP subunits, Related to Figure 4.**

**(A-B)** The interactions between RPAP3 iso2 constructs and RUVBL proteins using pull-down assays are shown.

**(C)** On the left panel, the RPAP3 truncation lacking the region 430-441 (H<sub>7</sub>-RPAP3 iso1<sub>442-665</sub>) was used to pull-down RUVBL1<sub>1-456</sub> or RUVBL2<sub>1-463</sub>. Shown on the right is the pull-down using the RPAP3 iso1 truncation with the 492-500 region deleted (H<sub>7</sub>-RPAP3 iso1<sub>385-665/Δ492-500</sub>) as bait and RUVBL1<sub>1-456</sub> or RUVBL2<sub>1-463</sub> as preys. Deleted amino acid sequences are highlighted in yellow in the sequence logos.

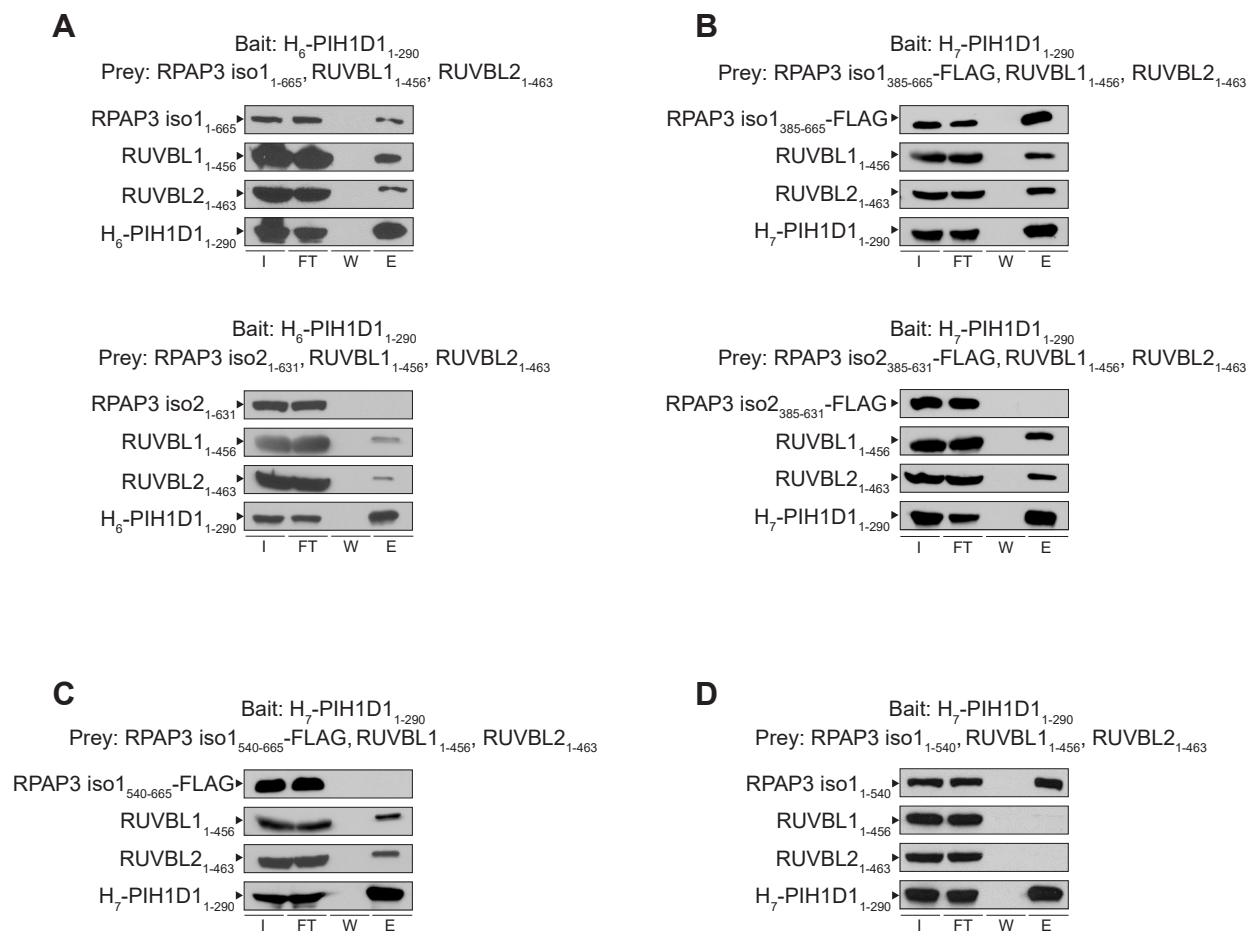
Figure S5



**Figure S6. Pull-down assays to identify regions required for interactions among R2TP subunits, Related to Figure 5.**

**(A-D)** Pull-down assays were carried out with baits and preys as indicated at the top of each panel.

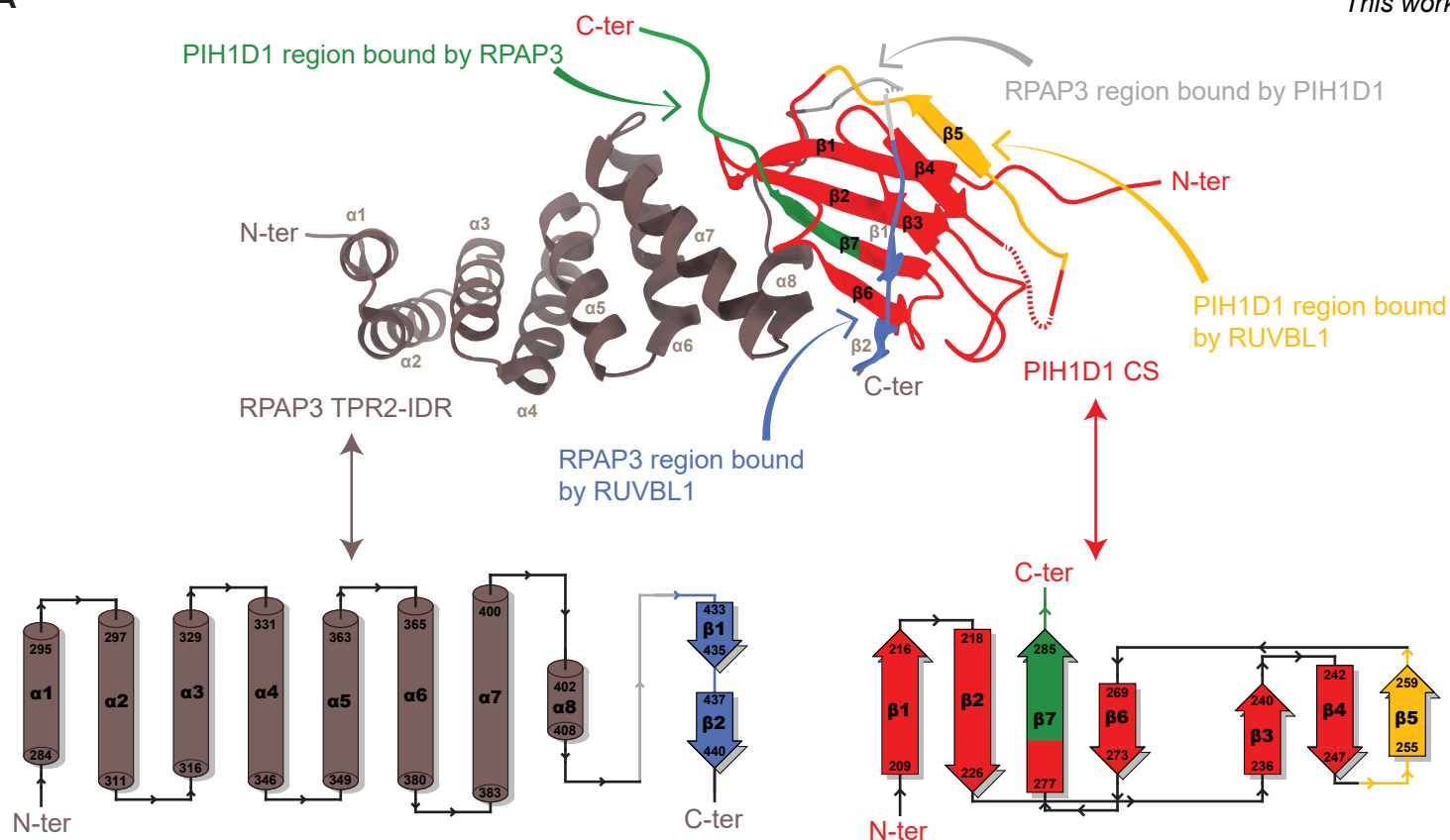
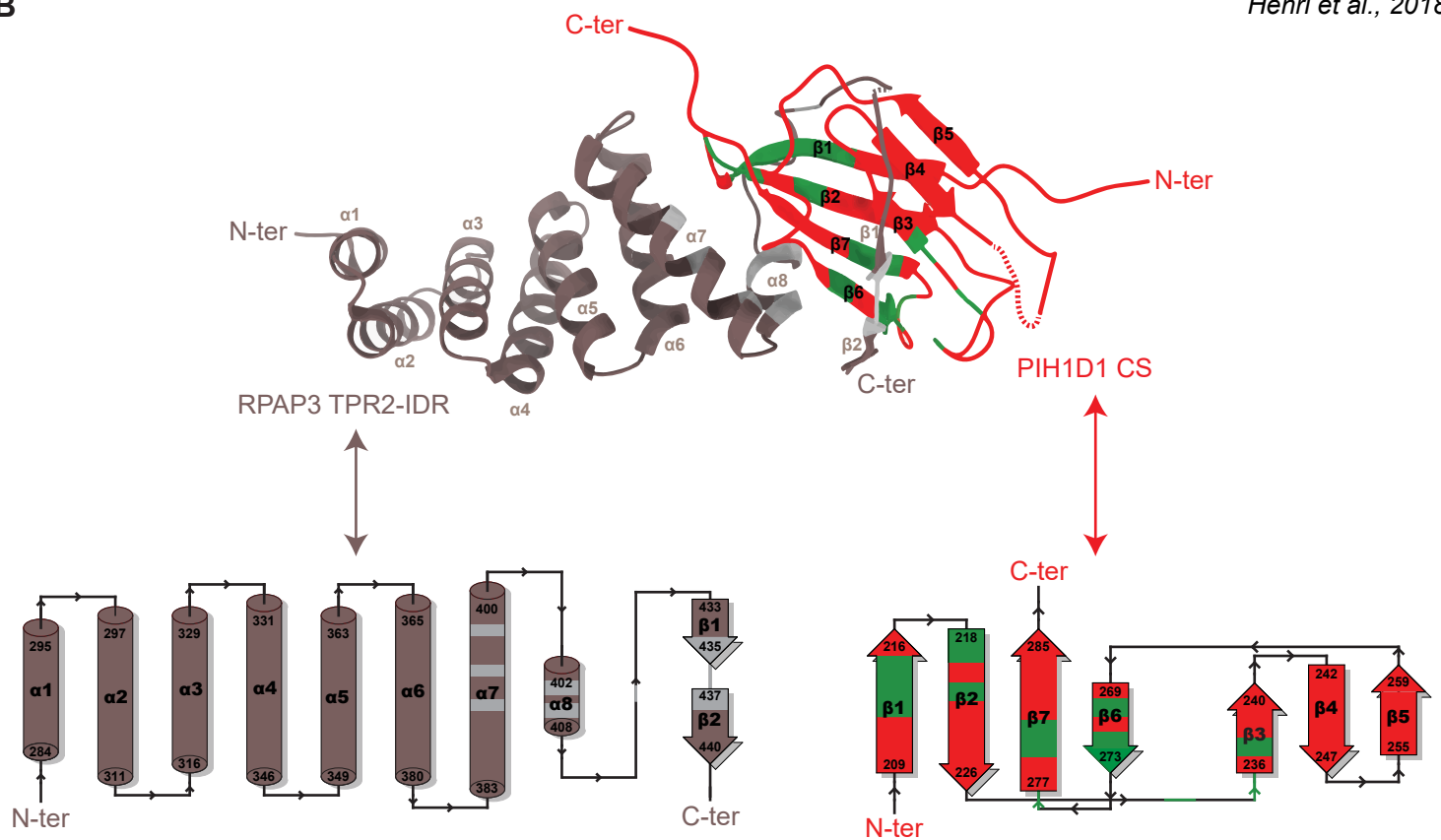
Figure S6



**Figure S7. Comparison of R2TP-binding interfaces identified in this work and in previously published studies, Related to Figure 9.**

(A) Co-crystal structure of RPAP3 iso1 TPR2 + IDR in complex with PIH1D1 CS domain (top, PDB ID: 6GXZ) and structure diagrams (bottom) displaying binding interfaces identified in this work. The RPAP3 iso1 region that binds PIH1D1 (gray), the PIH1D1 region that binds RPAP3 iso1 (green), the PIH1D1 region that binds RUVBL1 (orange), and the RPAP3 region that binds RUVBL1 (blue) are shown.

(B) Co-crystal structure of RPAP3 iso1 TPR2 + IDR in complex with PIH1D1 CS domain (top, PDB ID: 6GXZ) and structure diagrams (bottom) displaying binding interfaces identified by Henri et al. (Henri et al., 2018). Shown in green are the PIH1D1 regions that bind to RPAP3 iso1. The RPAP3 iso1 regions that bind to PIH1D1 are colored in gray.

**Figure S7****A***This work***B***Henri et al., 2018*

**Table S1. Molecular masses measured by SEC-MALS, Related to Figures 2 and 3.**

Sample	Concentration (mg/mL)	Molecular weight (kDa)	Oligomeric state
RUVBL1	1	45.1 ± 0.5	Monomer
	2	54.2 ± 0.2	Monomer
	5	57.8 ± 1.4	Monomer
		95.9 ± 15.7	Dimer
RUVBL2	1	61.4 ± 1.6	Monomer
		317.2 ± 1.5	Homohexamer
	2	57.0 ± 1.4	Monomer
		323.5 ± 0.7	Homohexamer
	5	56.4 ± 1.1	Monomer
		316.1 ± 1.3	Homohexamer
RUVBL1/2 <sup>a</sup>	1	60.0 ± 3.8	Monomer
		93.1 ± 11.1	Heterodimer
		374.5 ± 2.7	Heterohexamer
	2	52.6 ± 0.6	Monomer
		110.4 ± 4.3	Heterodimer
		315.9 ± 2.1	Heterohexamer
	5	51.4 ± 2.4	Monomer
		102.3 ± 7.0	Heterodimer
		339.5 ± 2.1	Heterohexamer
RPAP3	1	74.0 ± 8.3	Monomer
	2	70.3 ± 7.0	Monomer
	3	78.8 ± 3.0	Monomer
RPAP3-PIH1D1 <sup>a</sup>	1	114.5 ± 4.3	Heterodimer
	2	108.9 ± 5.5	Heterodimer
	3	108.6 ± 4.9	Heterodimer

<sup>a</sup>Total concentration considering 1:1 stoichiometry.

Standard deviations are shown for each molecular weight determination.

**Table S2. Size and dimension parameters determined by SAXS, Related to Figures 2 and 3.**

Sample	R <sub>g</sub> (Å)		D <sub>max</sub> (Å)
RUVBL2	Guinier	51.3 ± 0.8	N.A.
	P(r)	51.0	158
	CORAL <sup>a</sup>	48.4	166
RUVBL1/2	Guinier	52.9 ± 1.4	N/A
	P(r)	51.3	162
	CORAL <sup>a</sup>	47.2	168
RPAP3	Guinier	53.1 ± 1.0	N.A.
	P(r)	60.3	220
	DAM <sup>b</sup>	62.5	222
	EOM	60.0 ± 1.2	194 ± 7
RPAP3-PIH1D1	Guinier	65.0 ± 2.2	N.A.
	P(r)	67.5	240
	DAM <sup>b</sup>	66.1	245
	CORAL <sup>c</sup>	64.8 ± 3.9	252 ± 31

Hydrodynamic parameters estimated from the CORAL<sup>a</sup> and refined DA<sup>b</sup> models by the Hydropro 10 software.

<sup>c</sup>Averaged parameters estimated by the Hydropro 10 software from the 7 CORAL representative models.

Standard deviations are shown.

**Table S3. DSSO inter-cross-linked peptides identified by mass spectrometry, Related to STAR Methods and Figure S4B.**

Protein A	Peptide A <sup>a</sup>	Position	Protein B	Peptide B <sup>a</sup>	Position	XLinkX score
PIH1D1	AAFHR[K]RK	275	RPAP3	A[K]VLK	495	20.16
PIH1D1	MANP[K]LLGMGLSEAEAIGADSAR	5	RPAP3	EADIVI[K]STEGE	264	12.15
RPAP3	EENT[K]NR	82	RUVBL2	VG[K]LTLK	160	146.94
RUVBL1	IASHSHV[K]GLGLDESLAK	22	RPAP3	[K]QIEAQQNK	271	235.57
RUVBL1	IASHSHV[K]GLGLDESLAK	22	RPAP3	EENT[K]NR	82	22.2
RUVBL1	TISHVIIGL[K]TAK	162	RPAP3	A[K]VLK	495	165.58
RUVBL1	IASHSHV[K]GLGLDESLAK	22	RPAP3	A[K]VLK	495	145.83
RUVBL1	QL[K]LDPSIFESLQK	171	RPAP3	A[K]VLK	495	40.98
RUVBL1	QL[K]LDPSIFESLQK	171	RPAP3	EENT[K]NR	82	112.96
RUVBL1	GLGLDESLA[K]QAASGLVGQENAR	33	RPAP3	A[K]VLK	495	32.12
RUVBL1	GLGLDESLA[K]QAASGLVGQENAR	33	RPAP3	LEEAK[K]KDYER	221	211.64
RUVBL1	ING[K]DSIEK	422	RPAP3	ALVL[K]EK	137	124.33
RUVBL1	QL[K]LDPSIFESLQK	171	RPAP3	[K]ISQALASK	243	197.86
RUVBL1	YSVQLLTPANLLA[K]INGKDSIEK	418	RUVBL2	EG[K]IAGR	67	212.02
RUVBL2	TQGFLALFSGDTGEI[K]SEVR	269	RUVBL1	KTEITD[K]LR	274	285.43
RUVBL2	DKVQAGDVITID[K]ATGK	197	RPAP3	[K]QIEAQQNK	271	289.49
RUVBL2	[K]GTEVQVDDIKR	417	RPAP3	EENT[K]NR	82	295.2
RUVBL2	KGTEVQVDDI[K]R	427	RPAP3	EENT[K]NR	82	207.3
RUVBL2	LLIVSTTPYSE[K]DTK	365	RPAP3	[K]QIEAQQNK	271	206.43
RUVBL2	LLIVSTTPYSE[K]DTK	365	RPAP3	SYT[K]AYSR	202	131.66
RUVBL2	DKVQAGDVITID[K]ATGK	197	RPAP3	EENT[K]NR	82	229.02
RUVBL2	[K]GTEVQVDDIKR	417	RPAP3	A[K]VLK	495	11.15
RUVBL2	D[K]VQAGDVITIDK	186	RPAP3	A[K]VLK	495	122.34
RUVBL2	[K]GTEVQVDDIKR	417	RPAP3	[K]QIEAQQNK	271	19.79

<sup>a</sup>Cross-linked lysine residues are shown within brackets.

**Table S4. DAVID enrichment analysis for RPAP3 N-terminal domain interactors, Related to Figure 8D.**

Type	ID / Description	Proteins	p-value ( $\leq 0.05$ )
Protein domain	IPR016024 Armadillo-type fold	USP24, NBAS, FHOD1, TBCD, UBR4, TTI2, CAND1, ARMC6, VEPH1, CFAP69, ELMO2, MROH7, CLASP1, UNC79	0.000060167
	IPR013126 Heat shock protein 70 family	HSPA8, HSPA1L, HSPA7, HSPA6	0.000418929
	IPR001715 Calponin homology domain	SPECC1, EHBP1L1, SYNE1, SPTBN2, PLEC	0.0072854
	IPR000082 SEA domain	MUC1, MUC16, TMPRSS11F	0.024099331
	IPR013026 Tetratricopeptide repeat-containing domain	IFT88, NASP, CDC27, IFIT5, TONSL	0.044658965
	IPR014010 Egg jelly receptor, REJ-like	RNPS1, PKD1L2	0.04938001
GO: Cellular component	GO:0016324 Apical plasma membrane	CNTFR, SLC9A3R1, MUC1, FZD3, CDH2, STK26, ATP6V0A4, GNAT1, DLL1, SPTBN2	0.002116704
	GO:0097546 Ciliary base	CEP126, DISC1, GLI3, GLI2	0.002184026
	GO:0005814 Centriole	IFT88, CROCC, HSPA6, CAPG, DZIP1, SDCCAG8	0.004813626
	GO:0005813 Centrosome	SLC9A3R1, CEP126, CROCC, STK26, CDC27, AKAP9, UBR4, DISC1, RAB11FIP3, CLASP1, SDCCAG8	0.00856292
	GO:0097060 Synaptic membrane	PRKCG, AKAP9, LRP4	0.012819103
	GO:0045111 Intermediate filament cytoskeleton	ZNF175, PCDHB4, NFATC4, PLEC	0.013841878
	GO:0072562 Blood microparticle	HSPA8, ITIH4, HSPA1L, IGLL1, HSPA7, HSPA6	0.016100695
	GO:0005829 Cytosol	NBAS, GOSR1, GLI3, CENPC, TTN, GLI2, ZMYM2, NUF2, CDC27, AOX1, PHGDH, GNAT1, BUB1, RAB11FIP3, CLASP1, SNX6, SPTBN2, PRKCG, HSPA8, EIF2B3, HSPA1L, VPS13C, HSPA6, ARAP2, CTPS2, NEB, ANK3, NFATC4, AIMP2, MYH2, RRAGA, STK26, AKAP9, ACOT1, ELMO2, RNPS1, EIF3F, PLIN1, PLCD3, TKT, OPTN, PLEC, SDCCAG8	0.034454162
	GO:0043231 Intracellular membrane-bounded organelle	SLC9A3R1, SQLE, RRAGA, PARG, AKAP9, IFIT5, UGT2A3, WBP11, SEC23B, RAB11FIP3, SNX6	0.04470826
	GO:0008180 COP9 signalosome	HSPA1L, HSPA7, HSPA6	0.044813767
	GO:0019898 Extrinsic component of membrane	CNTFR, MUC16, VPS13C, SNX6	0.045047616

	GO:0016020 Membrane	CNTFR, NBAS, DDX24, FHOD1, CPNE6, GOSR1, UBR4, PKD1L2, GLI2, SLC9A3R1, CAND1, CDH2, NUF2, GNAT1, SEC23B, BUB1, CLASP1, SPECC1, HSPA8, FMO2, KRT10, IL17RB, SMARCA4, HCFC1, AIMP2, IGLL1, EHBP1L1, SLCO2A1, ELMO2, EIF3F	0.050326167
--	------------------------	---	-------------

**Table S5. Plasmids used in this work, Related to STAR Methods.**

Plasmid	Purpose <sup>a, b</sup>	Source
pQLink H7-RUVBL1 <sub>1-456</sub>	His-tagged full-length RUVBL1 expression	This study
pQLink H7-RUVBL2 <sub>1-463</sub>	His-tagged full-length RUVBL2 expression	This study
p11 H <sub>6</sub> -RUVBL1 <sub>1-456</sub>	His-tagged full-length RUVBL1 expression	Nano <i>et al.</i> , 2020
p11 H <sub>6</sub> -RUVBL2 <sub>1-463</sub>	His-tagged full-length RUVBL2 expression	Nano <i>et al.</i> , 2020
pETSUMO2 H <sub>12</sub> -SUMO-RPAP3 iso1 <sub>1-665</sub>	His and SUMO-tagged full-length RPAP3 iso1 expression	This study
pCOLA Duet-1 RPAP3 iso1 <sub>1-665</sub> , H <sub>6</sub> -PIH1D1 <sub>1-290</sub>	Co-expression of untagged full-length RPAP3 iso1 and His-tagged full-length PIH1D1	This study
pQM18 H <sub>6</sub> -PIH1D1 <sub>1-290</sub> -H <sub>6</sub>	N and C-terminal His-tagged full-length PIH1D1 expression	Machado-Pinilla <i>et al.</i> , 2012
pCOLADuet-1 RPAP3 iso1 <sub>1-665</sub> , H <sub>6</sub> -PIH1D1 <sub>1-280</sub>	Co-expression of untagged full-length RPAP3 iso1 and His-tagged PIH1D1 residues 1-280	This study
pCOLADuet-1 RPAP3 iso1 <sub>1-430</sub> , H <sub>6</sub> -PIH1D1 <sub>1-290</sub>	Co-expression of untagged RPAP3 iso1 residues 1-430 and His-tagged full-length PIH1D1	This study
pCOLADuet-1 RPAP3 iso1 <sub>1-415</sub> , H <sub>6</sub> -PIH1D1 <sub>1-290</sub>	Co-expression of untagged RPAP3 iso1 residues 1-415 and His-tagged full-length PIH1D1	This study
pCOLADuet-1 RPAP3 iso1 <sub>1-390</sub> , H <sub>6</sub> -PIH1D1 <sub>1-290</sub>	Co-expression of untagged RPAP3 iso1 residues 1-390 and His-tagged full-length PIH1D1	This study
pQLink RUVBL1 <sub>1-456</sub> -RUVBL2 <sub>1-463</sub>	Untagged full-length RUVBL1 and RUVBL2 co-expression	This study
pQLink RUVBL1 <sub>1-456</sub> , RUVBL2 <sub>1-463</sub> , H <sub>7</sub> -PIH1D1 <sub>1-290</sub>	Co-expression of untagged full-length RUVBL1 and RUVBL2, and His-tagged full-length PIH1D1	This study
pQLink RUVBL1 <sub>1-456</sub> , RUVBL2 <sub>1-463</sub> , H <sub>7</sub> -PIH1D1 <sub>1-280</sub>	Co-expression of untagged full-length RUVBL1 and RUVBL2, and His-tagged PIH1D1 residues 1-280	This study
pQLink RUVBL1 <sub>1-456</sub> , RUVBL2 <sub>1-463</sub> , H <sub>7</sub> -PIH1D1 <sub>1-270</sub>	Co-expression of untagged full-length RUVBL1 and RUVBL2, and His-tagged PIH1D1 residues 1-270	This study
pQLink RUVBL1 <sub>1-456</sub> , RUVBL2 <sub>1-463</sub> , H <sub>7</sub> -PIH1D1 <sub>1-260</sub>	Co-expression of untagged full-length RUVBL1 and RUVBL2, and His-tagged PIH1D1 residues 1-260	This study
pQLink RUVBL1 <sub>1-456</sub> , RUVBL2 <sub>1-463</sub> , H <sub>7</sub> -PIH1D1 <sub>1-250</sub>	Co-expression of untagged full-length RUVBL1 and RUVBL2, and His-tagged PIH1D1 residues 1-250	This study
pQLink RUVBL1 <sub>1-456</sub> , RUVBL2 <sub>1-463</sub> , H <sub>7</sub> -PIH1D1 <sub>1-240</sub>	Co-expression of untagged full-length RUVBL1 and RUVBL2, and His-tagged PIH1D1 residues 1-240	This study

pQLink RUVBL1 <sub>1-456</sub> , H7-PIH1D1 <sub>1-290</sub>	Co-expression of untagged full-length RUVBL1 and His-tagged full-length PIH1D1	This study
pQLink RUVBL2 <sub>1-463</sub> , H7-PIH1D1 <sub>1-290</sub>	Co-expression of untagged full-length RUVBL2 and His-tagged full-length PIH1D1	This study
pQLink RUVBL1 <sub>Δ126-234</sub> , RUVBL2 <sub>Δ133-238</sub>	Co-expression of untagged RUVBL1 and RUVBL2, both lacking the external DII	This study
pQLink RUVBL1 <sub>Δ126-234</sub> , RUVBL2 <sub>1-463</sub>	Co-expression of untagged RUVBL1 lacking the external DII and full-length RUVBL2	This study
pQLink RUVBL1 <sub>1-456</sub> , RUVBL2 <sub>1-463</sub> , H7-RPAP3 iso1 <sub>1-665</sub>	Co-expression of untagged full-length RUVBL1 and RUVBL2, and His-tagged full-length RPAP3 iso1	This study
pQLink RUVBL1 <sub>1-456</sub> , RUVBL2 <sub>1-463</sub> , H7-RPAP3 iso1 <sub>125-665</sub>	Co-expression of untagged full-length RUVBL1 and RUVBL2, and His-tagged RPAP3 iso1 residues 125-665	This study
pQLink RUVBL1 <sub>1-456</sub> , RUVBL2 <sub>1-463</sub> , H7-RPAP3 iso1 <sub>1-540</sub>	Co-expression of untagged full-length RUVBL1 and RUVBL2, and His-tagged RPAP3 iso1 residues 1-540	This study
pQLink RUVBL1 <sub>1-456</sub> , H7-RPAP3 iso1 <sub>1-665</sub>	Co-expression of untagged full-length RUVBL1 and His-tagged full-length RPAP3 iso1	This study
pQLink RUVBL2 <sub>1-463</sub> , H7-RPAP3 iso1 <sub>1-665</sub>	Co-expression of untagged full-length RUVBL2 and His-tagged full-length RPAP3 iso1	This study
pQLink RUVBL1 <sub>1-456</sub> , H7-RPAP3 iso1 <sub>540-665</sub>	Co-expression of untagged full-length RUVBL1 and His-tagged RPAP3 iso1 residues 540-665	This study
pQLink RUVBL2 <sub>1-463</sub> , H7-RPAP3 iso1 <sub>540-665</sub>	Co-expression of untagged full-length RUVBL2, and His-tagged RPAP3 iso1 residues 540-665	This study
pQLink RUVBL1 <sub>Δ126-234</sub> , RUVBL2 <sub>Δ133-238</sub> , H7-RPAP3 iso1 <sub>1-665</sub>	Co-expression of untagged RUVBL1 and RUVBL2, both lacking the external DII, and His-tagged full-length RPAP3 iso1	This study
pQLink RUVBL1 <sub>1-456</sub> , H7-RPAP3 iso1 <sub>385-665</sub>	Co-expression of untagged full-length RUVBL1 and His-tagged RPAP3 iso1 residues 385-665	This study
pQLink RUVBL2 <sub>1-463</sub> , H7-RPAP3 iso1 <sub>385-665</sub>	Co-expression of untagged full-length RUVBL2 and His-tagged RPAP3 iso1 residues 385-665	This study
pQLink RUVBL1 <sub>1-456</sub> , H7-RPAP3 iso1 <sub>442-665</sub>	Co-expression of untagged full-length RUVBL1 and His-tagged RPAP3 iso1 residues 442-665	This study
pQLink RUVBL2 <sub>1-463</sub> , H7-RPAP3 iso1 <sub>442-665</sub>	Co-expression of untagged full-length RUVBL2 and His-tagged RPAP3 iso1 residues 442-665	This study
pQLink RUVBL1 <sub>1-456</sub> , H7-RPAP3 iso1 <sub>385-665/Δ492-500</sub>	Co-expression of untagged full-length RUVBL1 and His-tagged RPAP3 iso1 residues 385-665, with the deletion of residues 492-500	This study

pQLink RUVBL2 <sub>1-463</sub> , H7-RPAP3 iso1 <sub>385-665/Δ492-500</sub>	Co-expression of untagged full-length RUVBL2 and His-tagged RPAP3 iso1 residues 385-665, with the deletion of residues 492-500	This study
pQLink RUVBL1 <sub>1-456</sub> , H7-RPAP3 iso1 <sub>442-665/Δ492-500</sub>	Co-expression of untagged full-length RUVBL1 and His-tagged RPAP3 iso1 442-665, with the deletion of residues 492-500	This study
pQLink RUVBL2 <sub>1-463</sub> , H7-TEV-RPAP3 iso1 <sub>442-665/ Δ492-500</sub>	Co-expression of untagged full-length RUVBL2 and His-tagged RPAP3 iso1 442-665, with the deletion of residues 492-500	This study
pQLink H7-RPAP3 iso1 <sub>1-665</sub> , PIH1D1 <sub>1-290</sub>	Co-expression of His-tagged full-length RPAP3 iso1 and untagged full-length PIH1D1	This study
pQLink H7-RPAP3 iso2 <sub>1-631</sub> , PIH1D1 <sub>1-290</sub>	Co-expression of His-tagged full-length RPAP3 iso2 and untagged full-length PIH1D1	This study
pQLink H7-RPAP3 iso1 <sub>385-665</sub> , PIH1D1 <sub>1-290</sub>	Co-expression of His-tagged RPAP3 iso1 residues 385-665 and untagged full-length PIH1D1	This study
pQLink H7-RPAP3 iso2 <sub>385-631</sub> , PIH1D1 <sub>1-290</sub>	Co-expression of His-tagged RPAP3 iso2 residues 385-631 and untagged full-length PIH1D1	This study
pQLink H7-RPAP3 iso1 <sub>1-665</sub> , PIH1D1 <sub>1-280</sub>	Co-expression of His-tagged full-length RPAP3 isoform 1 and untagged PIH1D1 residues 1-280	This study
pQLink H7-RPAP3 iso1 <sub>540-665</sub> , PIH1D1 <sub>1-290</sub>	Co-expression of His-tagged RPAP3 iso1 residues 540-665, and untagged full-length PIH1D1	This study
pQLink H7-RPAP3 iso1 <sub>1-540</sub> , PIH1D1 <sub>1-290</sub>	Co-expression of His-tagged RPAP3 iso1 residues 1-540, and untagged full-length PIH1D1	This study
p11 H6-RUVBL1 <sub>1-456</sub> WB	His-tagged full-length RUVBL1 D302N expression	This study
p11 H6-RUVBL2 <sub>1-463</sub> WB	His-tagged full-length RUVBL2 D299N expression	This study
pCOLADuet-1 RUVBL1 <sub>1-456</sub> -H6, eXact tag-RUVBL2 <sub>1-463</sub>	Co-expression of His-tagged full-length RUVBL1 and eXact-tagged full-length RUVBL2	This study
p11 H6-RUVBL1 <sub>1-456</sub> ND	His-tagged full-length RUVBL1 D353N expression	This study
p11 H6-RUVBL1 <sub>1-456</sub> DN	His-tagged full-length RUVBL1 D356N expression	This study
p11 H6-RUVBL1 <sub>1-456</sub> NN	His-tagged full-length RUVBL1 D353N/D356N expression	This study
p11 H6-RUVBL2 <sub>1-463</sub> ND	His-tagged full-length RUVBL2 D349N expression	Nano <i>et al.</i> , 2020
p11 H6-RUVBL2 <sub>1-463</sub> DN	His-tagged full-length RUVBL2 D352N expression	Nano <i>et al.</i> , 2020
p11 H6-RUVBL2 <sub>1-463</sub> NN	His-tagged full-length RUVBL2 D349N/D352N expression	Nano <i>et al.</i> , 2020
pETSUMO2 H12-SUMO-RPAP3 iso1 <sub>540-665</sub>	His and SUMO-tagged full-length RPAP3 iso1 C-terminal domain expression	This study

pQLink RUVBL1 <sub>1-456</sub> , H7-RPAP3 iso2 <sub>1-631</sub>	Co-expression of untagged full-length RUVBL1 and His-tagged full-length RPAP3 iso2	This study
pQLink RUVBL2 <sub>1-463</sub> , H7-RPAP3 iso1 <sub>1-631</sub>	Co-expression of untagged full-length RUVBL2 and His-tagged full-length RPAP3 iso2	This study
pQLink RUVBL1 <sub>1-456</sub> , H7-RPAP3 iso2 <sub>385-631</sub>	Co-expression of untagged full-length RUVBL1 and His-tagged RPAP3 iso2 residues 385-631	This study
pQLink RUVBL2 <sub>1-463</sub> , H7-RPAP3 iso2 <sub>385-631</sub>	Co-expression of untagged full-length RUVBL2 and His-tagged RPAP3 iso2 residues 385-631	This study
pCOLADuet-1 RPAP3 iso2 <sub>1-631</sub> , H6-PIH1D1 <sub>1-290</sub>	Co-expression of untagged full-length RPAP3 iso2 and His-tagged full-length PIH1D1	This study
pQLink RPAP3 iso1 <sub>385-665</sub> -FLAG, H7-PIH1D1 <sub>1-290</sub>	Co-expression of FLAG-tagged RPAP3 iso1 residues 385-665 and His-tagged full-length PIH1D1	This study
pQLink RPAP3 iso2 <sub>385-631</sub> -FLAG, H7-PIH1D1 <sub>1-290</sub>	Co-expression of FLAG-tagged RPAP3 iso2 residues 385-631 and His-tagged full-length PIH1D1	This study
pQLink RPAP3 iso1 <sub>540-665</sub> -FLAG, H7-PIH1D1 <sub>1-290</sub>	Co-expression of FLAG-tagged RPAP3 iso1 residues 540-665, and His-tagged full-length PIH1D1	This study
pQLink RPAP3 iso1 <sub>1-540</sub> , H7-PIH1D1 <sub>1-290</sub>	Co-expression of untagged RPAP3 iso1 residues 1-540, and His-tagged full-length PIH1D1	This study
pOBD2 RPAP3 <sub>1-665</sub>	Expression of full-length RPAP3 iso1 fused to the GAL4 DNA-binding domain for yeast 2-hybrid assays <sup>c</sup>	This study
pOBD2 RPAP3 <sub>1-565</sub>	Expression of RPAP3 iso1 residues 1-565 fused to the GAL4 DNA-binding domain for yeast 2-hybrid assays <sup>c</sup>	This study
pOBD2 RPAP3 <sub>1-465</sub>	Expression of RPAP3 iso1 residues 1-465 fused to the GAL4 DNA-binding domain for yeast 2-hybrid assays <sup>c</sup>	This study
pOBD2 RPAP3 <sub>1-415</sub>	Expression of RPAP3 iso1 residues 1-415 fused to the GAL4 DNA-binding domain for yeast 2-hybrid assays <sup>c</sup>	This study
pOBD2 RPAP3 <sub>1-390</sub>	Expression of RPAP3 iso1 residues 1-390 fused to the GAL4 activation domain for yeast 2-hybrid assays <sup>c</sup>	This study
pOAD PIH1D1 <sub>1-290</sub>	Expression of full-length PIH1D1 fused to the GAL4 activation domain for yeast 2-hybrid assays <sup>c</sup>	This study
pOAD PIH1D1 <sub>1-280</sub>	Expression of PIH1D1 residues 1-280 fused to the GAL4 activation domain for yeast 2-hybrid assays <sup>c</sup>	This study
pcDNA5 FLAG-PIH1D1	Expression of full-length N-terminally FLAG-tagged PIH1D1 <sup>d</sup>	This study
pcDNA5 RPAP3 iso1-3xFLAG	Expression of full-length C-terminally 3xFLAG-tagged RPAP3 iso1 <sup>d</sup>	This study

pcDNA5 RPAP3 iso1-3xFLAG	Expression of full-length C-terminally 3xFLAG-tagged RPAP3 iso2 <sup>d</sup>	This study
pcDNA5 FLAG-RPAP3 iso1	Expression of full-length N-terminally FLAG-tagged RPAP3 iso1 <sup>d</sup>	This study

<sup>a</sup>All constructs were expressed in *E.coli* LOBSTR pRIL strain, unless stated otherwise.

<sup>b</sup>His-tagged proteins expressed from pQLink, p11 and pCOLADuet-1 contained a TEV cut site between the tag and the protein; proteins expressed from pETSUMO2 had their His-SUMO tag removed by Ulp1 digestion.

<sup>c</sup>Constructs were expressed in *S. cerevisiae* PJ69-4a strain.

<sup>d</sup>Constructs were expressed transiently in RPE-1 cells.

**Table S6. Buffer solutions used in this work, Related to STAR Methods.**

Buffer	Composition
A	25 mM Tris-HCl (pH 7.5), 500 mM NaCl
B	25 mM Tris-HCl (pH 7.5), 500 mM NaCl, 500 mM imidazole
C	25 mM Tris-HCl (pH 7.5), 50 mM KCl, 10% glycerol, 1 mM DTT
D	25 mM Tris-HCl (pH 7.5), 500 mM KCl, 10% glycerol, 1 mM DTT
E	40 mM Tris-HCl (pH 7.5), 200 mM KCl, 5 mM MgCl <sub>2</sub> , 1 mM DTT, 10% Glycerol
F	25 mM Tris-HCl (pH 7.5), 200 mM NaCl, 10% glycerol
G	25 mM Tris-HCl (pH 7.5), 50 mM NaCl
H	25 mM Tris-HCl (pH 7.5), 500 mM NaCl
I	25 mM Tris-HCl (pH 7.5), 200 mM NaCl
J	25 mM Tris-HCl (pH 7.5), 200 mM NaCl, 250 mM imidazole
K	20 mM Tris-HCl, pH 7.5, 200 mM KCl, 8 mM MgCl <sub>2</sub> , 10% (v/v) glycerol
L	25 mM Tris-HCl (pH 7.5), 200 mM NaCl, 1 mM DTT, 10% glycerol
M	25 mM HEPES (pH 7.5), 200 mM NaCl, 5% glycerol
N	50 mM Tris-HCl (pH 7.4), 150 mM NaCl, 1 mM EDTA, 1% Triton X-100
O	50 mM Tris-HCl (pH 7.4), 150 mM NaCl, 0.05% Nonidet P-40
P	50 mM Tris-HCl (pH 7.4), 150 mM NaCl
Q	40 mM Tris-HCl (pH 7.5), 200 mM KCl, 5 mM MgCl <sub>2</sub>